Solid-state photonic interfaces using semiconductor quantum dots

Antoine Boyer de la Giroday

Darwin College

University of Cambridge
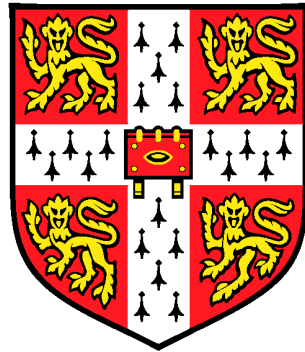
A dissertation submitted for the degree of

Doctor of Philosophy

August 2011

Acknowledgements

This work would not have been possible without the help and expertise of a number of people.

I thank my supervisors Dr. Andrew Shields and Prof. David Ritchie for giving me this unique opportunity to work on an exciting project in the best possible conditions at Toshiba Research Europe Ltd. and the Cavendish Laboratory. Moreover, their supervision and guidance have been invaluable. I have truly enjoyed my time in Cambridge and you two made it all possible, thanks a lot. Thanks must also go to EPSRC and Toshiba Research Europe Ltd. for financial support.

Luckily, I have worked alongside Dr. Niklas Sköld for most of my Ph.D. and his help was crucial. Niklas, thank you so much for your deep understanding of physics, great experimental skills, availability, and more importantly your constant good mood and kindness. It was a pleasure working with you.

I thank all the lovely people from Toshiba and the Cavendish for their help and for creating such a nice work environment. More particularly, Dr. Anthony Bennett, Dr. Mark Stevenson, and Dr. Robert Young were of great assistance at various stages and taught me a lot through fruitful discussions. I must also acknowledge my fellow students Cameron Salter, Matt Pooley, Andre Schwagmann, Phil Intallura, Raj Patel, Sam Dewhurst, Alex Dixon, Michael Conterio, Matt Dean and many others. Cheers for everything guys.

Dr. Ian Farrer grew all the wafers used in this thesis and Ken Cooper taught me how to process proper devices (among many other things). Thanks guys for your cooperation and hard work.

Lastly, I extend my gratitude to my family and friends who have encouraged me in everything that I have endeavoured. Above all, thanks to my dear Armande for her constant love and support.

Journal publications

1. *Quantum memories*
   C. Simon, M. Afzelius, J. Appel, **A. Boyer de la Giroday**, S.J. Dewhurst, N. Gisin, C.Y. Hu, F. Jelezko, S. Kröll, J.H. Müller, J. Nunn, E.S. Polzik, J.G. Rarity, H. De Riedmatten, W. Rosenfeld, A.J. Shields, N. Sköld, R.M. Stevenson, R. Thew, I.A. Walmsley, M.C. Weber, H. Weinfurter, J. Wrachtrup, and R.J. Young
   Eur. Phys. J. D 58, 1-22 (2010)

2. *Electric-field-induced coherent coupling of the exciton states in a single quantum dot*
   A.J. Bennett, M.A. Pooley, R.M. Stevenson, M.B. Ward, R.B. Patel, **A. Boyer de la Giroday**, N. Sköld, I. Farrer, C.A. Nicoll, D.A. Ritchie, and A.J. Shields
   Nature Physics, 6, 947 (2010)

3. *All-electrical coherent control of the exciton states in a single quantum dot*
   A. Boyer de la Giroday, A.J. Bennett, M.A. Pooley, R.M. Stevenson, N. Sköld, R.B. Patel, I. Farrer, D.A. Ritchie, and A.J. Shields
   Phys. Rev. B 82, 241301 (2010)

4. *Exciton-spin memory with a semiconductor quantum dot molecule*
   A. Boyer de la Giroday, N. Sköld, R.M. Stevenson, I. Farrer, D.A. Ritchie, and A.J. Shields
   Phys. Rev. Lett. 106, 216802 (2011)

5. *Coherent entangled light generated by quantum dots in the presence of nuclear magnetic fields*
   R.M. Stevenson, C.L. Salter, **A. Boyer de la Giroday**, I. Farrer, C.A. Nicoll, D.A. Ritchie, and A.J. Shields
   arXiv:1103.2969v1

6. *Excitonic couplings and Stark effect in individual quantum dot molecules*
   A. Boyer de la Giroday, N. Sköld, R.M. Stevenson, I. Farrer, D.A.
   Ritchie, and A.J. Shields
   J. Appl. Phys. 110, 083511 (2011)

7. *Electrical control of the exciton fine structure of a quantum dot molecule*
   N. Sköld, **A. Boyer de la Giroday**, A.J. Bennett, I. Farrer, D.A.
   Ritchie, and A.J. Shields
   In preparation

Conference proceedings

1. *Semiconductor single photon devices for quantum information processing*
   O. Thomas, C.L. Salter, A.J. Bennett, R.M. Stevenson, M.A. Pooley, M.B. Ward, R.B. Patel, **A. Boyer de la Giroday**, N. Sköld, I. Farrer, C.A. Nicoll, D.A. Ritchie, and A.J. Shields
   Proc. QCMC 2010

2. *Observation of anticrossings in the exciton state of single quantum dots via electrical tuning of the fine-structure splitting*
   M.A. Pooley, A.J. Bennett, R.M. Stevenson, M.B. Ward, R.B. Patel, **A. Boyer de la Giroday**, N. Sköld, I. Farrer, C.A. Nicoll, D.A. Ritchie, and A.J. Shields
   J. Phys.: Conf. Ser. 286, 012026 (2011)

3. *Coherent coupling of the excitonic states in a single quantum dot*
   A.J. Bennett, M.A. Pooley, R.M. Stevenson, M.B. Ward, R.B. Patel, **A. Boyer de la Giroday**, N. Sköld, I. Farrer, C.A. Nicoll, D.A. Ritchie, and A.J. Shields
   Proc. SPIE 7947, 794707 (2011)

4. *High-speed electrical control of a solid-state photonic quantum interface*
   A. Boyer de la Giroday, A.J. Bennett, M.A. Pooley, R.M. Stevenson, N. Sköld, R.B. Patel, I. Farrer, D.A. Ritchie, and A.J. Shields
   Quantum Electronics and Laser Science Conference, OSA Technical Digest (CD) (Optical Society of America, 2011), paper QThR6

5. *Exciton-spin memory with a single semiconductor quantum dot molecule*
   N. Sköld, **A. Boyer de la Giroday**, R.M. Stevenson, I. Farrer, D.A. Ritchie, and A.J. Shields
   CLEO/Europe and EQEC 2011 Conference Digest, OSA Technical Digest (CD) (Optical Society of America, 2011), paper ED1_2

Contributed talks

1. *High-fidelity electrical coherent control of the exciton states in a single quantum dot*
   A. Boyer de la Giroday, A.J. Bennett, M.A. Pooley, R.M. Stevenson, N. Sköld, R.B. Patel, I. Farrer, D.A. Ritchie, and A.J. Shields
   Quantum Dot Day 2011, Bristol (UK), 10 January 2011

2. *High-speed electrical control of a solid-state photonic quantum interface*
   A. Boyer de la Giroday, A.J. Bennett, M.A. Pooley, R.M. Stevenson, N. Sköld, R.B. Patel, I. Farrer, D.A. Ritchie, and A.J. Shields
   CLEO 2011, Baltimore (USA), 1-6 May 2011

3. *Quantum information processing with semiconductor nanotechnology*
   A. Boyer de la Giroday
   Darwin Science Seminar, Cambridge (UK), 9 June 2011

4. *Solid-state photonic interfaces using semiconductor quantum dots*
   A. Boyer de la Giroday, A.J. Bennett, N. Sköld, M.A. Pooley, R.M. Stevenson, M.B. Ward, R.B. Patel, I. Farrer, C.A. Nicoll, D.A. Ritchie, and A.J. Shields
   Consortium on quantum repeaters, Bad Honnef (Germany), 20-22 June 2011

5. *Spin storage and manipulation in semiconductor quantum dots*
   A. Boyer de la Giroday, N. Sköld, A.J. Bennett, R.M. Stevenson, M.A. Pooley, M.B. Ward, R.B. Patel, I. Farrer, C.A. Nicoll, D.A. Ritchie, and A.J. Shields
   The Rank Prize Fund symposium on optical implementations of quantum information, Cumbria (UK), 3-6 October 2011

Summary

New technologies based on the properties of quantum mechanics promise to revolutionise the way information is processed by outperforming what is possible using classical devices. Examples include massively parallel processing using quantum computers, verifiably secure communication using quantum cryptography, and measurement with sensitivity beyond classical limitation with quantum metrology. Realising the full potential of these technologies necessitates the ability to communicate quantum information over large distances, a key requirement for future quantum networks. However, developing practical implementations of long-distance quantum communication is challenging as it necessitates three major ingredients: light-matter interfaces, elementary quantum operations, and quantum memories. This thesis describes work that has been undertaken to address these requirements using semiconductor nanotechnology.

We have first demonstrated that single InAs quantum dots embedded inside conventional diode structures constitute high-fidelity controllable interfaces between optical qubits and solid-state qubits. Indeed, the polarisation state of a photon was transferred into the spin state of an electron-hole pair and eventually restored through radiative recombination of the electron and the hole with a fidelity up to 95%. Moreover, spins were manipulated using subnanosecond modulation of a vertical electric field applied to the quantum dots. By controlling this electrical modulation, we demonstrated elementary phase-shift and spin-flip gate operations with near-unity fidelities.

An electron-hole pair confined in a single quantum dot has a short radiative lifetime limiting therefore its use as an excitonic quantum memory. The solution we proposed was to use a quantum dot molecule to control the spatial separation of the electron and the hole and therefore prevent their recombination. Comprehensive studies of electric field effects upon the photoluminescence of quantum dot molecules lead to a clear understanding and a good control over their physical properties. Single photons were stored in individual quantum dot molecules up to 1μs and read out on a subnanosec-

ond time scale. Moreover, the circular polarisation of individual photons was transferred into the spin state of electron-hole pairs with a fidelity above 90%, which does not degrade for storage times up to the 12.5 ns repetition period of the experiment.

Our work on single quantum dots could be extended in the near future to allow for two-qubits quantum operations by confining a second electron-hole pair to be electrically manipulated. Storage of a superposition of spin states in a quantum dot molecule should also be possible if the spin states are made degenerate, which is feasible using the electric field dependence of the energy splitting between the spin states discussed in this thesis. We believe that combining both approaches will lead to the development of a controllable multi-qubit quantum memory for polarised light, a building block for long-distance quantum communication based on semiconductor nanotechnology.

Contents

Chapter 1

Introduction

Since the seminal theoretical work of Claude Shannnon in 1948 [1], the concept of "information" has acquired a central place in modern society. Indeed, most of human activities now heavily rely on various practical implementations of "information devices" such as computers and mobile phones. Moreover, communication based on the fast and reliable transfer and processing of information, whether it is through electrical, optical or other means, has been constantly increasing. This is particularly true considering the emergence of the internet in the last twenty years. In 2010, around 9 trillion emails were exchanged between 1.9 billion email users in the world.

The key point behind any information device is that the representation of information must be of physical nature [2]. As a consequence, the way information can be processed by a specific device is strongly related to its physical properties. A device based on quantum carriers of information is therefore expected to exhibit radically different properties compared to a device governed by classical physics. This observation has naturally lead to the development of the field of "quantum information science", which focuses on taking advantage of the fundamental properties of quantum mechanics in order to process information far beyond what is permitted by classical physics. Striking theoretical results have been discovered, such as quantum key distribution for unconditionally secured cryptography, quantum teleportation, quantum algorithms, and quantum computing [3, 4, 5]. These results have

led to great interest in practical realisations of those new ways of processing information. Even though some realisations have already been developed, the field is still in its infancy and further progress needs to be made. Efficient implementations of innovative "quantum information devices" are expected to revolutionise the entire IT industry over the next two decades.

Typical examples of promising quantum information technologies include nuclear magnetic resonance [6], ion traps [7, 8], cavity QED with neutral atoms and molecules [9, 10, 11], Bose-Einstein condensates [12], and superconducting qubits [13, 14]. In this thesis, we focus on another promising approach based on solid-state devices, more specifically on semiconductor self-assembled quantum dots.

1.1 Quantum information using semiconductor quantum dots

Semiconductor quantum dots (QDs) are nanometre scale regions made of a semiconductor material and surrounded by another semiconductor material presenting a higher band-gap in order to create a potential well. As a consequence, QDs confine electrons and holes in all three spatial dimensions on discrete energy levels, leading to a demonstrated shell structure. They are therefore usually described as "artificial atoms" and have the necessary quantum properties to be used as a resource for quantum information processing. They present however some differences from single atoms. They are indeed orders of magnitudes bigger, they allow for easier spatial control, and also for tunability (notably in their absorption/emission spectrum) over a large range of values by varying the QD dimensions, geometry or composition. Moreover, semiconductor quantum devices have a high potential for scalability as opposed to many other quantum technologies. Scalability opens up the possibility of fabricating large integrated networks required for quantum computation and communication. QDs are fully integrable in well-established, low-cost, conventional semiconductor electrical diode structures and benefit therefore from the progresses made during the past decades in

the semiconductor industry.

QDs naturally appear as good candidates for pratical implementations of quantum information processing devices, which has triggered much research activity in the field the past few years leading to remarkable progress. They have been demonstrated as efficient optically and electrically driven single photon sources [15, 16, 17], a key component to many quantum information applications including quantum cryptogaphy [18] and quantum computation [19, 20]. Moreover, they have been used to optically and electrically generate on-demand entangled photon pairs [21, 22, 23], a necessary resource for quantum teleportation [24]. Other important results include quantum key distribution at telecom wavelength [25], two-photon interference [26, 27, 28] and coherent manipulation of electron and electron-hole pair spins [29, 30, 31, 32].

Despite these recent results, much progress is still needed to fully exploit the potential of semiconductor quantum technologies. In this thesis, we will more specifically focus on some key missing elements required for the development of scalable quantum networks, which will allow spatially-separated parties to manipulate and communicate quantum information.

1.2 Solid-state photonic interfaces for quantum networks

A quantum network consists of quantum nodes connected by a quantum channel. Quantum nodes generate, process and store quantum information while the quantum channel is needed to communicate and distribute quantum information and entanglement between the nodes. Photonic "flying" qubits are usually used for quantum communication [33, 34, 35] as they weakly interact with the environment, particularly when they propagate through optical fibres used as the quantum channel. On the other hand, solid-state "stationary" qubits may be better suited to perform quantum computations [30, 36, 37, 38]. An interface between light and matter is therefore a key element to a quantum network.

Moreover, scalability requires long-distance quantum communication be-

tween the nodes. However, this is ultimately limited for photonic qubits by losses (i.e. scattering and absorption) in optical fibres, which both grow exponentially with fibre length. This problem is solved in the case of classical communication through repeated amplification of the light pulses carrying the information. This is however forbidden in the case of quantum communication by the no-cloning theorem [39] of quantum physics. A quantum repeater protocol [40] is therefore needed to achieve remote qubit entanglement. Such a protocol relies on entanglement swapping [41]. Consider two pairs of entangled states, (A, B) and (C, D). It is possible to entangle A and D by performing a joint measurement of systems B and C in a basis of entangled states, followed by classical communication of the results to the location of system A and/or D [42]. Using this property, entanglement is distributed between two independent quantum nodes separated by a long distance L by dividing L in shorter elementary links of length comparable to the fibre absorption length. Entanglement is then created independently within short elementary links and then successively swapped between neighbouring links until distributed over the distance L separating the nodes.

The two key elements to a deterministic quantum repeater protocol are a quantum memory and elementary quantum gates. Indeed, the created entanglement between elementary links must be stored until entanglement is established between neighbouring links in order to perform the necessary operations required to achieve entanglement swapping. These operations consist in performing local joint measurements projecting onto entangled states between two memories, which would be possible with elementary quantum gates between neighbouring memories, as single-qubit operations combined with a controlled-NOT gate constitute a universal quantum logic gate [43, 44, 45].

1.3 Thesis outline

This thesis describes the progresses achieved towards the realisation of controllable solid-state photonic quantum interfaces using semiconductor quantum dots, which may, in the future, constitute the building blocks of solid-state quantum repeaters for scalable quantum network architectures.

We start in chapters 2 and 3 by introducing the most important properties of semiconductor quantum dots as well as the experimental methods needed to understand the main results presented in the thesis.

In chapter 4, we use single quantum dots to demonstrate high-fidelity reversible transfer of quantum information from the polarisation of photons into the spin state of an electron-hole pair. We then electrically manipulate spins on a subnanosecond time scale, which allows to coherently control their time evolution. By varying the area of the electrical pulse, we demonstrate phase-shift and spin-flip gate operations with near-unity fidelities. Though these results represent an important step towards a controllable semiconductor quantum interface, the short radiative lifetime of single dots limit storage of quantum information to the nanosecond scale, insufficient for a quantum memory or a quantum repeater. The approach we have followed to overcome this issue is to use a pair of coupled quantum dots, known as a quantum dot molecule, to control the electron-hole pair spatial separation leading to longer lifetimes.

Chapter 5 presents a comprehensive study of electric field effects upon the photoluminescence of individual quantum dot molecules. This study provides a deep understanding of the physics behind quantum dot molecules, notably through the analysis of the spectroscopic patterns arising from the different charged states of a quantum dot molecule. A simple model accurately describing this extremely rich line structure is also presented. Moreover, reversing the doping sequence of the diode structure allows both electron and hole coupling between the dots to be investigated. High potential barriers cladding the quantum dot molecule allow the application of strong electric fields, resulting in a larger than expected quantum confined Stark effect. Finally, the fine structure of an electron-pair pair confined in a quantum dot molecules is studied as a function of electric field and an unexpected rotation of the eigenstates is demonstrated, which is a key requirement to allow for electrically controlled quantum operations on the electron-hole pair spin state.

In chapter 6, we report on a single photon and spin storage device based on a semiconductor quantum dot molecule. Optically excited single electron-

hole pairs are trapped within the molecule, and their recombination rate is electrically controlled over 3 orders of magnitude. Single photons are stored up to 1 μs and read out on a subnanosecond time scale. By using resonant excitation, the circular polarisation of individual photons is transferred into the spin state of electron-hole pairs with a fidelity above 80%, which does not degrade for storage times up to the 12.5 ns repetition period of the experiment. Eventually, we provide some leads to extend the spin-memory scheme to a quantum memory for polarised light.

Finally, we draw our conclusions in chapter 7 on the results presented in this thesis as well as present some potential future lines of research.

Chapter 2

Semiconductor quantum dots

This chapter provides the background knowledge on semiconductor quantum dots (QDs) required to understand the following chapters of this thesis. A theoretical approximation explaining the effect of confinement and the origin of the "atom-like" properties of QDs is presented. The physical and optical properties of QDs relevant to this thesis are explained and quantum dot molecules (QDMs) are introduced. More extensive reviews on QDs can be found in [46, 47].

2.1   Theoretical background

In this section, we discuss the effect of reducing the dimensions of quantum nanostructures on the energy, wavefunction, and density of states of carriers in semiconductors [48]. We use the effective-mass approximation, which assumes that the envelope wavefunction does not vary much in the unit cell with a length scale of subnanometres. This is verified for the simplified picture of the nanostructures discussed here.

Within the effective-mass approximation, the electron is described as a "free" electron with an effective mass usually labelled m^*. Assuming a parabolic band dispersion, the band-edge electron states of semiconductors are described by the effective-mass equation

$$\left[-\frac{\hbar^2}{2m^*}\nabla^2 + V(\mathbf{r}) \right] F_k(\mathbf{r}) = \epsilon F_k(\mathbf{r}), \tag{2.1}$$

where $\hbar$ is the reduced Planck's constant, $\mathbf{r} = (x, y, z)$ is the electron position vector, $V(\mathbf{r})$ is the confinement potential, F_k is the envelope wave function, and ϵ is the electron energy. The electron wavefunction Ψ is then given by

$$\Psi = F_k(\mathbf{r})u_0(\mathbf{r}), \tag{2.2}$$

where the envelope function F_k is obtained by resolving Eq. (2.1), and where the Bloch function $u_0(\mathbf{r})$ and m^* are usually calculated using the **k.p** perturbation theory [49].

2.1.1 Bulk material

In a bulk semiconductor, $V(\mathbf{r})$ can be approximated to 0 and solving Eq. (2.1) leads to the energy

$$\epsilon = E(\mathbf{k}) = \frac{\hbar^2 k^2}{2m^*}, \tag{2.3}$$

and the normalised envelope wave function

$$F_k(\mathbf{r}) = \frac{1}{\sqrt{V}}e^{-i\mathbf{k}.\mathbf{r}}, \tag{2.4}$$

where V is the volume of the bulk material considered and $\mathbf{k}$ is the wave vector. $\mathbf{k}$ must satisfy the periodic boundary conditions leading to $\mathbf{k} = \left(\frac{n_x 2\pi}{L_x}, \frac{n_y 2\pi}{L_y}, \frac{n_z 2\pi}{L_z} \right)$, where n_x, n_y, n_z are integers. The density of states $g(E)$ per unit volume, i.e. the number of states between an energy of E and an energy of $E + dE$, is given by

$$g(E) = \frac{2}{V}\sum_{\mathbf{k}} \delta\left[E(\mathbf{k}) - E\right] = \frac{1}{2\pi^2}\left(\frac{2m^*}{\hbar^2}\right)^{\frac{3}{2}} E^{\frac{1}{2}}. \tag{2.5}$$

2.1.2 Effect of confinement

Confinement of a carrier in a particular direction arises when the energy potential in this direction is such that the motion of the carrier is confined on a scale comparable to the de Broglie wavelength λ_b given by

$$\lambda_b = \frac{h}{p} \propto \frac{h}{\sqrt{m^* k_B T}}, \tag{2.6}$$

where p is the electron momentum, h and k_B are Planck's and Boltzmann's constant, m^* is the carrier effective mass, and T is the temperature. By properly choosing the semiconductor material as well as by working at low temperature, quantization can appear on scales that are large compared to the lattice constant of the crystal. At cryogenic temperature, λ_b is on the order of $10 - 100 nm$ for InAs and GaAs, which is the typical size of a self-assembled semiconductor QD.

Confinement along a particular dimension results in quantized energy levels along that dimension. This is illustrated in Fig. 2.1, where the parabolic density of states $g(E)$ for a bulk material obtained in Eq. (2.5) is compared to those of the three main types of semiconductor nanostructures: quantum wells (2D confinement), quantum wires (1D confinement) and quantum dots (0D confinement).

2.1.3 Quantum dots

To understand the discrete density of states of QDs, we assume here that QDs consist in rectangular boxes of dimensions L_x, L_y, and L_z and that the confinement potential $V(\mathbf{r})$ is infinitely high for all directions and therefore given by

$$V(\mathbf{r}) = V(x) + V(y) + V(z), \tag{2.7}$$

where $V(i) = \infty$ when $|i| \geq L_i/2$ and $V(i) = 0$ when $|i| \leq L_i/2$, for i=x,y,z. Solving Eq. (2.1) with this potential leads to
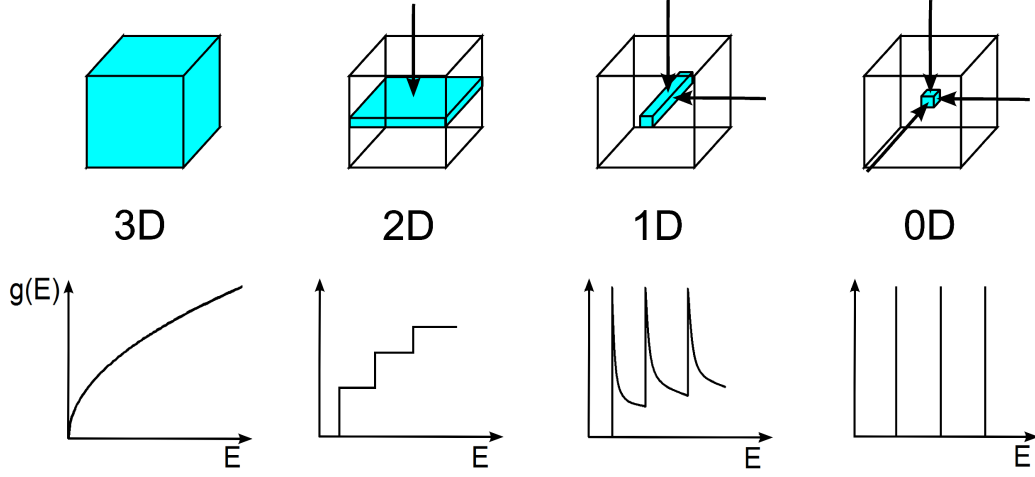
Figure 2.1: Schematic representation of the effect of reducing the dimensions of a semiconductor material on the density of states. Discrete energy levels appear when the material is reduced in all 3 spatial dimensions, leading to so-called quantum dots.

$$\epsilon = E(\mathbf{k}) = E_{n_x} + E_{n_y} + E_{n_z} = \frac{\hbar^2}{2m^*}\left[\left(\frac{n_x\pi}{L_x}\right)^2 + \left(\frac{n_y\pi}{L_y}\right)^2 + \left(\frac{n_z\pi}{L_z}\right)^2\right], \quad (2.8)$$

where n_x, n_y, n_z are integers and $\mathbf{k} = \left(\frac{n_x\pi}{L_x}, \frac{n_y\pi}{L_y}, \frac{n_z\pi}{L_z}\right)$. This demonstrated shell structure arising from carrier confinement in all three spatial dimensions is similar to the discrete energy levels of an atom and QDs are therefore often referred to as "artificial atoms". The corresponding wave function is given by

$$F(\mathbf{r}) = \phi_{n_x}(x)\phi_{n_y}(y)\phi_{n_z}(z), \quad (2.9)$$

where $\phi_{n_i}(i) = \sqrt{\frac{2}{L_i}}\sin\left[n_i\pi(\frac{i}{L_i} + \frac{1}{2})\right]$. Finally, the density of states for QDs is given by

$$g(E) = 2N_D \sum_{n_x,n_y,n_z} \delta(E - E_{n_x} - E_{n_y} - E_{n_z}), \quad (2.10)$$

where N_D is the volume density of QDs (Fig. 2.1).

2.2 Schematic band diagram

Two types of QDs can be distinguished. QDs which simultaneously trap electrons and holes are called type-1 QDs while type-2 QDs attract only one type of carriers and repel the other [50]. Our research focuses on type-1 QDs. To achieve confinement in a type-1 QD, the material used to make the QD is chosen to have a bandgap smaller than that of the bulk material it is embedded in. In this thesis, we will be concerned with InAs (bandgap of $0.354eV$ at $300K$) QDs grown on GaAs (bandgap of $1.424eV$ at $300K$), the most common type of QDs. The direct bandgap of InAs allows for efficient optical transitions within the QD. A schematic band diagram of the type of QDs used in this thesis is shown in Fig. 2.2.

2.3 Excitation schemes

Carriers in a QD are usually created either through electrical injection [16] or photo-excitation. Other ways include thermal excitation and more complex schemes such as band-driven surface-acoustic-wave injection [51]. In this thesis, we concentrate on photo-exciting electrons from the valence band into the conduction band, leaving a hole in the valence band. We distinguish three different excitation schemes (illustrated in Fig. 2.2) leading to significantly different carrier dynamics and properties of the emission as will be demonstrated in the following chapters.

2.3.1 Above-band excitation

Carriers are photo-excited in the bulk GaAs material surrounding the QD with a light source of energy higher that the bandgap of GaAs. The carriers are then captured in a random manner by the wetting layer, which is essentially a thin quantum well made of a material with a bandgap lower than the bandgap of GaAs. Carriers eventually relax down to the lowest energy levels of the QD through non-radiative processes occurring on a time scale of around 10-100ps and dominated by longitudinal-optical phonon scattering
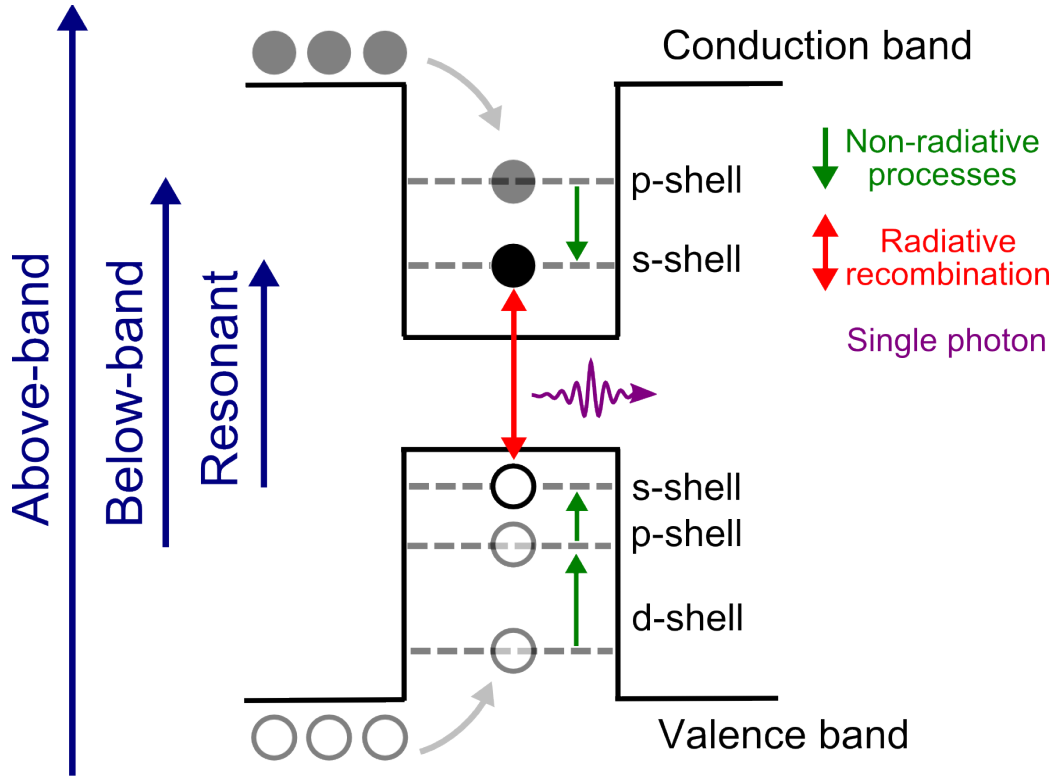
Figure 2.2: Schematic band structure of an InAs QD grown on GaAs showing an "atom-like" shell structure. Carriers excited in the bulk GaAs material will relax into the QD and decay to the s-shell through non-radiative processes. Carriers can also be directly excited quasi-resonantly or resonantly into the QD. An electron-hole pair in the s-shell can recombine and emit a single photon. There is a finite time delay before another electron-hole pair can repopulate the s-shell, leading to single photon emission.

[52, 53]. An electron-hole pair can then recombine and emit a single photon with a total energy equal to the bandgap energy plus the confinement energy of the electron and the hole. This energy is significantly different from the excitation energy and the light source can easily be filtered away, which is essential in the case of a confocal setup.

2.3.2 Quasi-resonant excitation

Carriers are photo-excited with a light source of energy lower than the GaAs bandgap energy but higher than the s-shell energy. Carriers are therefore

created directly into an excited electronic state of the QD before relaxing down to the s-shell on a picosecond timescale. Most common types of quasi-resonant excitation schemes include optical pumping of the p-shell transition or pumping of the s-shell through the creation of a 1-LO phonon in GaAs. This scheme requires significantly more power than above-band excitation considering the smaller absorption cross-section of the QD compared to bulk GaAs. However, the excitation energy still differs from the emission energy of the QD and therefore spectral filtering between both signals remains possible in the case of a confocal setup. Quasi-resonant excitation usually leads to cleaner spectra with lower background emission.

2.3.3   Resonant excitation

In this scheme, the energy of the pump source exactly matches the energy of the QD s-shell so that carriers are directly photo-excited in their lowest energy configuration. This excitation scheme presents the same advantages as quasi-resonant excitation. Moreover, no relaxation mechanism is needed in the case of resonant excitation, which reduces the uncertainty in the emission time of the photon. The major issue with resonant excitation is the discrimination between the pump signal and the emission of the QD. Indeed, the scheme requires high pump power that cannot directly be filtered away spectrally in a confocal setup. A possible solution consists in exciting the QD in-plane while collecting its emission out of the plane [54]. Another solution, which will be used in this thesis, is to apply an electric-field modulation after the excitation process to Stark shift the energy of the s-shell in order to spectrally filter the excitation light.

2.4   Carriers in a quantum dot

The maximum number of confined carriers in a QD depends mostly on the size of the QD, the height of the confining potential barrier and the effective mass of the confined carriers, larger QDs or those with deeper confining barrier or heavier carriers being capable of confining more carriers. For the

growth conditions used in this thesis, the QDs usually confine one spin-degenerate electron level and two spin-degenerate hole levels (i.e. a maximum of six carriers). Each energy level in the QD can be occupied by maximum two carriers with opposite spins in agreement with Pauli's exclusion principle and the lowest energy levels are typically occupied first (at least in thermal equilibrium at low temperature).

2.4.1 Quantum dot states

Different states of a QD can be distinguished depending on the number of carriers in each band and on their spin orientation s (for electrons) and hybridized angular momentum projection and spin orientation $j = l + s$ (for holes).

An important state of a QD is the neutral exciton state X, resulting from the binding of an electron in the conduction band with a hole in the valence band leading to a Coulomb-correlated electron-hole pair. Two types of neutral excitons can be distinguished depending on the total angular momentum of the system. Indeed, the heavy hole has a total azimuthal angular momentum of $j_z = \pm 3/2$ [55] (usually referred as the "hole spin") and an electron has a spin projection $s_z = \pm 1/2$. Therefore, a neutral exciton can have a total angular momentum $m = s_z + j_z$, which can have any one of four values +2,-2,+1,-1. Due to the conservation of total angular momentum, only excitons with $m = \pm 1$ can decay to the ground state $|0\rangle$ (empty QD) through emission of a single photon. Such excitons are therefore known as bright excitons (labelled X_b), while excitons with $m = \pm 2$ are called dark excitons (labelled X_d). Dark excitons could decay via a pair of photons but as there is no intermediate energy levels this process is highly suppressed.

Another important state is the biexciton XX, which consists of a pair of electrons and a pair of holes with anti-aligned spins. This is the only possible biexciton spin ground state in agreement with Pauli's exclusion principle. Finally, other states consist of X or XX states with additional carriers (either electrons or holes) confined in the QD as well. The states are then referred as positively or negatively charged states depending on whether the additional
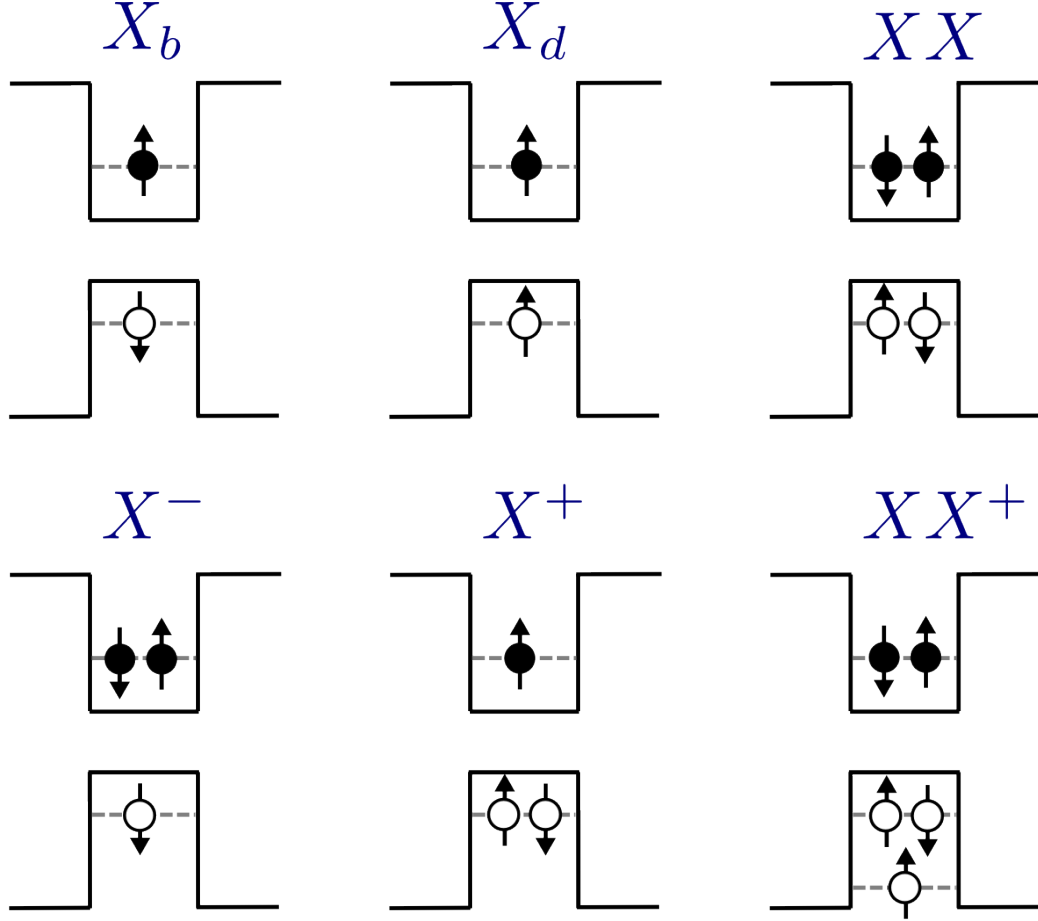
Figure 2.3: Schematic representation of various lowest energy states of a QD: the bright exciton X_b, the dark exciton X_d, the biexciton XX, the negatively charged exciton X^-, the positively charged exciton X^+, and the positively charged biexciton XX^+. Arrows indicate the directions of the electron's spin s and the hole's angular momentum j.

carriers are respectively holes or electrons. An illustration of examples of the lowest energy states discussed above is given in Fig. 2.3.

2.4.2 Quantum dot fine structure

As mentioned above, two types of neutral excitons can be distinguished depending on the total angular momentum of the QD m. With negligible interactions between the electron's spin s_z and the hole's spin j_z, the exciton state

would be four-fold degenerate. However, when the electron's spin and hole's spin interactions are considered, the exciton state split into two pairs of two fold degenerate states, the states for which $m = \pm 2$ having lower energy due to the exchange interaction. Finally, asymmetry must be considered as well to have a more realistic picture of the electronic structure of QDs. Indeed, circular symmetry of the QD has been assumed so far and no anisotropic external fields have been considered. In practice, asymmetry originates in a QD from several mechanisms such as physical elongation of the base of a QD or strain field inside the QD and piezoelectricity of the bulk material usually leads to a small inbuilt electric field [47, 56]. In an asymmetric QD, bright and dark excitons are therefore no longer degenerate and both split into two non-degenerate states. This splitting can nevertheless be controlled in different ways and reduced to zero, leading to emission of polarisation-entangled photon pairs [57, 58]. As the lowest energy state of the biexciton is spin neutral it has no spin-splitting arising from the exchange interaction induced by asymmetry of the confining potential. The biexciton consists therefore in a single non-degenerate state. A simplified energy diagram illustrating the different effects discussed is shown in Fig. 2.4.

2.5   Quantum dot molecules

The coupling between single QDs has become a fruitful new area of research for the past few years [59, 60], motivated both by the fundamental physical mechanisms of coupling between QDs and by possible applications in opto-electronics and quantum information technologies. Because of the strain-field generated by the lattice mismatch between different semiconductor materials, QDs grown successively on top of each other tend to align vertically [61, 62], which leads to the formation of coupled QDs also known as quantum dot molecules (QDMs). The system used in this thesis consists of a pair of InAs QDs separated in the growth direction by a barrier of controllable thickness typically of several nanometers and made of the bulk material (GaAs) in which the QDs are embedded. A schematic band diagram of a QDM is given in Fig. 2.5. The top QD is usually larger than the bottom one as its growth
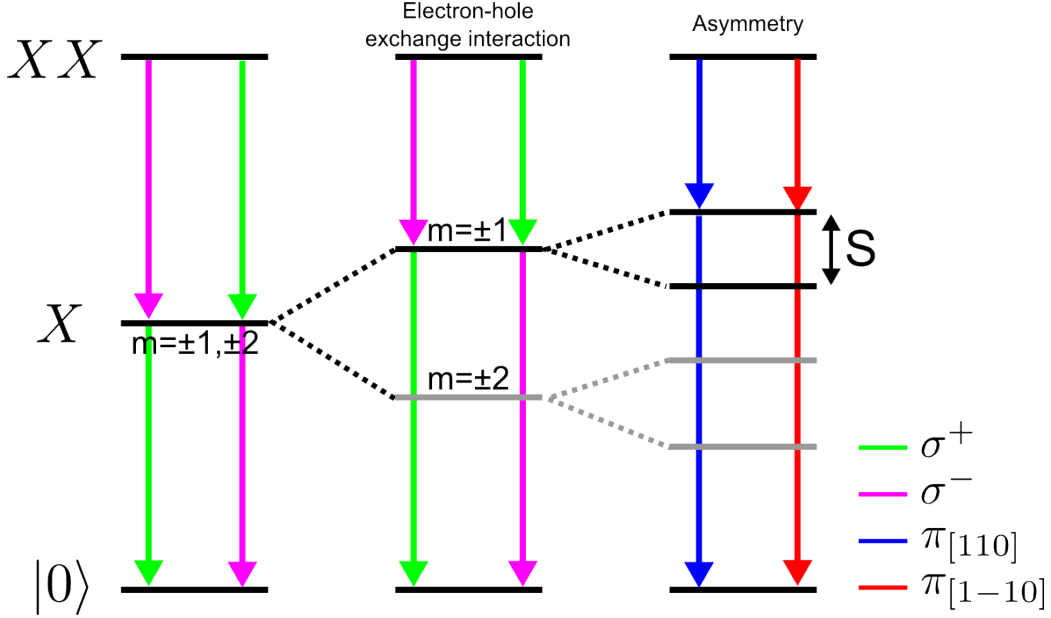
Figure 2.4: Energy levels of a single QD and effects of the exchange interaction and asymmetry of the QD on the four exciton states $m = \pm 1, \pm 2$. Allowed optical transitions are shown along with the polarisation of the emitted photons: σ corresponds to circularly polarised photon ($+$ is right hand, $-$ is left hand) and π to linearly polarised photons ([110] and [110] are the crystal axes). The fine structure spin splitting between the two bright states is labelled S.

is triggered by the strain field from the first layer of QDs [63, 64]. This leads to lower energy levels for the top QD as illustrated in Fig. 2.5.

Even within the case of small QDs in which only one or two excitons can be confined, the number of possible states of a QDM structure are considerably higher than in the case of single QDs. Indeed, QDMs allow for quantum tunneling of holes and electrons between the QDs when electric fields are applied such that resonances appear in the energy level structure. Quantum tunneling must here be understood as the nanoscopic quantum phenomenon in which a particle may penetrate a potential barrier higher than the kinetic energy of the particle, which violates the principles of classical mechanics. As a consequence, two main classes of optical transitions can be distinguished in a QDM: "direct" or "intradot" transitions where the recombining carriers (forming a direct exciton) are in the same QD and "indirect" or "interdot"
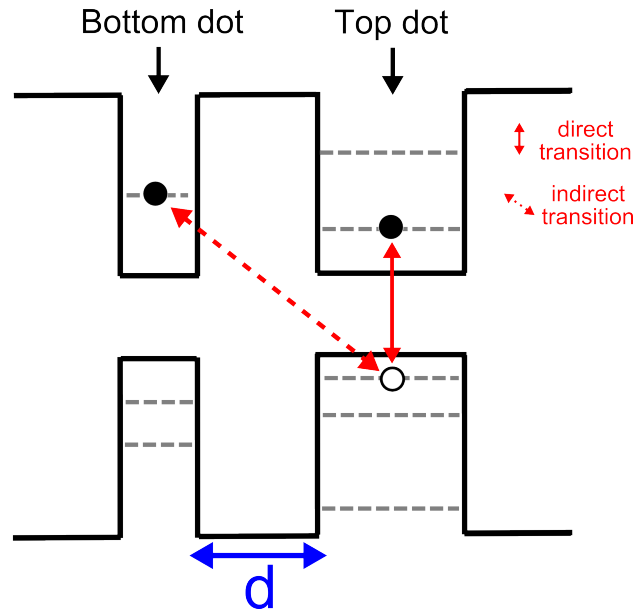
Figure 2.5: Simplified band diagram of an InAs QDM embedded in GaAs. The top QD is strain-induced and therefore larger than the bottom QD, resulting in lower (higher) energy levels for the electron (hole). One electron and one hole are represented in the bottom QD and one electron in the top QD. Direct (indirect) transitions are optical transitions originating from the radiative recombination of carriers trapped within the same (different) QDs.

transitions where the carriers (forming an indirect exciton) are distributed across the QDM (see Fig. 2.5). The different possible optical transitions of a QDM originating from the neutral exciton and biexciton states as well as from the charged states will be discussed in detail in chapter 5.

Chapter 3

Experimental methods

In this chapter, we discuss the different experimental methods and fabrication techniques used to prepare our quantum devices based on semiconductor quantum dots (QDs). We also present the optical measurements performed to obtain the results shown in the following chapters.

3.1 Sample preparation

3.1.1 Quantum dot growth

QDs can be produced in many ways through the creation of a 3-dimensional modulation, which is of the correct size to confine the carriers on a length scale smaller than the de Broglie wavelength. Typical examples of fabrication methods include electric-field modulation, etching, interface fluctuations [57], and self-assembly [65]. This research focuses on self-assembled InAs QDs in GaAs grown by molecular beam epitaxy [66].

The principle behind self-assembly works as the following (see Fig. 3.1). A thin layer of a semiconductor single crystal (such as InAs) is slowly grown on top of another semiconductor with a different lattice constant (such as GaAs). After a few monolayers have been deposited (1.6 monolayers in the case of InAs atop of GaAs), the strain brought by the lattice mismatch between the two semiconductors involved causes the deposited layer to break up into small islands and form dome-shaped or pyramidal QDs typically
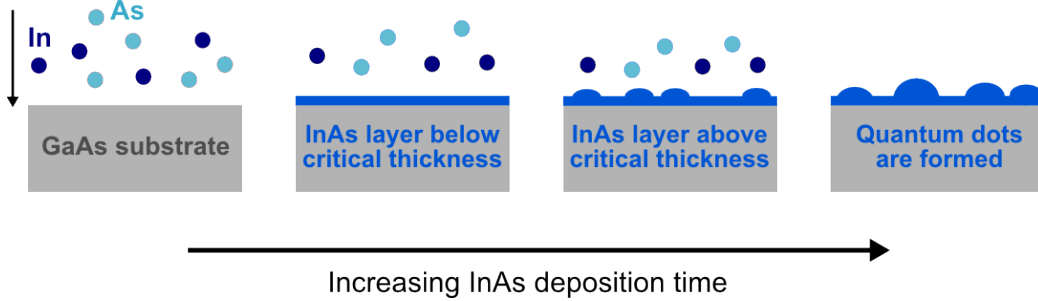
Figure 3.1: Growth of self-assembled InAs QDs using the Stranski-Krastanov growth method. Atoms of In and As are deposited on the GaAs substrate progressively forming the so-called "wetting layer". Once the wetting layer has reached the critical thickness, the strain originating from the lattice constant mismatch between the different materials is released through the formation of QDs.

around 20-30nm in diameter and 5nm high. This is known as the Stranski-Krastanov (SK) growth technique [65, 67, 68]. A typical example of InAs QDs grown on GaAs is shown in Fig. 3.2. The exact shape and size of QDs formed using the SK growth technique strongly depends on both the material used and the exact growth conditions, which therefore influence the physical properties of the QDs such as the number of carriers in a QD or the energy levels in the band structure. Other techniques to fabricate self-assembled QDs than the SK growth method presented here can be found in [65].

Quantum dot molecules (QDMs) are formed following the process shown in Fig. 3.3. A thin spacer of GaAs of thickness d ($\approx$1-20nm) is deposited on top of a first layer of InAs QDs. A second layer of InAs QDs is then grown on top of the GaAs. Due to the strain field generated from the first layer of QDs, which "seeds" the growth of the second layer [61, 62, 63, 64], QDs from the second layer are vertically self-aligned with the first layer and larger than QDs from the first layer.

InAs based self-assembled QDs are well adapted for potential applications in quantum information because of their long coherence time [69] and good control over the growth process, notably leading to coupled structures such as those studied here or positioning of the QDs, which is a condition for scalability. Other common examples of material systems used to create QDs
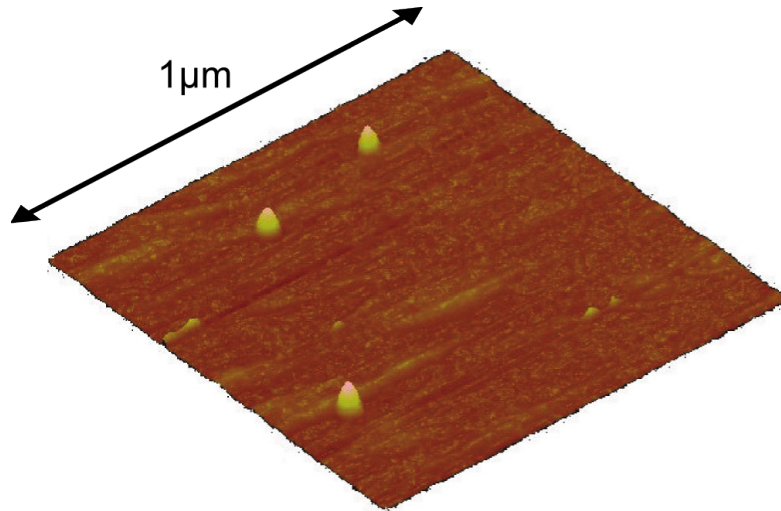
Figure 3.2: An atomic force microscope image of the surface of a sample grown with a layer of InAs QDs on top of GaAs. The dot density is $\approx$1-10μm^{-2}.
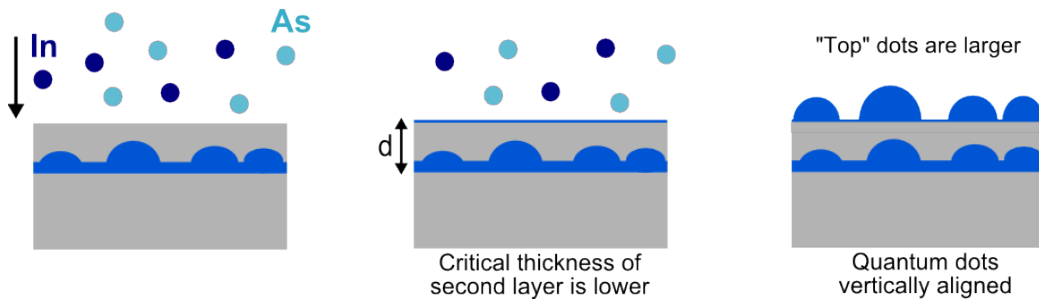
Figure 3.3: Growth of InAs QDMs separated by a GaAs layer of thickness d. The strain field generated by the lower (bottom) layer of QDs triggers the growth of the upper (top) layer of QDs. As a consequence, the wetting layer from the upper (top) layer is thinner and the QDs are larger and vertically aligned with the bottom QDs.

include GaAs/InP, Ge/Si, CdSe/ZnSe and InN/GaN [65].

3.1.2 Semiconductor microcavities

An important advantage of semiconductor QDs is their fairly easy integration into optical cavities in order to control the spatial localization of light and increase the amount of emitted light collected. Indeed, due to the large
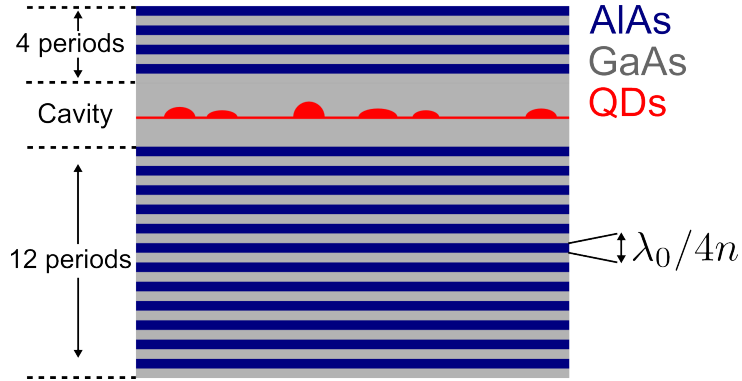
Figure 3.4: Example of a planar microcavity containing 12 DBR periods at the bottom of the cavity containing the QDs and 4 DBR periods at the top. This design is representative of the devices used in this thesis.

difference between the large refractive index (n) of III-V semiconductors ($n = 3.54$ for GaAs at a wavelength of $1\mu m$) and the refractive index of air, only $\approx 1 - 5\%$ of the light from from a QD is emitted out of a bare wafer [70]. Examples of structures where the emission is increased due to its coupling to the mode of a cavity include planar microcavities, micropillars, microdisks, and two-dimensional photonic crystals [71, 72].

In this work, we will restrict ourselves to the use of planar Fabry-Pérot microcavities consisting of two distributed Bragg reflectors (DBRs) surrounding the cavity region made of a GaAs spacer layer containing the QDs. Each DBR consists of alternating layers of high- and low-refractive index materials (respectively GaAs with $n = 3.54$ and AlAs $n = 2.97$ in our case), the thickness of which is equal to $\lambda_0/4n$, where λ_0 is the design wavelength of the cavity and λ_0/n is the optical wavelength in the material. The length of the GaAs cavity is usually an integer number of one (or one half) optical wavelengths. One pair of GaAs and AlAs layers corresponds to one period in the DBR. A typical planar microcavity is represented in Fig. 3.4.

Optical waves travelling through the DBR structure experience partial reflections and transmissions at the interfaces between the high- and low-refractive indices layers. As a consequence, backward and forward travelling waves will interfere constructively or destructively depending on the wavelength. Wavelengths around λ_0 will constructively interfere resulting in a
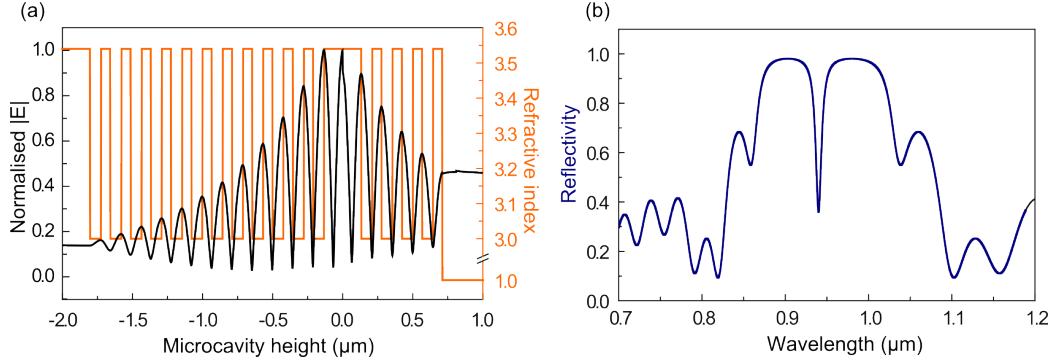
Figure 3.5: (a) Electric field profile of a mode confined in a planar microcavity designed for $\lambda_0 = 940nm$ and made of 12(4) DBR periods at the bottom (the top). Modulation of the refractive index due the alternative layers of GaAs and AlGaAs is also shown. (b) Reflectivity profile of the structure showing a dip at $\lambda_0 = 940nm$. Image taken from [74].

region of high reflectivity centered on λ_0 known as the stopband. The presence of the cavity layer causes a narrow transmission window (the cavity mode) to open in the stopband at λ_0. The exact reflectivity profile of the structure and the sharpness of the cavity mode depend on the number of mirror periods and the materials. A typical example of the electric field and reflectivity profiles is shown in Fig. 3.5 for the structure in Fig. 3.4. Importantly, using microcavity structures such as those presented here significantly increases the collection efficiency by modifying the angular emission profile with more light being directed to the surface of the device [73].

3.1.3 Device fabrication

The majority of the results in this thesis were obtained by applying vertical electric fields across the QDs. To do so, QDs inside microcavities were incorporated in electrical devices consisting of *p-i-n* diode heterostructures grown by molecular beam epitaxy. The typical design of these devices is illustrated in Fig. 3.6.

A single layer of InAs QDs (two layers separated by few nanometres in the case of QDMs) with dot density $<1\mu m^{-2}$ was grown at the centre of the intrinsic region made of a GaAs quantum well clad with a short period

superlattice equivalent to $Al_{0.75}Ga_{0.25}As$ on each side, which prevents tunneling of the carriers out of the dot region when the structure is biased. The QDs inside the barriers were encased in a weak planar microcavity made of two DBRs respectively on top and bottom of the dot layer. The three periods of the DBRs adjacent to the superlattice were doped with concentration $\approx 10^{18}cm^{-3}$. Doping was extended into the superlattice and allowed for application of an electric field along the growth direction. The electric field F was calculated using $F = \left(\frac{V-V_{bi}}{d}\right)$, where V is the bias applied to the structure, V_{bi} is the built-in potential and d is the thickness of the intrinsic region. A shallow ohmic contact on top the device was formed using a 5nm thick GaAs layer heavily doped with a concentration $\approx 10^{20}cm^{-3}$.

Even though QDs grown using the SK method tend to form along surface features, their positions are random on the micron scale. Techniques allowing isolation and relocation of QDs are needed to be able to reproduce experimental measurements at any time or to perform new measurements on a previously studied QD. The technique used here involves an aperture mask made of an opaque material (such as Aluminium) on top of the sample. The thickness of the metal mask was typically around 60nm. Excitation and photon collection occured through this opaque metallic film on the sample surface patterned with micron-diameter apertures.

We used standard photolithography and wet etching techniques to fabricate diodes of two different sizes. Large diodes had lateral dimensions of 360μm$\times360\mu$m while small diodes had lateral dimensions of 35μm$\times60\mu$m. The main advantage of small diodes is their lower capacitance leading to much shorter electrical response time. These were therefore used for experiments requiring high-speed modulation of the electric field. In other cases, large diodes were usually preferred as they contained more apertures and therefore more QDs to be studied within the same device. A top view of a typical large device patterned with an array of 100×100 apertures is shown in Fig. 3.7.
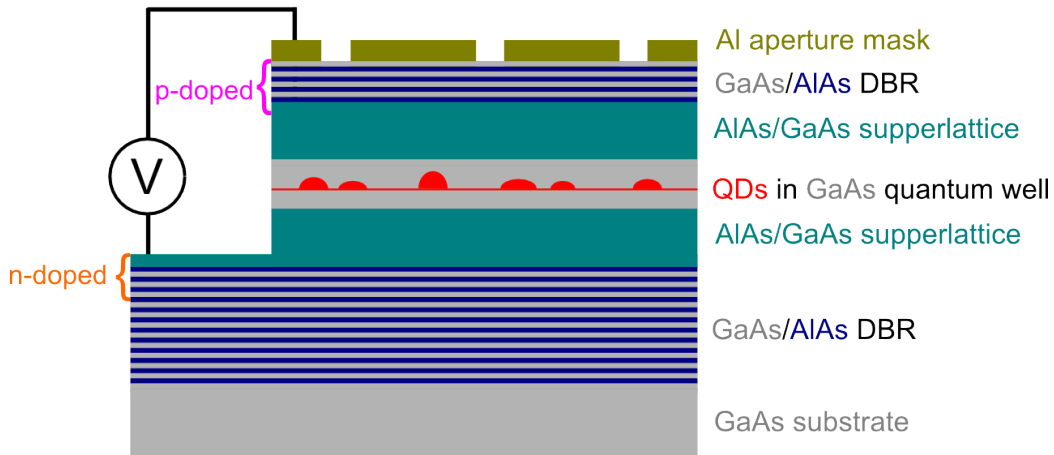
Figure 3.6: Illustration of the structure of the devices used to study the behaviour of QDs under an electric field. The QD layer is sandwiched between AlAs/GaAs superlattice tunnel barriers to prevent optically excited excitons from leaving the system when an electric field is applied between the n- and p-doped layers. An aluminium mask containing circular apertures is deposited on top to allow for isolation and relocation of QDs.
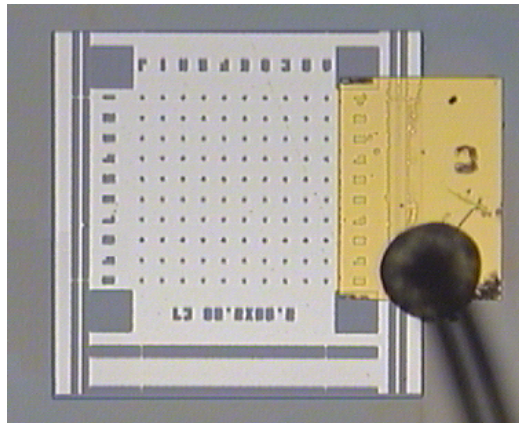
Figure 3.7: optical image of an aperture mask consisting of an array of 100×100 circular holes. The gold contact on which a thin black wire is connected constitutes the p-contact of the device.

3.2 Optical measurements

Once devices are processed from grown wafers and suitable QDs and QDMs are found, the optical and quantum properties were measured using a battery
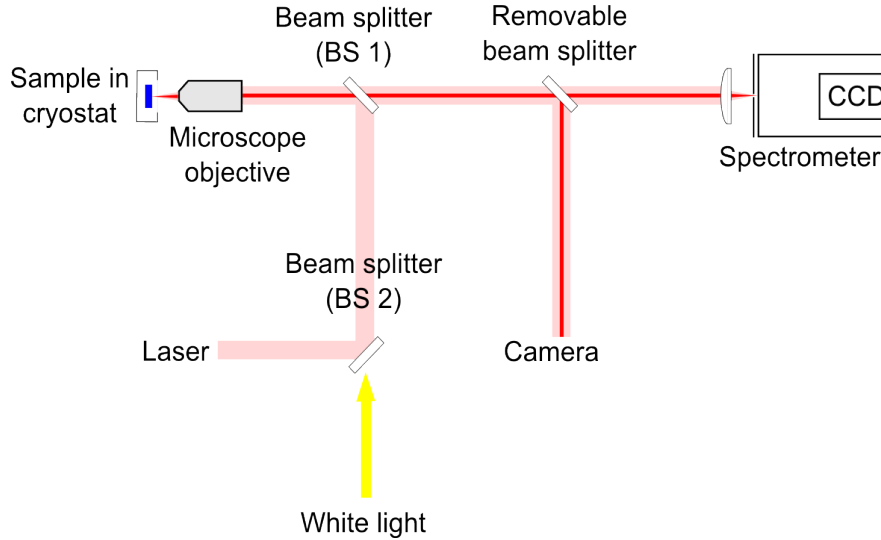
Figure 3.8: Schematic of the experimental setup used to measure photoluminescence spectra from single QDs and QDMs.

of methods described in this section. Most of the equipment were computer-controlled using customised softwares allowing different parameters of a particular experiment to be scanned and measured.

3.2.1 Micro-photoluminescence spectroscopy

A schematic of the experimental setup used to measure the wavelength-resolved photoluminescence of QDMs is shown in Fig. 3.8.

Our samples were optically excited using either a pulsed diode laser or a Ti:Sapphire laser. The diode laser operated at 870nm with a tunable repetition rate up to 80MHz and a pulse width <100ps. In some experiments, this laser was externally triggered using a pulse pattern generator. The Ti:Sapphire laser had a fixed repetition rate of 80MHz mode-locked and a tunable wavelength emission from 700nm to 1080nm. The Ti:Sapphire laser was pumped with a CW laser emitting at 532nm with a power of 5W. This system produced pulses of width below 10ps.

The laser beam was focused on the sample surface to an approximately $1\mu m^2$ spot using a long working distance microscope objective with a numerical aperture of 0.42 and a $\times 50$ magnification. The microscope objective

was mounted on a XYZ stage to allow easy traversal of the sample surface and focusing of the laser. Photoluminescence from the sample was collected using the same objective in a coaxial arrangement.

A beam splitter (BS1) was used to separate the light coming from the laser and the outgoing photoluminescence from the sample. A second beam splitter (BS2) was used to combine white light co-linearly with the laser beam to enable visual access to the sample surface. The light was focused to the same location on the sample as the laser light and its reflection was collected using the same microscope objective.

A third (removable) beam splitter was added in the path of the light collected by the objective and directed the white-light image of the sample surface to a video camera for imaging and alignment purposes. The white light was turned off and the beam splitter removed once the system was aligned to avoid external perturbations and maximise the photoluminescence intensity entering the spectrometer.

The samples were mounted into a continuous flow He-cryostat and cooled down to below 10K. The sample temperature was controlled using the an accompanying temperature controller. The cryostat provided excellent sample stability as it was designed to have ultra-low in-plane sample drift and vibrations of less than $0.1\mu m$. The samples were mounted in high vacuum on top of a cold finger using silver paint to provide a good thermal link. A thin 0.5mm window provided optical access and the sample was placed within a few mm from this window, which allowed the use of the high magnification microscope objective lens.

Finally, photoluminescence was collected by a single stage spectrometer with a cavity length of 64cm inside which two reflective diffraction gratings were used. A coarse grating (600mm^{-1} with a resolution of $\approx100\mu$m) was used for low resolution measurements allowing observations on a wide range of wavelength and a finer grating (1800mm^{-1} with a resolution of $\approx30\mu$m)) was used for high resolution measurements on a small range of wavelength. A variable width and height entrance slit was used to reduce the entrance angle into the spectrometer. A charged coupled device (CCD) consisting of an array of 1024×256 of $26\mu m^2$ pixels was used to detect the light dispersed
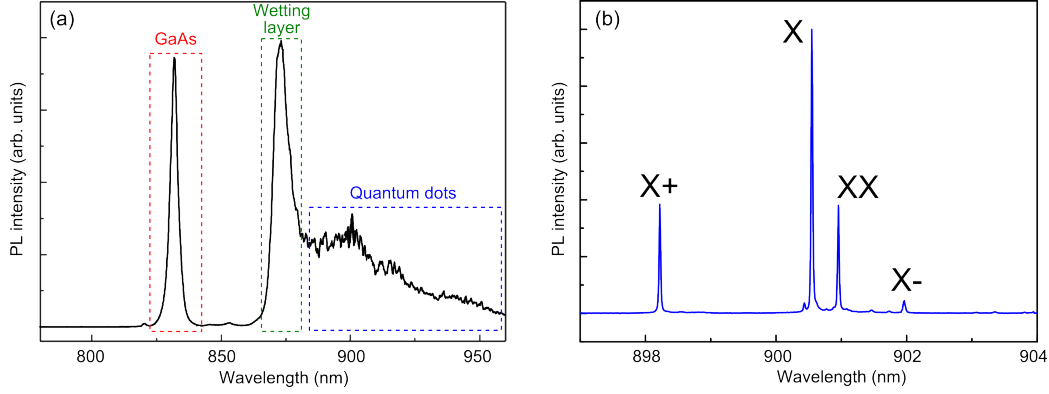
Figure 3.9: (a) Typical optical spectrum obtained with the setup presented in Fig. 3.8, showing emission from GaAs impurities, from the wetting layer, and from a large number of QDs located below the aperture under investigation. (b) Optical spectrum showing emission from different states of a single QD on a finer wavelength scale, obtained by using a high-resolution spectrometer and a sample with reduced dot density compared to the sample used to obtain (a).

by the spectrometer and kept at around 140K using liquid nitrogen to reduce background noise.

Fig. 3.9(a) shows the full spectrum from a sample with a high dot density obtained with our setup. Three regions can be distinguished. An emission peak at lower wavelength arises from the recombination of excitons bound to impurities in GaAs [75]. Another peak is associated with emission from the wetting layer, which behaves like a quantum well [47]. Finally, the sharper peaks found at higher wavelengths and forming hairy features correspond to emission from QDs. Both their ability to confine carriers in three dimensions and their relatively long lifetime on the nanosecond timescale leads to sharp lines, which are resolution limited by the coarse grating in the spectrometer.

Fig. 3.9(b) shows a typical high-resolution spectrum obtained with a sample with low dot density containing emission peaks from different states of a single QD: the neutral exciton (X) and biexciton (XX), the positively charged (X+) exciton and the negatively charged exciton (X-). These different transitions can be identified using mainly two methods. First, as described in section 2.4.2, the bright neutral exciton eigenstates are split in energy, which
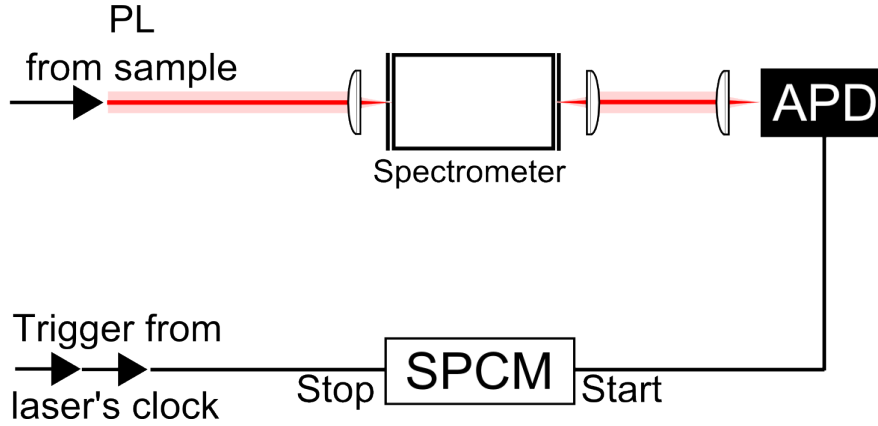
Figure 3.10: Schematic of the experimental setup used to measure time-resolved photoluminescence from single QDs and QDMs. SPCM holds for Single Photon Counting Module and APD for Avalanche Photodiode.

results in a linear polarisation splitting between the exciton and the biexciton. This splitting can be experimentally measured using half-wave plates [57] and permits to distinguish between neutral and charged states. Secondly, the dependence of the integrated intensity of a QD emission line with laser pump power provides information about the excitonic state. Indeed, each photon absorbed by the semiconductor material will create a single electron-hole pair that will relax into the QD and recombine to emit a single photon. The total integrated intensity is therefore expected to vary linearly with pump power for the exciton state. If the probability of an exciton capture at a laser power P is denoted p_P, capture of a biexciton will occur with a probability p_P^2 and a quadratic dependence with laser power is expected for the biexciton state [16]. Finally, the different charged states are identified using their energy shift from neutral states originating from Coulomb interactions, with X+ (X-) emission lines measured at lower (higher) wavelength.

3.2.2   Time-resolved spectroscopy

The photoluminescence from a single emission energy (within the resolution limit of the grating used) of a QD can be time-resolved using the setup shown in Fig. 3.10.

The photoluminescence light collected into the spectrometer and dispersed by the grating is no longer directed into a CCD (as shown in Fig. 3.8), but instead out of the spectrometer lateral exit port and through a second variable width and height slit. The emission is then focused into a single photon counting module (SPCM) using a thermoelectrically cooled and temperature controlled silicon avalanche photodiode (APD), which is roughly 40% efficient at 900nm. The laser clock is also connected to a SPCM counter card. The principle of lifetime measurement works in the following way: the SPCM card measures the time between a reference pulse from the laser and a photon being detected at the chosen wavelength. A histogram of the distribution of time intervals measured is built up as the card collates measurement at the clock rate of the pulsed laser exciting the QD (see Fig. 3.11). The width of each time bin is dependent on the resolution of the SPCM card which is typically 50ps. The radiative lifetime τ_r of the QD state under investigation is deduced from the histogram by fitting directly the exponential decay according to the first-order equation of photon counts

$$N(t) = N(0)e^{-\frac{t}{\tau_r}}, \tag{3.1}$$

where $N(t)$ is the number of photons detected by the SPCM at time t.

3.2.3 Magneto-photoluminescence spectroscopy

Some of the results presented in this thesis involved the application of a magnetic field to the sample. A magnetic field applied to a QD introduces Zeeman interactions between the spins of carriers and the magnetic field [76]. The effects are highly dependent on the orientation of the field due to the asymmetry of the QD. Two particular orientations are usually considered when studying the response of a QD to an external magnetic field. The first orientation, called the Voigt geometry, is with the magnetic field in the plane of the sample, parallel to the exciton dipole. The second orientation, known as the Faraday geometry, is with the magnetic field in the growth direction. A magnetic field in the Voigt geometry couples the bright and dark exciton states and can be used for instance to control the fine structure splitting [77].
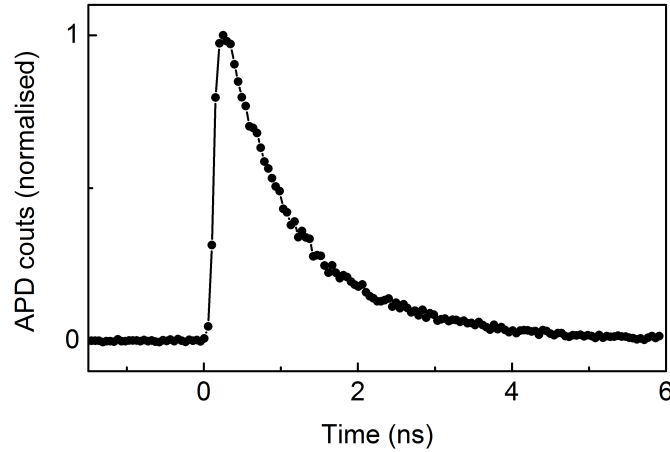
Figure 3.11: Typical time-resolved photoluminescence signal from a single QD showing an exponential decay of the emission with time.

In some cases, it can reduce the value of the fine structure so that entangled pairs of photons are produced [21]. In this thesis, we only consider magnetic fields in the Faraday geometry where the Zeeman interaction creates pure spin eigenstates with an energy splitting directly proportional to the field.

A magnetic field was applied to the sample using a continuous-flow cryostat surrounded by a superconducting magnet with a range up to 5T. The sample was mounted on a cold finger and the whole provided a cryogenic environment with good spatial stability . The geometry of the magnet cryostat was similar to the geometry of the cryostat used for micro-photoluminescence spectroscopy resulting in easy integration with optical components.

3.2.4 Photoluminescence excitation spectroscopy

Photoluminescence excitation spectroscopy was used to find the different energy levels of a QD and excite carriers quasi-resonantly. This was made possible using the wavelength tunability of the Ti:Sapphire laser. Indeed, a birefringent filter consisting of crystalline quartz plates cut parallel to their optical axes is placed within the laser cavity at Brewster's angle. As a con-
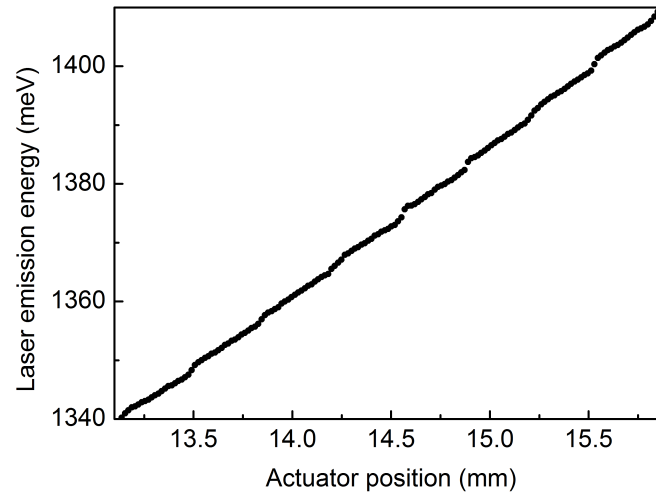
Figure 3.12: Laser emission energy plotted as a function of actuator position. The actuator was motorised and its position was computer-controlled with a micrometre-scale precision.

sequence, only a narrow range of wavelengths linearly polarized reach lasing threshold. Rotating the filter about an axis normal to the plates changes these wavelengths and allows the output wavelength to be tuned. This rotation was induced by changing the position of a computer-controlled motorised actuator (see Fig. 3.12). Small departures from linear dependence between the actuator position and the laser emission energy seen on Fig. 3.12 are due to mode hopping of the laser.

The excitation energy of the laser was typically tuned from below the s-shell energy up to the energy of the wetting layer. Photoluminescence was then observed only for specific values of the laser energy corresponding to various resonances of the QD such as the p-shell or phonon resonances, which will be used in this thesis.

Chapter 4

All-electrical coherent control of an exciton qubit in a single quantum dot

4.1 Introduction

As discussed in chapter 1, emerging quantum technologies such as quantum computing and quantum cryptography promise to revolutionise the way information is processed by controlling quantum bits or "qubits" in two-level quantum systems [4, 3]. Photonic "flying" qubits are used for quantum communication [33, 34, 35] as they easily travel in space or through standard optical fibres while solid-state "stationary" qubits are usually more convenient to perform quantum computations [36, 37, 38, 30]. These two embodiments have thus far been developed independently, but coherent control of both types of qubits and coherent transfer of quantum information between them are necessary to extend the potential of quantum technologies [78].

Optical absorption of photons in a semiconductor to create an electron-hole pair (or exciton) provides a natural mechanism to initialise a stationary qubit. Selection rules and conservation of angular momentum determine the mapping of the photon polarisation onto the spin state of the exciton. Once initialised manipulation of solid-state spins has been achieved with pulsed

magnetic fields at milli-kelvin temperatures [37] or coherent optical beams [38, 30] and is theoretically achievable using couplings to localised optical modes [79]. However, these techniques require bulky setups or synchronized lasers, making them somewhat impractical and incompatible with large-scale applications. New methods to control these qubits based on scalable, low-cost, well-established semiconductor light-emitting diode structures will be advantageous when it comes to controlling large numbers of qubits.

In this chapter, we advocate using the spin-state of an exciton trapped in a self-assembled semiconductor quantum dot (QD) as an electrically-controllable qubit in which quantum information from flying qubits can be efficiently transferred and easily restored. We start by describing the coherent coupling of the exciton eigenstates that is induced by a vertical electric field and characterising the device and the QD used in our experiments. We then discuss the initialisation of the exciton spin state, its time evolution, and the fidelity of the reversible transfer of quantum information from a photonic qubit into a solid-state qubit. Finally, we demonstrate high-fidelity phase-shift and spin-flip gate operations using subnanosecond dynamical modulation of the electric field to manipulate the exciton spin.

4.2 Electrical coherent coupling of the exciton states

An exciton has two optically-active spin eigenstates energetically separated by a fine-structure splitting (s) resulting from the exchange interaction [80, 81]. When the magnitude of s is large, the two bright exciton eigenstates in the QD can be seen as oppositely-polarised radiating dipoles aligned along the [110] and $[1\bar{1}0]$ crystal axes. This orientation is mapped onto the linear polarisation of photons to which the eigenstates couple. We use the notation $|X_H\rangle$ and $|X_V\rangle$ to refer to the spin eigenstates, where H and V are the horizontal and vertical orientations in the lab-frame respectively defined by the crystal axes [110] and $[1\bar{1}0]$ (see Fig. 4.1(a) and inset in Fig. 4.1(d)).

Controlling the magnitude of s is of great interest as it leads to the emis-

sion of polarisation-entangled photon pairs when reduced below the linewidth of the biexciton-to-exciton-to-empty cascade [21, 82]. It has recently been discovered [58] that the magnitude of s and the orientation of the eigenstates can be controlled via an applied vertical electric field, which is one of the most practical methods to tune s among those yet reported [77, 83, 84, 85, 86].

The magnitude of s and the orientation of the eigenstates are determined by the electron-hole exchange interaction in combination with an in-plane asymmetry in the confining potential in terms of strain, piezoelectric fields, shape and composition as well as the crystal inversion asymmetry. Moreover, QDs are lens or pyramid shaped rather than cylindrical and therefore the strain and piezoelectric fields vary from the bottom to the top of the dot. By shifting the electron and hole wave functions along the growth direction with a vertical electrical field the in-plane asymmetry at the wave function overlap can be modified, eventually leading to a coupling between the basis states with dissimilar spin. In fact, such a coupling has also been observed when s is tuned using external stress [87, 88] and can always be expected if the symmetry is lower than C_{2v} [89].

The evolution of s and the orientation of the eigenstates when an electric field is applied is well described by the empirical model developed in [58]. Using the natural basis $\{|X_H\rangle, |X_V\rangle\}$ aligned with the crystal axes, the Hamiltonian describing the evolution of the eigenstates in matrix representation is

$$\begin{pmatrix} E_H & s_0/2 \\ s_0/2 & E_H - \gamma(F - F_0) \end{pmatrix}, \tag{4.1}$$

where E_H is the energy of the exciton state $|X_H\rangle$, $s_0/2$ is a coupling term between the basis states $\{|X_H\rangle, |X_V\rangle\}$, F is the electric field, F_0 is the field at minimal splitting, and γ is the rate at which the splitting between the energy levels varies in the absence of the coupling term $s_0/2$. The eigenstates $|X_\pm\rangle$ of this Hamiltonian are the symmetric and antisymmetric coherent superpositions of the basis states

$$|X_+\rangle = \cos\theta\,|X_H\rangle + \sin\theta\,|X_V\rangle\,, \qquad (4.2)$$

$$|X_-\rangle = \sin\theta\,|X_H\rangle - \cos\theta\,|X_V\rangle\,, \qquad (4.3)$$

where θ is a real angle that describes the orientation of the eigenstates relative to the crystal lattice (see inset in Fig. 4.1(d)). The eigenvalues $E_\pm$ and θ are given by

$$E_\pm = E_H - \frac{\gamma(F-F_0)}{2} \pm \frac{1}{2}\sqrt{\gamma^2(F-F_0)^2 + s_0^2}, \qquad (4.4)$$

$$\theta = \tan^{-1}\left[\frac{(E_+ - E_-) - \gamma(F-F_0)}{s_0}\right], \qquad (4.5)$$

which leads to a splitting

$$|s| = |E_+ - E_-| = \sqrt{\gamma^2(F-F_0)^2 + s_0^2}. \qquad (4.6)$$

The coupling term $s_0/2$ leads to an anticrossing in the energies $E_\pm$ of the eigenstates (see Fig. 4.1(b)), the size of which determines the minimal splitting s_0 (see Fig. 4.1(c)), and induces a continuous a rotation of their orientation θ (see Fig. 4.1(d)).

Further discussion on how the coupling term $s_0/2$ varies from QD to QD, with temperature or laser power can be found in [58], along with a discussion on how to use the electrical tunability of the fine structure splitting to control the entanglement between two photons.

4.3 Device and quantum dot characteristics

The *p-i-n* heterostructure used for our experiment is schematically represented in Fig. 4.2(a). A single layer of InAs QDs with dot density $<1\mu\mathrm{m}^{-2}$ was grown at the center of the intrinsic region made of a 10nm GaAs quantum well. To apply large electric fields while avoiding tunneling of the carriers out of the dot region, the intrinsic region is clad with a short period superlattice
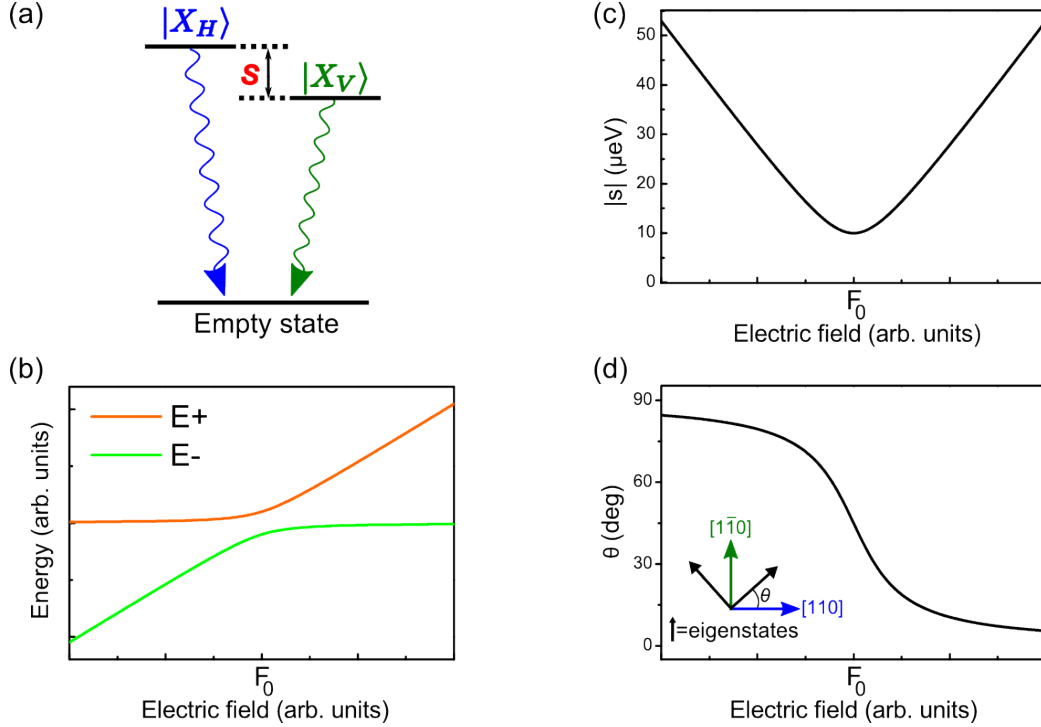
Figure 4.1: (a) Schematic energy diagram of the neutral exciton states in a single QD. (b) Eigenenergies $E_\pm$ as a function of electric field showing an anticrossing of size s_0 at F_0. (c) Magnitude of s and (d) θ as a function of electric field. The curves in (b), (c), and (d) were obtained using Eq. (4.1) with the parameters $s_0 = 10\mu eV$ and $\gamma = -0.26\mu eV\,kV^{-1}cm$.

equivalent to $Al_{0.75}Ga_{0.25}As$ on each side. Doping extends into the super-lattice and allows application of an electric field along the growth direction. The electric field F is calculated using $F = \left(\frac{V-V_{bi}}{d}\right)$, where V is the bias applied to the structure, $V_{bi}=2.2V$ is the built-in potential and $d=140$nm is the thickness of the intrinsic region. This *p-i-n* device is encased in a weak planar microcavity consisting of 14 (4) periods below (above) the dot layer.

The electric field dependence of the exciton and biexciton states of our QD is shown in Fig. 4.2(b). The energy of the different exciton states depends mainly on the Coulomb interaction between the involved charges. Which line belongs to which exciton complex can be understood from their respective power dependence and fine structure. We find that in our samples X and XX are separated by a few meV with XX on the low energy side. The charged
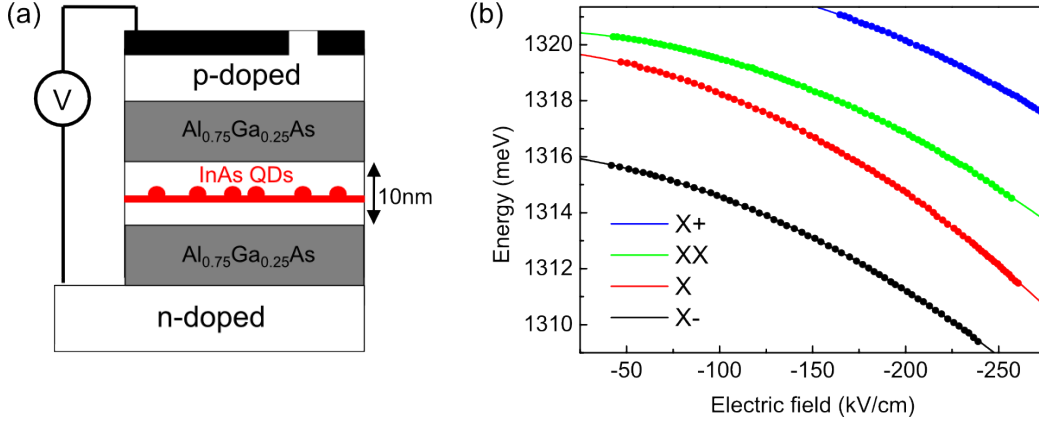
Figure 4.2: (a) Heterostructure design with $Al_{0.75}Ga_{0.25}As$ tunneling barriers preventing carriers from tunneling out of the QD region when a large electric field is applied. (b) Energy of the exciton and biexciton states of our QD as a function of vertical electric field showing a quadratic dependence arising from the quantum-confined Stark effect. Points correspond to experimental data and plain lines are quadratic fits.

	X	XX	X^-	X^+
E_0 (meV)	1319.86	1320.52	1316.16	1322.59
p (μeVkV^{-1}cm)	5.73	1.81	7.11	-4.51
β (μeVkV^{-2}cm^2)	-0.101	-0.083	-0.088	-0.084

Table 4.1: Energy, permanent dipole moment, and polarisability of the four exciton states for our quantum dot (obtained from Fig. 4.2(b)).

states are separated from the X and XX states by 5-10 meV with the X^+ state appearing on the high energy side and the X^- state appearing on the low energy side. All the exciton states shift slightly with electric field due to the quantum confined Stark effect. The field dependence of the shift is given by [90, 91, 92]

$$E = E_0 + pF + \beta F^2, \tag{4.7}$$

where p is the permanent dipole moment in the growth direction, β is the polarisability and F is the applied field. Table 4.1 shows the theoretical fits using Eq. (4.7) to experimental data. The values found are consistent with previous studies on similar structures [93].
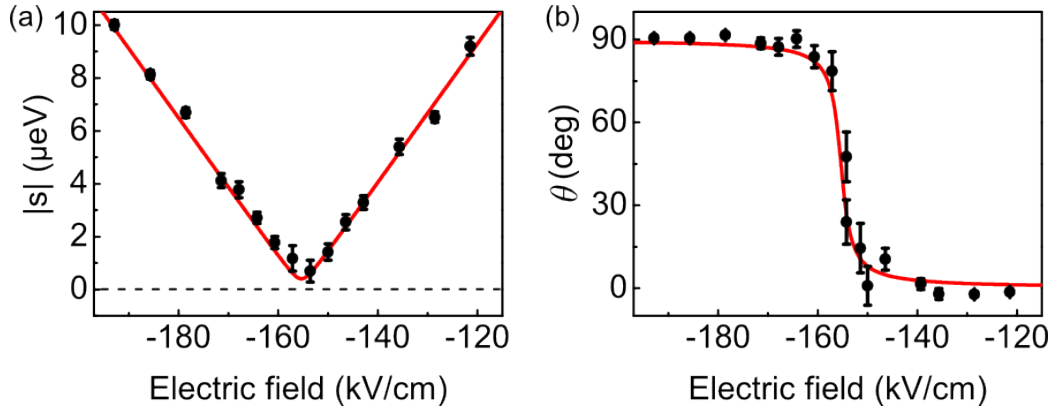
Figure 4.3: (a) Evolution of $|s|$ and (b) orientation of the eigenstates relative to the lab-frame as a function of vertical electric field. Black points correspond to experimental data obtained with our QD and red lines correspond to theoretical fits using Eqs. (4.5) and (4.6).

Measurements of the splitting and orientation of the eigenstates for our QD is shown in Fig. 4.3(a) and (b), along with theoretical fits (plotted in red) to the experimental values using Eqs. (4.5) and (4.6). $|s|$ is found to vary linearly with gradient $\gamma = \pm 0.26 \mu$eVkV^{-1}cm. The anticrossing is measured at a field F_0=-155.4kVcm^{-1} where the splitting is reduced to its minimum value of s_0=0.4μeV.

4.4 Single dots as solid-state photonic interfaces

In this section, we characterise the use of an exciton spin in a single QD as an interface between optical and solid-state qubits. Three steps can be distinguished: the transfer of quantum information from a photon polarisation into the exciton spin state, the spin state time evolution, and the reconversion of a solid-state qubit into a photonic qubit through radiative recombination.

4.4.1 Operating principle of the interface

Fig. 4.4 illustrates the operating principle of a solid-state photonic interface based on a single QD. An input qubit $|\Psi_{in}\rangle$ is first encoded into the polarisation of a photon defined by the parameters θ and φ that are used as coordinates to represent the optical qubit on the Poincaré sphere. Quasi-resonant excitation of the QD then maps the polarisation of $|\Psi_{in}\rangle$ into the spin state of the exciton qubit $|\Psi_X(t)\rangle$, therefore defining a point with the same coordinates (θ, φ) on the Bloch sphere of the solid-state qubit. The phase accumulation between the eigenstates rotates the qubit in a plane parallel to the equatorial plane of the Bloch sphere. Eventually, the electron-hole pair in the QD recombines and emits a photon of polarisation $|\Psi_{out}\rangle$ depending on the time spent in the solid-state $|\Psi_X(t)\rangle$.

4.4.2 Spin initialisation through quasi-resonant excitation

Quasi-resonant optical excitation allows for initialisation of any superposition of spin states by mapping the polarisation of an "input" excitation photon into the spin state of the exciton [94, 85]. This can be achieved through the creation of a phonon, as illustrated in the energy diagram of Fig. 4.5(a). The photoluminescence excitation spectrum obtained for our QD is shown in Fig. 4.5(b). A clear peak is found at an energy of $\approx$34.6meV, indicating optical excitation of the exciton state along with the creation of a 1-LO phonon in GaAs [95]. Resonances at the same energy and of similar width were also found for many other QDs studied.

Considering an input excitation photon of polarisation

$$|\Psi_{in}\rangle = \cos\theta \, |H\rangle + e^{i\varphi} \sin\theta \, |V\rangle \,, \tag{4.8}$$

the idealised coherent time evolution of the exciton spin state (away from the anticrossing) is given by

$$|\Psi_X(t)\rangle = \cos\theta \, |X_H\rangle + e^{i\frac{st}{\hbar}} e^{i\varphi} \sin\theta \, |X_V\rangle \,. \tag{4.9}$$
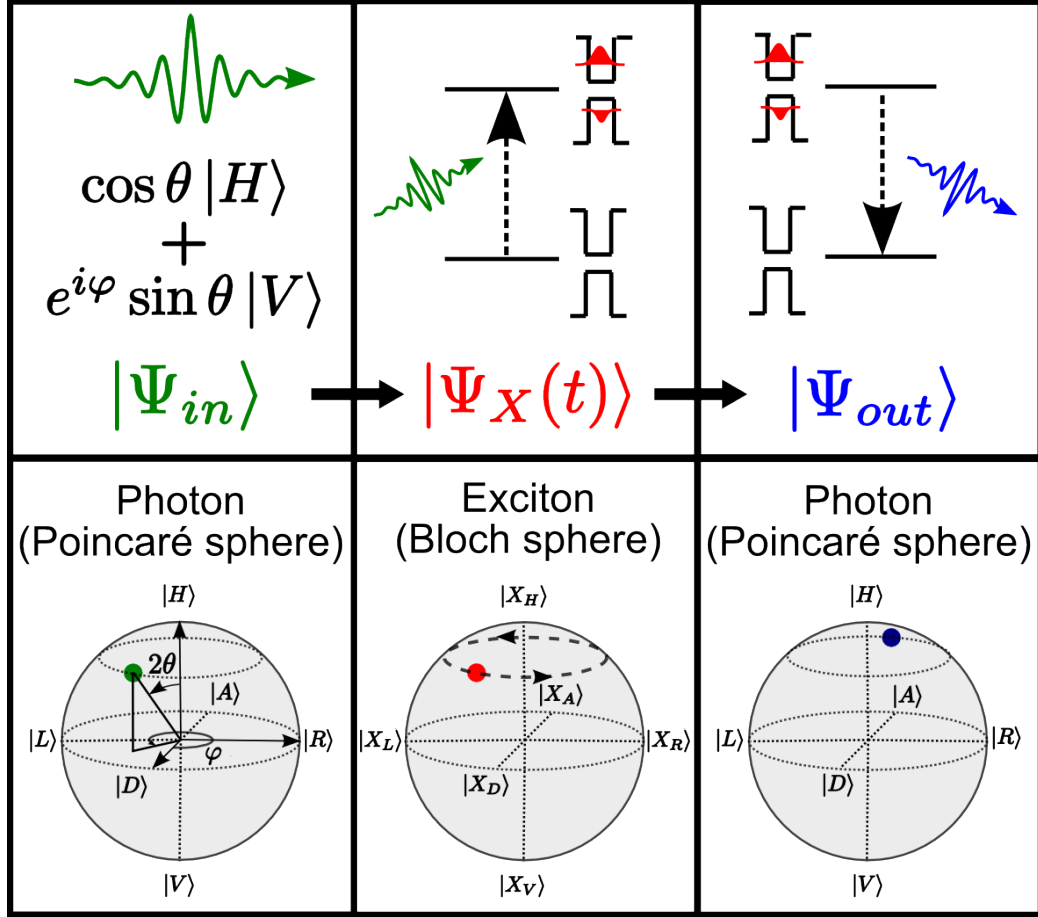
Figure 4.4: Operating principle of our solid-state photonic interface. An optical qubit $|\Psi_{in}\rangle$ is first encoded in the polarisation of a photon. Quantum information is then coherently transferred from $|\Psi_{in}\rangle$ into the spin state $|\Psi_X(t)\rangle$ of the exciton which rotates around the equatorial plane of the Bloch sphere at an angular velocity $|s|/\hbar$. Finally, the electron-hole pair recombines and emits a photon of polarisation $|\Psi_{out}\rangle$ depending on the time spent in the solid-state.

The splitting s therefore introduces a phase difference between the eigenstates accumulated over time at a rate of $st/\hbar$ and leading to coherent oscillations of the spin state [96]. Those oscillations can be observed by initialising an exciton in a superposition of eigenstates and measuring its radiative emission along any superposition of eigenstates (Fig. 4.6(a)), leading to a signal of intensity
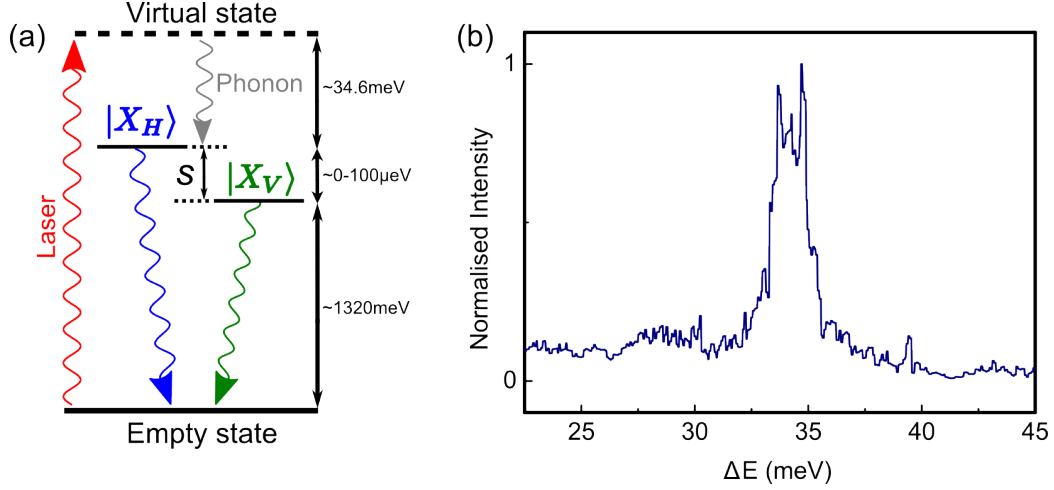
Figure 4.5: (a) Schematic energy diagram of the QD used in our experiment where the polarisation of the laser is transferred into the exciton spin state through quasi-resonant excitation. As indicated, the schematic is not to scale: 1-LO phonons in GaAs have an energy around 34.6meV while s is in the 0-100μeV energy range and the neutral exciton energy is around 1320meV for our QDs. (b) PLE spectrum for our QD showing the resonance corresponding to excitation through the creation of a 1-LO in GaAs.

$$I(t) \propto \cos\left(st/\hbar\right) e^{-t/\tau_r}, \tag{4.10}$$

where τ_r is the radiative lifetime measured to be 1.28$\pm$0.08ns for our QD. Fitting those oscillations allows for temporal measurements of $|s|$ that agree well with spectral measurements (Fig. 4.6(b)).

4.4.3 Time evolution of the spin state

We measure the evolution of the exciton spin state by time-resolving the polarisation state of the photons that are emitted. The polarisation state of a photon can be measured using the density matrix formalism. The general form of the density matrix for a qubit is

$$\rho = |\Psi\rangle \langle\Psi| = \begin{pmatrix} \rho_{11} & \rho_{12} \\ \rho_{12}^* & \rho_{22} \end{pmatrix}, \tag{4.11}$$
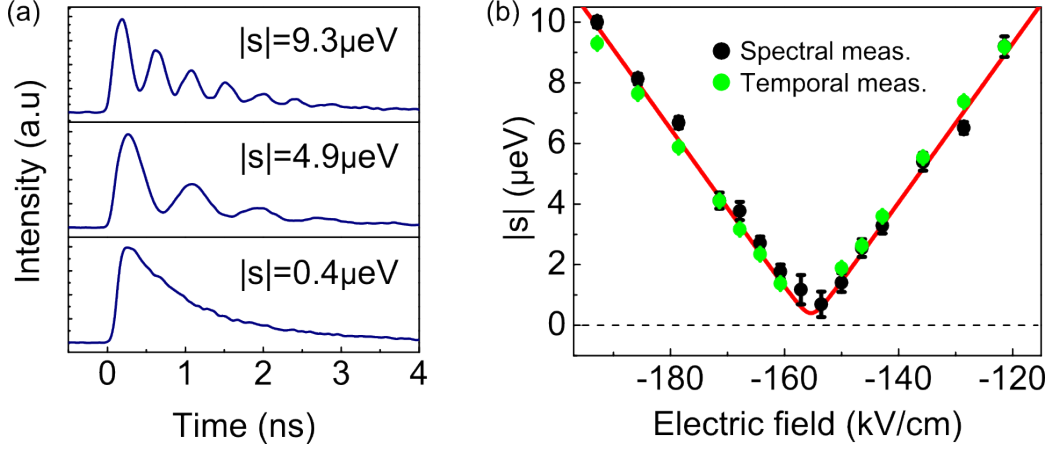
Figure 4.6: (a) High-visibility coherent oscillations of the spin state for three different values of $|s|$. The exciton was initialised in a maximum superposition of eigenstates and emission was time-resolved along the same orientation. (b) Comparison between spectral and temporal measurements of $|s|$.

where $\rho_{11} + \rho_{22} = 1$ and $*$ denotes the complex conjugate. Using the $\{|H\rangle, |V\rangle\}$ basis where

$$|H\rangle = \begin{pmatrix} 1 \\ 0 \end{pmatrix} \; ; \; \{V\rangle = \begin{pmatrix} 0 \\ 1 \end{pmatrix}, \tag{4.12}$$

and considering a qubit $|\Psi\rangle = \cos\theta\,|H\rangle + e^{i\frac{st}{\hbar}}e^{i\varphi}\sin\theta\,|V\rangle$, we find

$$\rho = \begin{pmatrix} \cos^2\theta & \cos\theta\sin\theta e^{-i\frac{st}{\hbar}}e^{-i\varphi} \\ \cos\theta\sin\theta e^{i\frac{st}{\hbar}}e^{i\varphi} & \sin^2\theta \end{pmatrix}. \tag{4.13}$$

The density matrix of a photon can be reconstructed by measuring its polarisation in the linear, diagonal, and circular bases according to

$$\rho_{11} = \langle H\,|\rho|\,H\rangle = \cos^2\theta, \tag{4.14}$$

$$Re\,(\rho_{12}) = \langle D\,|\rho|\,D\rangle - \frac{1}{2} = \cos\theta\sin\theta\cos(\varphi + \frac{st}{\hbar}), \tag{4.15}$$

$$Im\,(\rho_{12}) = \langle L\,|\rho|\,L\rangle - \frac{1}{2} = \cos\theta\sin\theta\sin(\varphi + \frac{st}{\hbar}). \tag{4.16}$$

In theory, only one measurement in each basis (i.e. a set of three mea-

surements) is therefore required to reconstruct the density matrix considering the normalisation conditions. However, those normalisation conditions must be experimentally obtained by measuring both polarisations for each basis. As a consequence, a total of six measurements are needed in order to study the time evolution of the exciton spin state.

In Fig. 4.7, the exciton was initialised in a diagonal superposition of eigenstates (corresponding to $|X_D\rangle$ on the Bloch sphere) and the emission was measured in the linear $\{|H\rangle, |V\rangle\}$, diagonal $\{|D\rangle, |A\rangle\}$ and circular $\{|R\rangle, |L\rangle\}$ bases. Measurements were performed at an electric field of -175kVcm^{-1} where $|s| \approx$ 5μeV and where the eigenstates are oriented along H and V. Each signal was normalised by the sum of the two measurements in the corresponding basis. The time evolution for each measurement is given by

$$\langle H \, |\rho| \, H \rangle = \frac{1}{2}, \tag{4.17}$$

$$\langle V \, |\rho| \, V \rangle = \frac{1}{2}, \tag{4.18}$$

$$\langle D \, |\rho| \, D \rangle = \frac{1}{2} + \frac{1}{2}\cos(\frac{st}{\hbar}), \tag{4.19}$$

$$\langle A \, |\rho| \, A \rangle = \frac{1}{2} - \frac{1}{2}\cos(\frac{st}{\hbar}), \tag{4.20}$$

$$\langle R \, |\rho| \, R \rangle = \frac{1}{2} - \frac{1}{2}\sin(\frac{st}{\hbar}), \tag{4.21}$$

$$\langle L \, |\rho| \, L \rangle = \frac{1}{2} + \frac{1}{2}\sin(\frac{st}{\hbar}), \tag{4.22}$$

where $\rho = |D\rangle \langle D|$ is the density matrix of a diagonally-polarised photon. No oscillations are observed when measuring $|\Psi_{out}\rangle$ along the eigenstates while oscillations of angular frequency $s/\hbar$ are observed when measuring in diagonal and circular basis states, with a dephasing corresponding to the respective positions of those states on the equator of the Bloch sphere.

After normalisation, one measurement from each basis can be used to reconstruct the exciton spin state density matrix using Eqs. (4.14)-(4.16) (Fig. 4.8(a)). Moreover, the qubit position on the Bloch sphere can also be calculated using the Bloch vector. with coordinates $(\sin 2\theta \cos \varphi, \sin 2\theta \sin \varphi, \cos 2\theta)$.
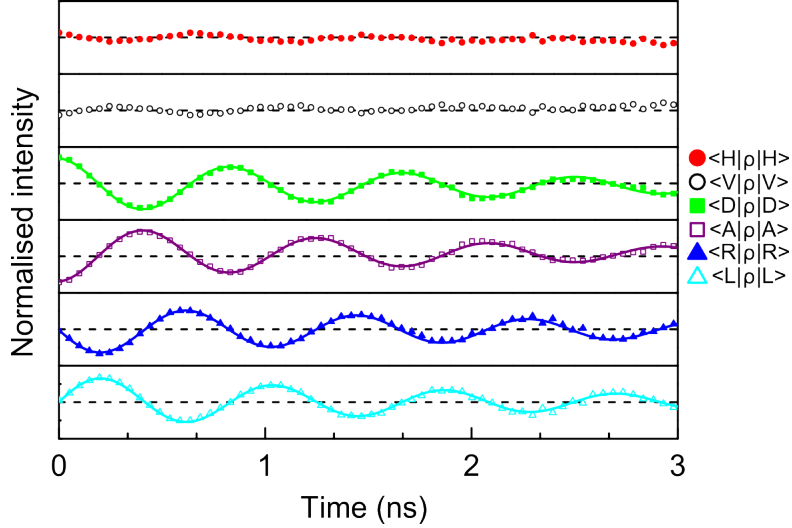
Figure 4.7: Complete characterisation of the time evolution of $|\Psi_X(t)\rangle$ prepared in the $|X_D\rangle$ spin state by time-resolved measurements in linear, diagonal, and circular bases. The symbols refer to measurements along different polarisations. The vertical scale for each signal goes from 0 to 1.

The free evolution of the exciton spin Bloch vector around the Bloch sphere in the equatorial plane is shown in Fig. 4.8(b) along with the projected trajectories. The norm of the Bloch vector is smaller than 1 due to imperfect initialisation of the spin state and it decreases with time due to decoherence effects, as discussed in the next section.

4.4.4 Fidelity of the interface

The fidelity of the interface is defined as

$$f_{in} = |\langle\Psi_{out}|\Psi_{in}\rangle|^2 = \frac{I_{co}}{I_{co} + I_{cross}}, \tag{4.23}$$

where I_{co} (I_{cross}) is the output photoluminescence intensity co(cross)-polarised with the excitation polarisation. We measured the fidelity at -175kVcm^{-1} for six different input qubits prepared in the linear, diagonal, and circular states (Fig. 4.9). Exciting an eigenstate leads to f_{in}=0.95±0.03 decaying with a time scale of 78±17ns, which is limited by spin scattering. Exciting a maximum superposition leads to an initial fidelity f_{in}=0.81±0.03
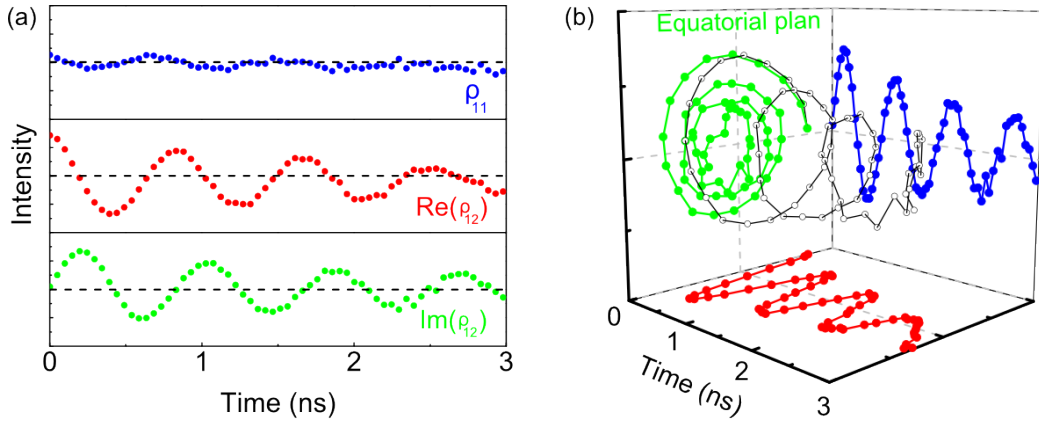
Figure 4.8: (a) Intensity of the normalised density matrix elements as a function of time. The scale for ρ_{11} goes from 0 to 1, while the scale for $Re(\rho_{12})$ and $Im(\rho_{12})$ goes from -0.5 to 0.5. (b) Trajectory of the Bloch vector (in black) around the Bloch sphere, which illustrates the qubit rotation in the equatorial plane due to the finite splitting between the eigenstates. Green, blue and red solid lines show the projected trajectories (axes scale from 0 to 1).

which oscillates due to the finite value of s. The envelope of the time-resolved fidelity decays with a time scale of 3.0±0.4ns limited by cross-dephasing, which randomises the phase relationship between the two super-imposed eigenstates [97, 96]. Cross-dephasing is significantly longer than the radiative lifetime and the time needed to perform electrical manipulation of the qubit.

The amplitude of the oscillation in the fidelity for maximum superpositions is reduced compared to the fidelity when exciting in an eigenstate. We mostly attribute this to the finite response time of the APD (timing resolution of ≈50ps), the temporal resolution of the SPCM card (≈10ps), the width of the laser pulse (≈2-100ps), and the uncertainty in the time at which the superposition is created and detected originating from the finite linewidth of the transition. Moreover, slight misalignment of the wave plates and their miscalibration at the excitation energy also may also cause some fidelity reduction in the case of a maximum superposition.

The combined effect of the APD, the SPCM card and the laser pulse width is measured in Fig. 4.10(a) by directly time-resolving the laser emission. We
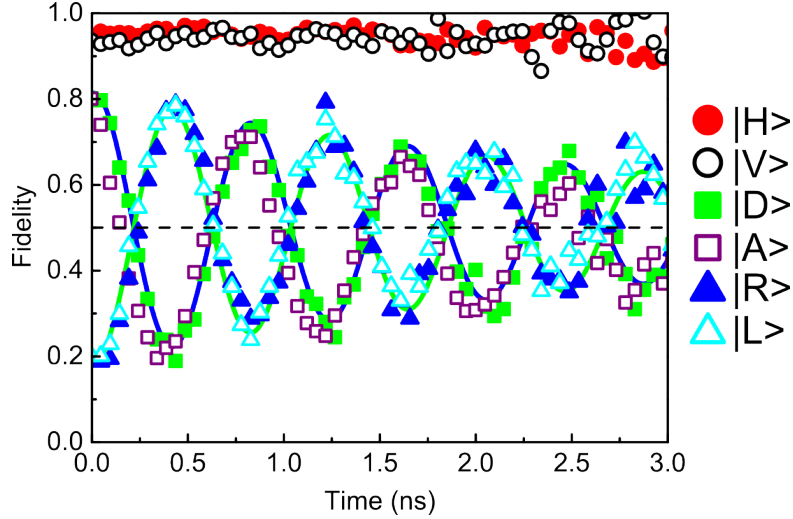
Figure 4.9: Fidelity $f_{in}=|\langle\Psi_{out}|\Psi_{in}\rangle|^2$ of the interface. The symbols refer to different input qubits.

approximate the response function with a normalised Gaussian function and we define the temporal jitter of the system as the full-width at half-maximum (FWHM) measured to be 100 ± 1ps. The effect of the jitter width on the fidelity of the interface for a maximum superposition is illustrated in Fig. 4.10(b) for different values of the fine structure splitting, assuming an initial fidelity of 0.95. The data were obtained by measuring the amplitude of the signal resulting from the convolution of a sine function of amplitude 0.95 with a normalised Gaussian function of variable FWHM. As an important part of the total jitter width is due to technological limitations and considering that the performance of available detectors is continuously improving, we anticipate that a higher initialisation fidelity for maximum superpositions should be achievable in the near term.

4.5 Electrical coherent spin manipulation

In this section, the change in splitting s and the coherent coupling between the exciton states when a vertical electric field is applied are used to implement logic gates and manipulate the exciton spin on a subnanosecond time
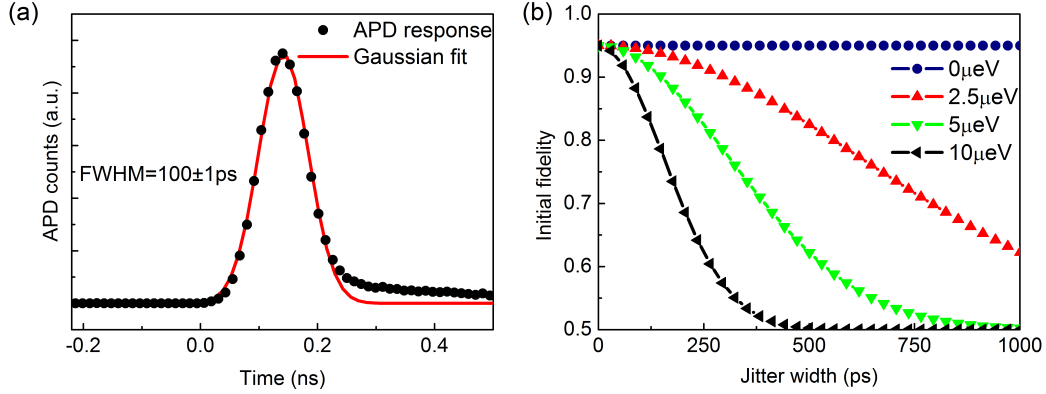
Figure 4.10: (a) Response function of the APD when illuminated with a mode-locked pulsed laser along with a Gaussian fit of which the FWHM gives the jitter. (b) Effect of the jitter width on the measured initial fidelity of a maximum superposition for different values of the splitting.

scale.

4.5.1 Gate fidelity

The fidelity f_G of a gate operation is given by [98]

$$f_G = |\langle \Psi_G | U_I | \Psi_{in} \rangle|^2 / f_{in}, \tag{4.24}$$

where Ψ_G is the state of the photon emitted by the exciton after the gate operation and U_I is the ideal gate transformation matrix. Normalisation to f_{in} is used to evaluate the fidelity of the gate independently of the initialisation of the spin state discussed previously. To take dephasing into account, the definition can be extended to [99]

$$f_G = Tr\left[\rho_G U_I \rho_X U_I^*\right] / Tr\left[\rho_X^2\right], \tag{4.25}$$

where $\rho_G = |\Psi_G\rangle \langle \Psi_G|$ is the density matrix of the photon emitted by the exciton after the gate operation, $\rho_X = |\Psi_X\rangle \langle \Psi_X|$ is the density matrix of the exciton state with no gate applied, and Tr represents the trace.

4.5.2   Phase-shift gate

A phase-shift gate is a single-qubit gate that leaves the basis state $|X_H\rangle$ unchanged and maps $|X_V\rangle$ to $e^{i\xi}|X_V\rangle$, where ξ is the phase-shift. This operation is equivalent to rotating the qubit in the equatorial plane of the Bloch Sphere by ξ radians. The gate operation is represented by the "rotation" matrix

$$R_\xi = \begin{bmatrix} 1 & 0 \\ 0 & e^{i\xi} \end{bmatrix}. \tag{4.26}$$

Electrical coherent control of the phase accumulated by the qubit when initialised in a superposition of eigenstates can be demonstrated by dynamic modulation of $|s|$. We operate at values $|s| > 5\mu\text{eV}$ so that the orientation of the eigenstates does not change significantly with electric field. The time evolution is then given by

$$|\Psi_X(t)\rangle = \cos\theta\,|X_H\rangle + e^{i\frac{\int_0^t s(\tau)d\tau}{\hbar}}e^{i\varphi}\sin\theta\,|X_V\rangle, \tag{4.27}$$

where $s(\tau)$ is modulated by an electrical pulse inducing faster phase accumulation during the gate operation (Fig. 4.11(a)). By applying a pulse of constant width but different amplitudes, we show that the phase-shift is proportional to the gate amplitude (Fig. 4.11(b)). Some deviation from linear behaviour arises from ringing in the electrical signal due to limited speed of our device and limited bandwidth of the pulse generator.

Phase-shifts were fitted from time-resolved measurements shown in Fig. 4.12 where the exciton was initialised in a diagonal superposition $|X_D\rangle$ and emission was measured both along the diagonal and anti-diagonal polarisations. A 500ps Gaussian electrical pulse was applied 250ps after the laser initialises the qubit.

Further measurements to assess the quality of the gate operation were performed for a phase-shift $\xi = \pi$ (corresponding to what is known as the Pauli-Z gate). Fig. 4.13(a) and (b) show measurements in the diagonal basis after initialisation in $|X_D\rangle$, respectively without gate and with a π phase-shift gate applied, the latter corresponding to a modulation of $|s|$ from a minimum
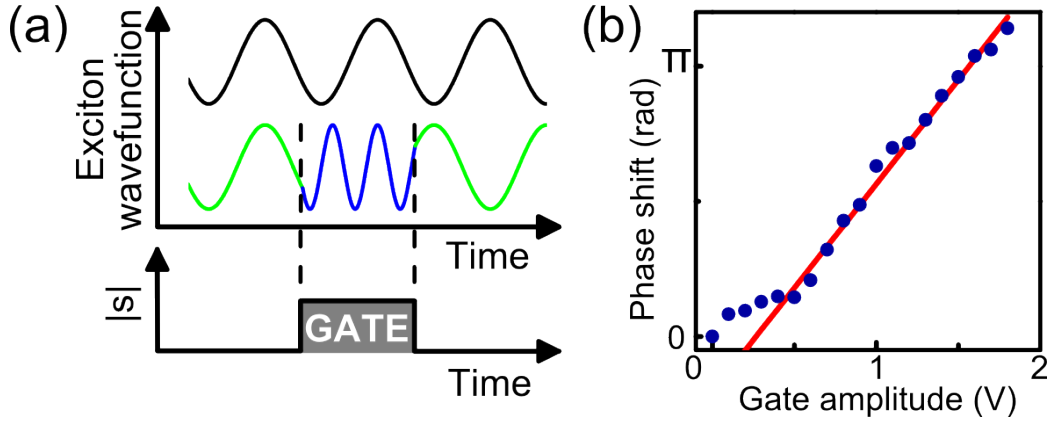
Figure 4.11: (a) The electrical gate modulates $|s|$ and induces a faster phase accumulation between the spin eigenstates. The gated time-evolution (bottom) is consequently dephased compared to the ungated operation (top). (b) Phase-shift as a function of gate amplitude.
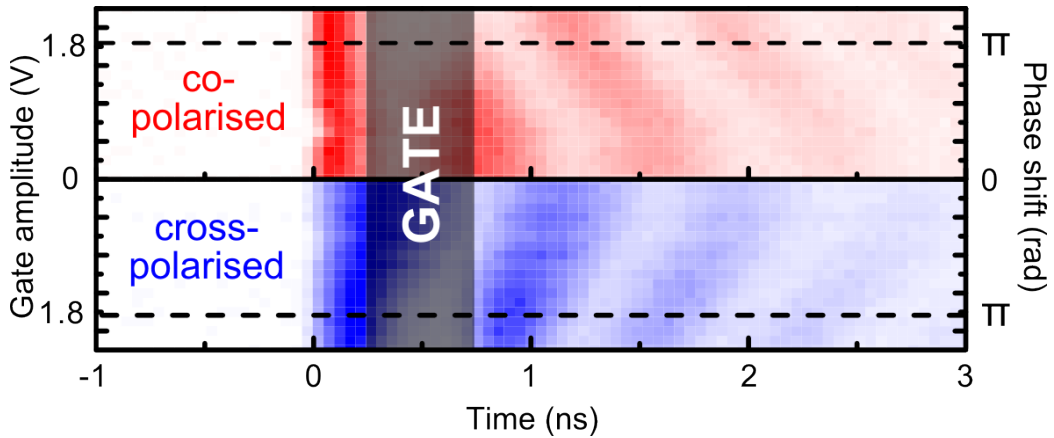
Figure 4.12: Normalised (color scale from 0 to 1) time-resolved data for an exciton initialised in a diagonal superposition $|X_D\rangle$ and measurements in the diagonal basis.

of $\approx 5\mu$eV to a maximum of $\approx 10\mu$eV, estimated from the Stark shift resulting from the electrical pulse. The intensity falls during the gate operation as emission is Stark-shifted out of the detection window. Fidelity as a function of time for the phase-shift gate is shown in Fig. 4.13(c). Irregularities in the evolution of the fidelity just after the gate are due to ringing in the electrical signal. Away from the gate, the fidelity fluctuates between 0.9 and 1.
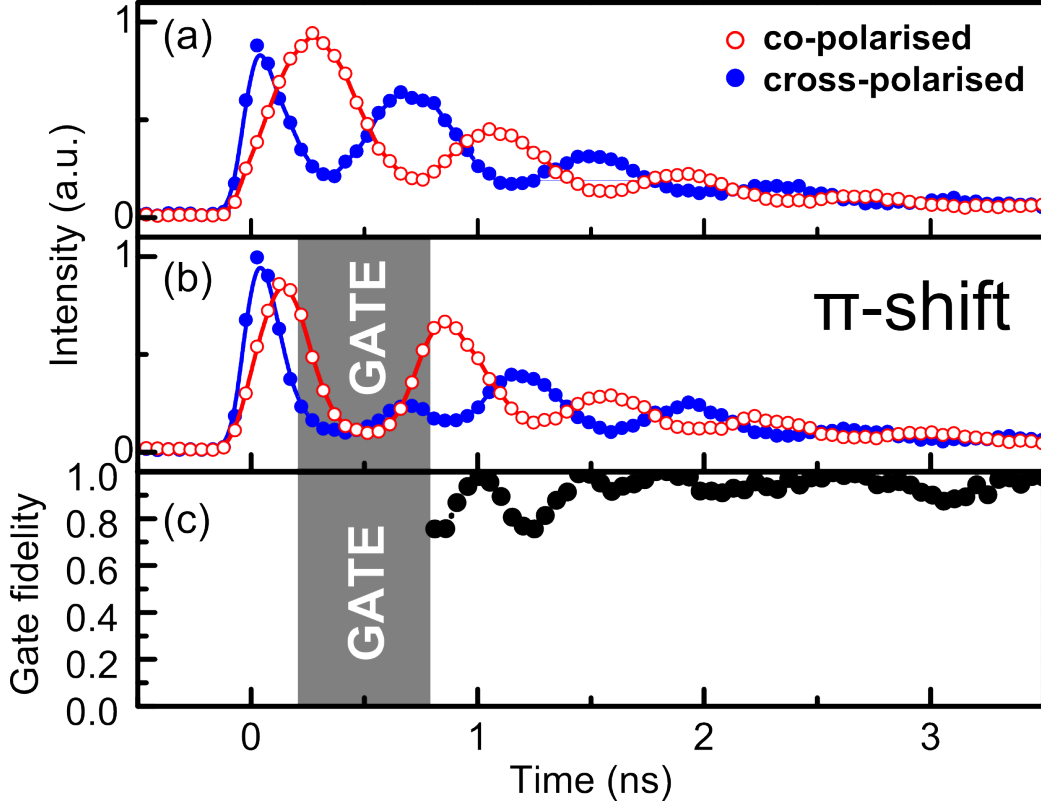
Figure 4.13: (a) and (b) Radiative emission from the QD initialised in $|X_D\rangle$ respectively without gate and with a π phase-shift gate. (c) Fidelity of the π-shift gate operation as a function of time.

4.5.3 Spin-flip gate

More complex operations are achieved by operating at small values of $|s|$ where the orientation of the eigenstates are strongly sensitive to the electric field (Fig. 1(c)). This ability to change not only the energetic splitting of the two levels but also to dynamically vary the eigenstates allows complete control of the qubit: any input state can be mapped onto any output state.

To illustrate this we now describe a "spin flip" between the two eigenstates obtained by applying a spin-flip gate (also known as the Pauli-X gate), which is the quantum equivalent of a NOT gate. This gate is represented by the Pauli-X matrix

$$X = \begin{bmatrix} 0 & 1 \\ 1 & 0 \end{bmatrix}. \tag{4.28}$$

The operating principle behind implementing the spin-flip gate with a QD is shown in Fig. 4.14. The exciton is initialised in the eigenstate $|X_D\rangle$ at minimum splitting $|s|$=0.4μeV and is represented by a point at the north pole of the Bloch sphere with the axis labeled D. An electrical pulse similar to that used to obtain the π phase-shift is applied to the structure and rotates the eigenstates by 45° (the new eigenstates being therefore $|X_H\rangle$ and $|X_V\rangle$) without changing the orientation of the spin state. As a consequence, the exciton is now in a superposition $|X_D\rangle$ represented at the equator of the Bloch sphere and still oriented diagonally in the lab-frame. A π phase is then accumulated during the gate operation leading to the superposition $|X_A\rangle$. After the pulse, the eigenstates rotate back to their initial pre-pulse orientation with the exciton being now in its eigenstate $|X_A\rangle$, corresponding to a spin flip from $|X_D\rangle$.

Fig. 4.15(a) and (b) show emission from both eigenstates (oriented along D and A), after exciting $|X_D\rangle$. The polarisation of the emission after the gate is reversed, corresponding to a spin-flip in the solid-state. Fig. 4.15(c) shows the fidelity as a function of time obtained for the spin-flip operation shown in Fig. 4.15(b). The fidelity is 0.97 after the gate and then fluctuates due to ringing in the electrical signal.

4.6   Conclusion

In conclusion, we demonstrated that an exciton in a QD is a high-fidelity solid-state photonic interface, on which arbitrary phase-shifts and spin-flips can be performed electrically. Quantum information encoded in the polarisation of a photon was transferred into and restored from the spin state of the exciton. Coherent manipulation of the spin qubits was achieved through dynamical modulation of a vertical electric field and high-fidelity phase-shift and spin-flip gate operations were demonstrated.

Using small gate areas and on-chip electronics will reduce ringing in the
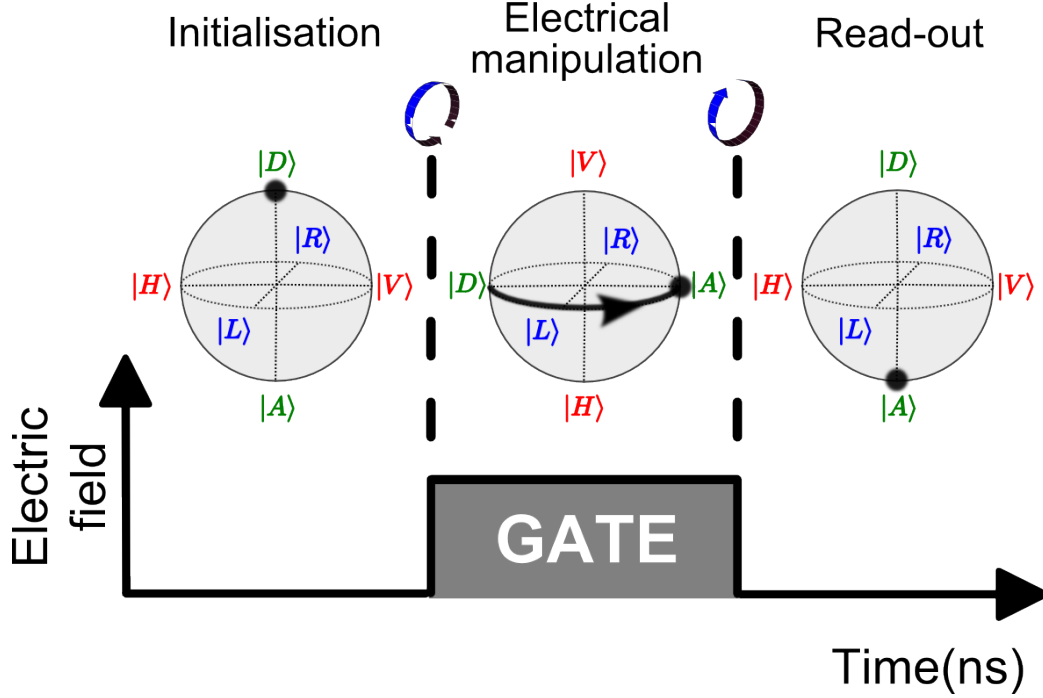
Figure 4.14: Operating principle of the spin-flip gate. The exciton is initialised at minimum splitting in its eigenstate $|X_D\rangle$. Modulating the electric field changes the value of $|s|$ and rotates the eigenstates by 45° resulting in a superposition $|X_D\rangle$. A π phase-shift is accumulated during the gate operation leading to a superposition $|X_A\rangle$. Returning to the initial value of the electric field induces another 45° rotation of the eigenstates resulting in a spin flip.

electrical signals and improve the gate fidelities. It will also allow operation times below 10ps [100], so that more than 300 operations can be performed within the coherence time. Extending our scheme to two qubits could be achieved in the near term through the creation of biexcitons [99]. Further increase in the number of qubits would be achievable using site-positioned dots with low fine-structure splitting in devices with local gates, which is technologically feasible [101].

The main limitation of a solid-state photonic interface based on single QDs is the short radiative lifetime of excitons, limiting storage to few nanoseconds. Reducing the local optical density of states with cavity QED [71] or using quantum dot molecules to separate the electron-hole pair and
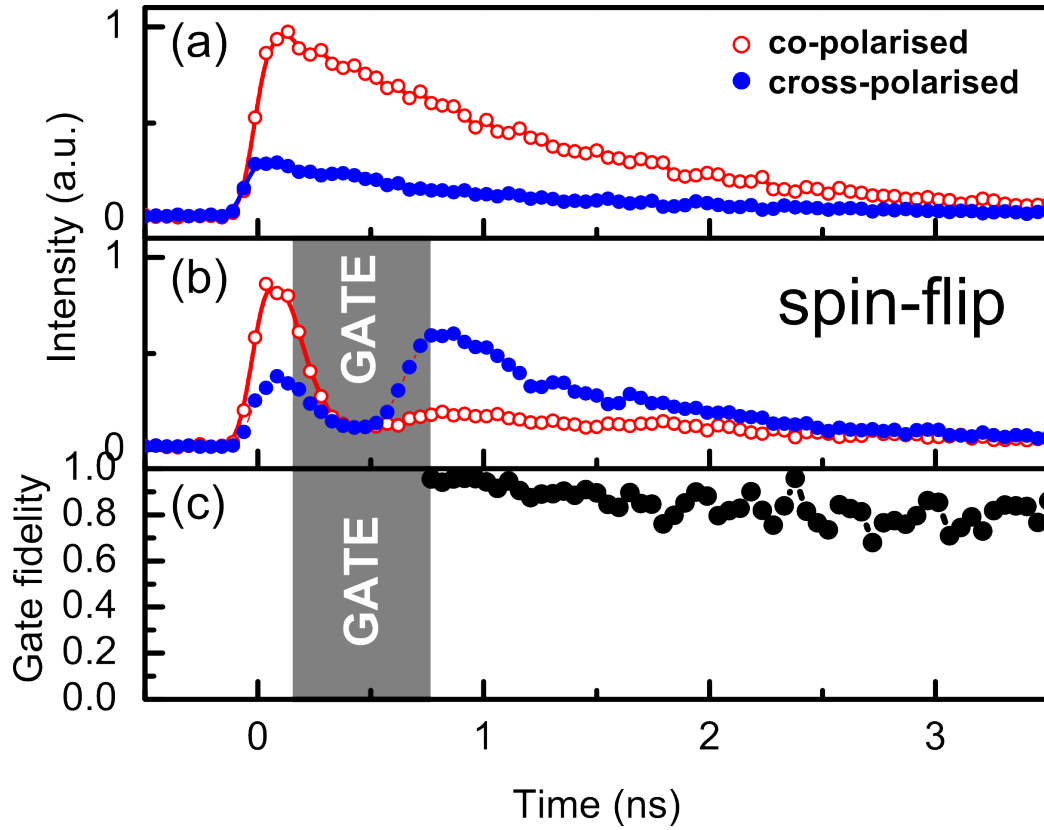
Figure 4.15: (a) and (b) Radiative emission from the QD respectively without gate and with the spin-flip gate. The trace with empty (plain) circles is obtained when exciting and measuring along the same (opposite) eigenstates. (c) Fidelity of the spin-flip gate as a function of time.

prevent recombination [102] could however increase the exciton lifetime by orders of magnitude and allow for triggered emission. We decided to explore the latter solution and our results on quantum dot molecules are presented in the next two chapters.

Chapter 5

Quantum dot molecules in electrically-tunable structures

5.1 Introduction

The functionality of single QDs can be enhanced by combining them into quantum dot molecules (QDMs) where the coupling of the QDs is controlled with an external electric field. Vertically-stacked QDs forming QDMs [59, 103] have recently attracted much attention, which has lead to a better understanding of their physical properties such as coherent delocalisaltion of excitonic states under electric fields [104, 105] and tunable exchange interactions [106]. New applications based on those properties include electrostatic spin manipulation [107, 108], single-shot measurement of an electron spin [109], ultrafast optical control of entanglement between two quantum-dot spins [110], and exciton-spin storage devices [102].

However, most of the research on electric-field dependent spectroscopy of QDMs has so far focused on only one type of charged states (positive or negative) per device [106, 111]. Moreover, the limited range of accessible electric fields in the structures used prevented the observation of intradot transitions properties such as the quantum confined Stark effect (QCSE). Finally, controllable tunneling of carriers between the QDs forming a QDM was studied only for InAs QDs capped with GaAs and annealed at higher

temperature [112]. Further study of QDMs under electric fields therefore promises to extend their potential as a resource for quantum information processing.

In this chapter, we present a comprehensive study of InAs QDMs in *p-i-n* and *n-i-p* diode structures. Selective coupling of electron and hole energy levels of the QDM was achieved by modifying the doping profile of the diode structure. Neutral exciton coupling energies for both carriers were measured as a function of barrier thickness between the QDs. Moreover, we performed an electric-field dependent spectroscopic analysis of the four main transitions: the neutral exciton and biexciton (X and XX), the positively charged exciton (X^+), and the negatively charged exciton (X^-). The 20 optically-allowed transitions (compared to 4 optically-allowed transitions for single QDs) were accessible using a single device and the QCSE from intradot transitions was measured. Experimental results were compared to theoretical models. Finally, the effects of an electric field on the electron-hole exchange interaction that defines the fine structure splitting and polarisation anisotropy of the bright neutral exciton states are investigated in QDMs.

5.2 Background

5.2.1 Device structure

The devices used in our study consist of *p-i-n* and *n-i-p* heterostructures grown by molecular beam epitaxy (Fig. 5.1(a)). Two layers of InAs QDs with dot density $<1\mu\text{m}^{-2}$ and separated by a GaAs barrier of controllable layer thickness d were grown at the center of the intrinsic region made of a GaAs quantum well clad with a short period superlattice equivalent to $Al_{0.75}Ga_{0.25}As$ on each side, which prevents tunneling of the carriers out of the QD region when a large vertical electric field is applied. Vertical alignment of the QDs to form QDMs naturally arises from the strain field generated by the growth of the first layer [61, 62]. Doping extends into the superlattice and allows for application of an electric field along the growth direction. The electric field F is calculated using $F = \left(\frac{V - V_{bi}}{D}\right)$, where V is the bias applied
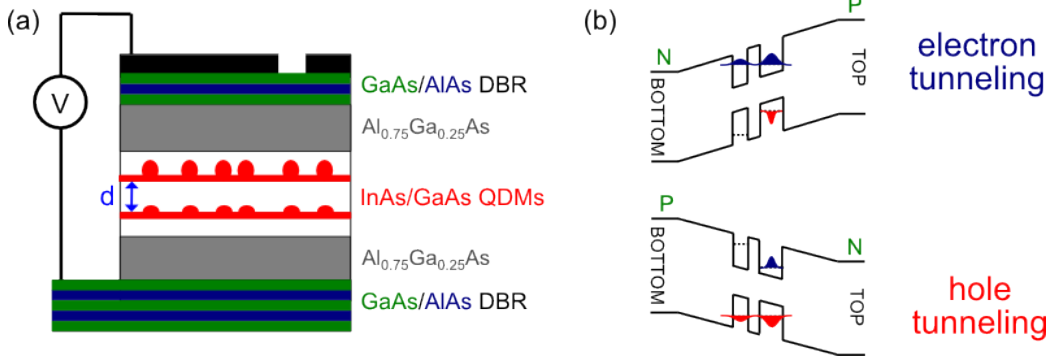
Figure 5.1: (a) Schematic illustration of the device structure. (b) Selective tunneling of carriers in a QDM using different doping configuration. Electron (hole) wavefunctions are represented in blue (red).

to the structure, V_{bi} is the built-in potential and D is the thickness of the intrinsic region. The devices were encased in weak planar microcavities to enhance collection efficiency. An aluminium mask on top of the sample with μm-sized apertures was used to isolate a small number of QDMs for optical measurements.

5.2.2 Structural and energetic properties

QDs from the top layer are strain-induced and therefore larger than QDs from the bottom layer [63, 64]. As a consequence, the energy levels for the electron (resp. hole) are lower (resp. higher) in the top QD and carriers relax into the top QD at flat-band conditions (low-energy configuration). Applying a vertical electric field in reverse bias (to avoid electrical injection of carriers) will increase (resp. decrease) the energy of the levels on the p-side (resp. n-side) of the diode structure. Consequently, tuning the electron (resp. hole) energy levels from the top QD into resonance with the levels of the bottom QD requires the top QD to be positioned on the p-side (resp. n-side) of the structure. Selective coupling of electron or hole energy levels of the QDM is therefore possible by modifying the doping profile, with p-i-n (resp. n-i-p) doping sequence (from bottom to top) leading to hole (resp. electron) energy levels coupling (see Fig. 5.1(b)).

Tuning the energy levels of both QDs into resonance results in coherent tunneling of the carriers between the QDs, leading to the formation of molecular orbitals delocalised over both QDs and the intervening barriers. Such tunneling events give rise to anticrossings (see Fig. 5.2(a) for a neutral exciton anticrossing arising from the tunneling of a hole from the top to the bottom QD) and the formation of complex patterns, which depend on the nature of the state and the properties of the QDs in the QDM. The patterns from the four main transitions (X,XX,X$^+$,X$^-$) will be studied in section 5.4. On the anticrossing shown in Fig. 5.2(a), two electric field dependences are distinguished. In the so-called "direct" states (i.e. both carriers involved in the optical transitions are confined into the same QD, see orange dashed line in Fig. 5.2(a)), a rather weak dependence is found due to the small dipole moment in the direction of the field and as a first approximation the field dependence of the direct states is neglected. For the "indirect" states (i.e. carriers involved in the optical transition are located in different QDs, see green dashed line in Fig. 5.2(a)), the dipole moment in the direction of the field is substantially larger due to the large separation of the electron and hole when confined in separate QDs. The magnitude of the dipole moment of the indirect exciton is ed (where e is the electron charge and d is the separation between the electron and the hole, i.e. essentially the thickness of the barrier between the QDs) and its orientation is from the electron to the hole (see Fig. 5.2(b)). In the case of hole (electron) tunneling, the electric field F is along (opposite) the growth direction so that the electric field dependence of the energy of indirect states is $-edF$ (edF).

5.3   Selective tunneling of carriers

As described in section 5.2.2, modifying the doping profile allows for controlling the tunneling carrier. Both types of tunneling can generally not be studied on the same device. We define a positive electric field as an electric field along the growth direction so that electron (resp. hole) energy levels coupling usually occurs at negative (resp. positive) fields (see Fig. 5.3). In some few cases, hole tunneling events were also observed at negative electric
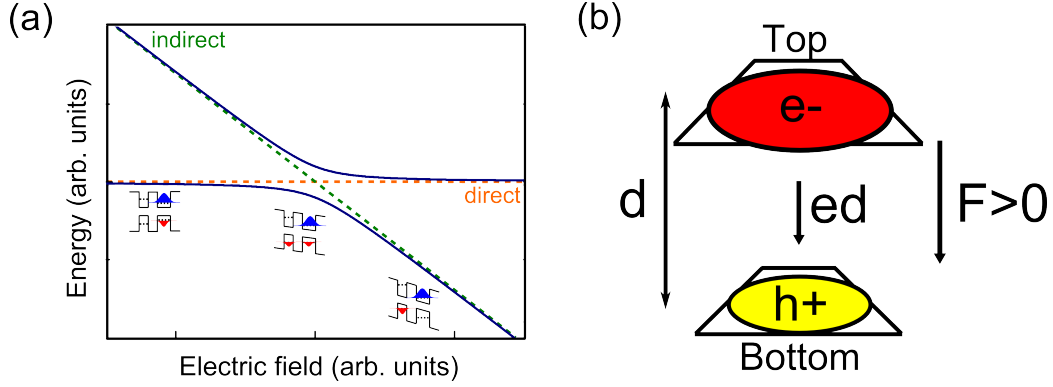
Figure 5.2: (a) Electric field dependence of the direct and indirect exciton states and coherent coupling of the hole energy levels of both QDs resulting in the formation of an anticrossing. Schematic band diagrams of the exciton at different electric fields are shown. (b) Schematic illustration of the QDM exciton at positive electric field when the hole has tunnelled from the top QD to the bottom QD. The dipole moment of the indirect exciton, *ed*, is indicated.

fields (such as for the QDM presented in section 5.4.8), which we attribute to fluctuations in the size of QDs [63, 64] that causes some departure from the simplified picture in Fig 5.3. However, no difference in any properties measured and discussed in this chapter were observed between QDMs with hole tunneling events at positive and negative electric fields.

A typical example of tunneling event giving rise to an anticrossing is shown in Fig. 5.4 respectively for (a) electron and (b) hole tunneling. Fig. 5.4 was generated using standard micro-PL spectroscopy (see section 3.2.1). Individual spectra were accumulated at different values of the electric field applied to the structure to generate a three-dimensional plot usually referred to as a "spectral map" [105, 106]. Spectral maps for electron and hole tunneling shown in Fig. 5.4 corresponds to the same quantum state (the neutral exciton) of a QDM and the same distance between the QDs, which clearly illustrates the dependence of the anticrossing size on the nature of the tunneling carrier.

Using selective doping, we measured neutral exciton anticrossing energies for electron and hole tunneling as a function of GaAs barrier layer thickness on more than 50 QDMs. Results obtained are plotted in Fig. 5.5(a), where
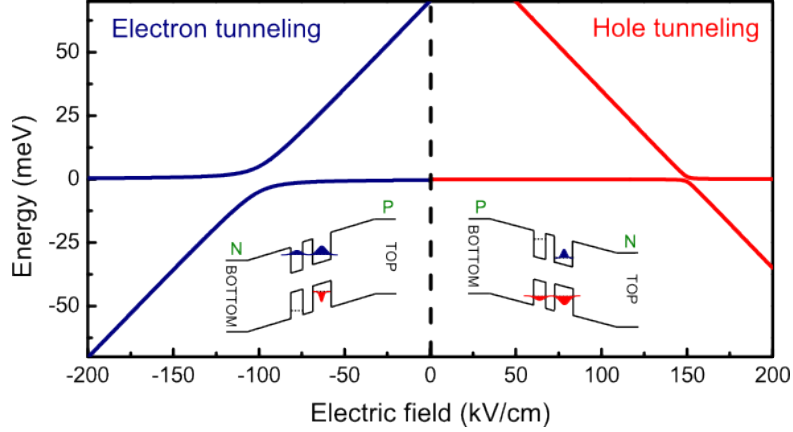
Figure 5.3: Electron and hole tunneling occurring respectively at negative and positive electric fields. The electric field at which an anticrossing appears depends on the physical properties of each QDM and is expected to be different for hole and electron tunneling as shown in this schematic illustration.
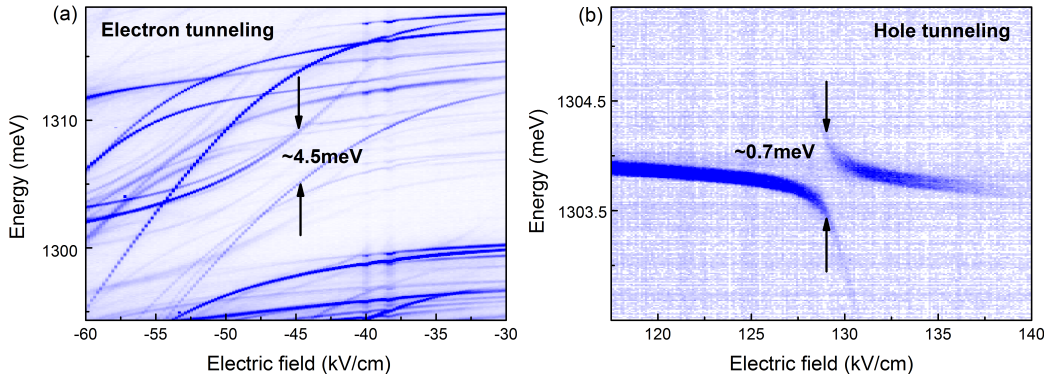
Figure 5.4: Anticrossings of different sizes arising from the tunneling of (a) an electron hole and (b) a hole in QDMs with similar barrier thickness. Holes are expected to have lower tunnel coupling energy than electrons due to their higher effective mass. In both plots, the intensity scale is linear and the background was not subtracted.

each experimental point corresponds to a single QDM. Anticrossing energies were obtained by measuring the minimum energy separation between the two exciton branches of each spectrum and barrier thicknesses were obtained by measuring the slope *ed* of the indirect state.

The anticrossing energy was found to decrease exponentially with increasing QD separation, as expected for the quantum mechanical tunneling of a
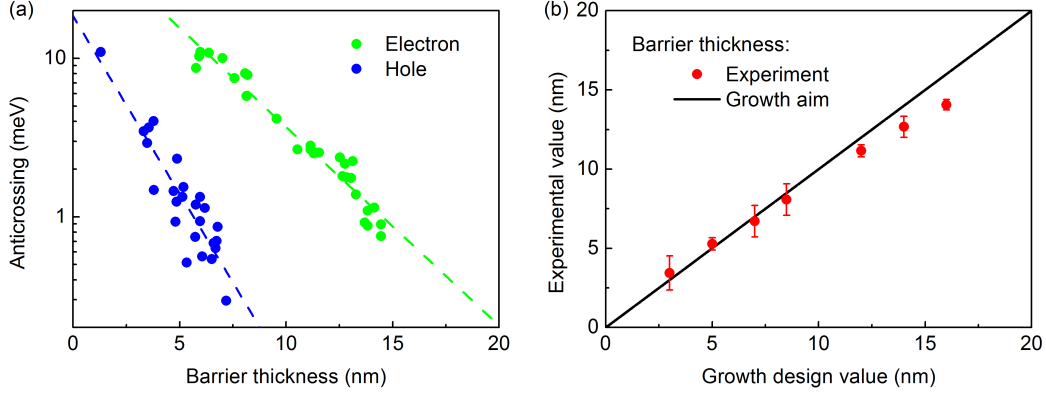
Figure 5.5: (a) Anticrossing energies as a function of barrier thickness for electron and hole tunneling extracted from neutral exciton spectra similar to Fig. 1(b). Each point corresponds to a single QDM. Dashed lines are linear fits (on a semilog scale) to all the poins. (b) Comparison between design (black line) and experimental values (red dots) for the barrier thickness. Good agreement demonstrates accurate control over the coupling energy between QDs forming a QDM.

particle through a barrier of potential. Moreover, the anticrossing energies for electrons are found to be an order of magnitude larger than for holes in the range of thicknesses studied and the ratio of the slopes of the data points for holes and electrons is 1.8 ± 0.1. This is mostly due to the higher effective mass of holes compared to electrons and were observed previously [112]. However, the slopes extrapolated from our results are about twice the values previously reported. This is attributed to the different types of QDs used for both studies. Indeed, previous experiments were performed on InAs QDs partially capped with GaAs and then annealed at high temperature to achieve height control. This other method used for selective tunneling of the carriers leads to different QDs properties. Our results therefore quantify the impact of the QDMs fabrication process on the dependence of tunnel coupling energies with barrier thickness.

Control over the barrier thickness was estimated by comparing growth nominal values with experimentally measured values. Results are shown in Fig. 5.5(b), where statistics were built from the experimental data obtained for each growth design value. Good agreement is found between the fitted

barrier thickness and the nominal growth design. Small deviations are attributed to the fact that the data were collected from a large number of wafers grown over several years under different temperature conditions. Moreover, the values were measured from devices processed from different wafer regions, which might results in growth rate variation.

5.4 Optical spectroscopy

5.4.1 Introduction

In this section, we discuss the electric field dependence of the four main quantum states of a QDM, i.e. the exciton (X), the biexciton (XX), the negatively charged exciton (X^-) and the positively charged exciton (X^+), in a step by step manner. Based on previous work [105, 106, 111], we start with a description of the direct and indirect exciton states accounting for spin-conserving tunneling, exchange and Coulomb interactions, and Pauli exclusion. We then expand the model to include the QCSE on the direct exciton states and show that this extended model is in excellent agreement with the experimental data. We here only consider hole tunneling (electron tunneling can be described analogously).

5.4.2 Notations

To describe the quantum states of a QDM, we use the matrix notations $\begin{pmatrix} e_T & e_B \\ h_T & h_B \end{pmatrix}$ developed in [106], where the first (second) column refers to the carriers in the top (bottom) QD and the first (second) row indicates the number of electrons (holes) in each QD. Moreover, underlines are used to indicate the carriers involved in the optical transition, e.g. $\begin{pmatrix} \underline{1} & 0 \\ 1 & \underline{1} \end{pmatrix}$ for the optical transition of X^+ where the electron in the top QD radiatively recombines with the hole in the bottom QD. Optical transitions involving carriers localised in the same (different) QD(s) are referred to as "direct" ("indirect") transitions. Specific spin states are labelled using arrows using the fact that carriers have only two spin projections in the ground state of a QD. $\{\uparrow, \downarrow\} \equiv \pm 1/2$ are used

for the electron spin and $\{\Uparrow, \Downarrow\} \equiv \pm 3/2$ for the hole spin, e.g. $\begin{pmatrix} \uparrow\downarrow & 0 \\ \Downarrow & \Uparrow \end{pmatrix}$ for a XX state with one hole that has tunneled from the top to the bottom QD. Finally, spin-singlet and -triplet configurations are specified using the subscript S and T, e.g. $\begin{pmatrix} \uparrow & 0 \\ \Downarrow & \Uparrow \end{pmatrix}_S$ and $\begin{pmatrix} \uparrow & 0 \\ \Downarrow & \Uparrow \end{pmatrix}_T$ for the hole spin-singlet and -triplet states of an indirect X^+ state. The spin-singlet state is $\left(|\Uparrow\Downarrow\rangle - |\Downarrow\Uparrow\rangle \right)/\sqrt{2}$ and the triplet states are $\left(|\Uparrow\Downarrow\rangle + |\Downarrow\Uparrow\rangle \right)/\sqrt{2}$, $|\Uparrow\Uparrow\rangle$, and $|\Downarrow\Downarrow\rangle$ respectively with spin-projections $T = 0$, $T = 3$, and $T = -3$.

In our description, we will use state configurations with the carriers wavefunctions localized in one or the other QD as basis states. These configurations are realized away from the energy level resonances. Around the resonances, molecular states corresponding to coherent superpositions of the basis states will form. Spin degenerate states in which all spins are flipped are not considered.

5.4.3 Neutral exciton

Using the basis $\left\{ \begin{pmatrix} \uparrow & 0 \\ \Downarrow & 0 \end{pmatrix}, \begin{pmatrix} \uparrow & 0 \\ 0 & \Downarrow \end{pmatrix}, \begin{pmatrix} \uparrow & 0 \\ \Uparrow & 0 \end{pmatrix}, \begin{pmatrix} \uparrow & 0 \\ 0 & \Uparrow \end{pmatrix} \right\}$ containing all possible spin configurations, i.e. the direct and indirect bright exciton spin states (electron and hole spins with opposite projections) and the direct and indirect dark exciton spins states (electron and hole spins with parallel projections), the Hamiltonian for the neutral exciton is [105]

$$\hat{\boldsymbol{H}}_X = E_X \boldsymbol{I} + \begin{pmatrix} J & t & 0 & 0 \\ t & E^h - edF & 0 & 0 \\ 0 & 0 & -J & t \\ 0 & 0 & t & E^h - edF \end{pmatrix}, \qquad (5.1)$$

where E_X is the energy of a neutral exciton confined in a single QD (the top QD in this case), $\boldsymbol{I}$ is the idendity matrix, F is the electric field applied to the structure. The energy difference between the dark and bright direct exciton states is given by $2J$, where J is the electron-hole exchange energy, while the bright and dark indirect exciton states have the same energy as the electron-hole exchange interaction is expected to diminish when the charge carriers are separated in different QDs. We only consider here the short-

range exchange interaction and only the bright-dark splitting which is the largest effect in the fine structure [76]. We will discuss the bright states splitting arising from the long-range exchange interaction in section 5.5. The off-diagonal matrix element t gives the tunnel coupling energy (of a single hole in this case) between the direct and indirect states. There is no coupling between the bright and dark states as tunneling preserves spin. E^h is the energy required to move the hole from the top to the bottom QD at zero field (and therefore defines the electric field at which energy levels from both QDs are tuned into resonance), and edF is the linear Stark shift induced by the dipole moment of the indirect states where e is the charge of the electron, and d is the distance between the two QDs forming the QDM.

The first two eigenvalues of $\hat{\boldsymbol{H}}_X$ provide the bright exciton eigenenergies of the QDM given by

$$E_\pm = E_X + \frac{J + E^h - edF}{2} \pm \frac{\sqrt{(J - E^h + edF)^2 + 4t^2}}{2}, \qquad (5.2)$$

and are plotted in Fig. 5.6(a) where the different transitions to the vacuum state are indicated. Optically-allowed transitions are represented by plain lines and forbidden transitions by dashed lines. The physical effect of the different terms in Eq. (5.1) on the energy levels is also schematically illustrated in Fig. 5.6(a). The corresponding optical spectrum is shown in Fig. 5.6(b), where spectral lines originate only from bright transitions.

The eigenstates of $\hat{\boldsymbol{H}}_X$ can also be computed from Eq. (5.1) and the neutral bright (dark states can be found analogously) exciton quantum states of the QDM are found to be the symmetric and antisymmetric coherent superpositions of the direct and indirect excitons (see Fig. 5.6(b))

$$|\Psi_+\rangle = \cos\theta \begin{pmatrix} \uparrow & 0 \\ \Downarrow & 0 \end{pmatrix} + \sin\theta \begin{pmatrix} \uparrow & 0 \\ 0 & \Downarrow \end{pmatrix}, \qquad (5.3)$$

$$|\Psi_-\rangle = \sin\theta \begin{pmatrix} \uparrow & 0 \\ \Downarrow & 0 \end{pmatrix} - \cos\theta \begin{pmatrix} \uparrow & 0 \\ 0 & \Downarrow \end{pmatrix}, \qquad (5.4)$$

where
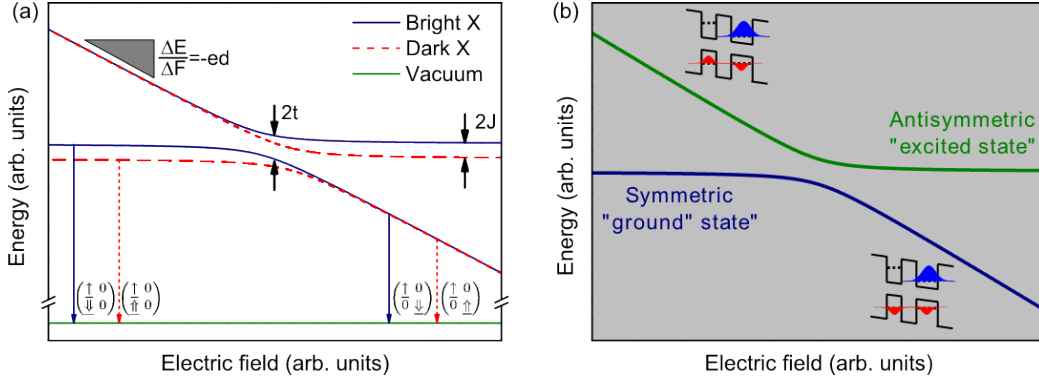
Figure 5.6: (a) All possible eigenenergies and transitions for the neutral exciton states. The physical effect of the different parameters of the QDM are indicated. (b) Calculated optical spectrum of the neutral exciton showing the symmetric and antisymmetric branches.

$$\theta = \tan^{-1}\left[\frac{(E_+ - E_-) - J + E^h - edF}{2t}\right].\qquad(5.5)$$

The centre of the anticrossing is characterised by $\theta = \pi/4$ and away from the resonance the state of the QDM is close to purely direct or indirect. The symmetric state has a lower energy and is often referred to as the molecular ground state in analogy to real molecules, while the antisymmetric state is usually referred to as the excited state [113].

An example of a neutral exciton spectrum obtained experimentally is plotted in Fig. 5.7 and is qualitatively comparable to the calculated spectrum in Fig. 5.6(b).

5.4.4 Biexciton

The biexciton spectrum, arising from the transitions between the XX states and the X states, is slightly more complicated than the exciton spectrum. The different possible spin configurations for the XX state are the direct state, which is a singlet state due to the Pauli exclusion principle, and the indirect singlet and degenerate triplet states (T=0 and T=±3). This leads to the basis $\left\{\begin{pmatrix}\uparrow\downarrow & 0\\ \Uparrow\Downarrow & 0\end{pmatrix}, \begin{pmatrix}\uparrow\downarrow & 0\\ \Downarrow & \Uparrow\end{pmatrix}_S, \begin{pmatrix}\uparrow\downarrow & 0\\ \Uparrow & \Downarrow\end{pmatrix}_T\right\}$, for which the Hamiltonian is [111]
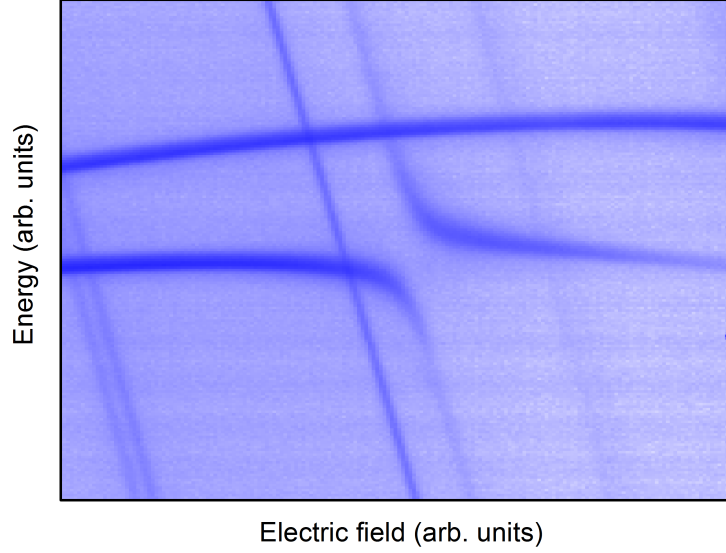
Figure 5.7: Experimental spectrum of a neutral exciton in a QDM. The intensity scale is logarithmic and the background was subtracted.

$$\hat{\boldsymbol{H}}_{XX} = E_{XX}\boldsymbol{I} + \begin{pmatrix} 0 & \sqrt{2}t & 0 \\ \sqrt{2}t & E^h - edF & 0 \\ 0 & 0 & E^h - edF \end{pmatrix}, \qquad (5.6)$$

where E_{XX} is the confinement energy for a biexciton confined in a single QD and E^h is the Coulomb energy required to move one of the biexciton holes to the bottom QD. There is no electron-hole exchange interaction term in $\hat{\boldsymbol{H}}_{XX}$ as the total spin of the electrons, which must be in the singlet state, is 0. We now have a factor $\sqrt{2}$ in front of the tunnel coupling energy as two indistinguishable holes can potentially tunnel from the direct state to the singlet hole spin configuration of the indirect state. There are no coupling terms between the triplet and singlet states since tunneling conserves spin and the triplet state will therefore pass straight through the anticrossing.

The three different XX states will decay to the four different X states discussed previously leading to a total of 12 possible transitions. Among these transitions, only 8 are optically allowed: 4 from the XX singlet states and 4 from the XX triplet states. Fig. 5.8(a) shows the 4 optical transitions from the XX singlet states and Fig. 5.8(b) plots the resulting "X-shaped"
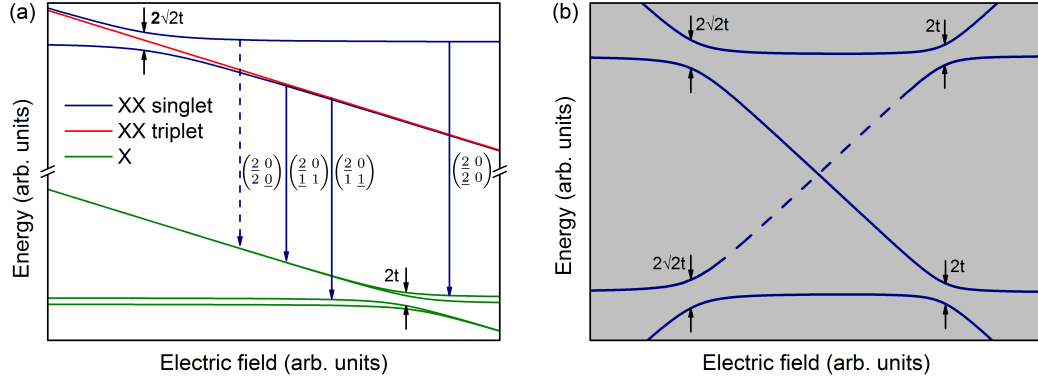
Figure 5.8: (a) Optical transitions from the XX singlet states and (b) resulting optical spectrum.

optical spectrum that is usually referred to as an "x-pattern".

The upper and lower energy bound of the x-pattern are the direct transitions $\left(\begin{smallmatrix} 2 & 0 \\ \underline{2} & 0 \end{smallmatrix}\right)$, which is similar to the XX transition of a single QD, and $\left(\begin{smallmatrix} 2 & 0 \\ \underline{1} & 1 \end{smallmatrix}\right)$, which is similar to an X^- transition in a single QD with a spectator hole in the second QD. Within the x-pattern, two indirect transitions anticross with the direct transitions forming in total four anticrossings. One pair of anticrossings of size $2t$ occurs at the same electric field as the exciton anticrossing since the X state is the final state in the transition. The second pair of anticrossings of size $2\sqrt{2}t$ arises from the anticrossing in the XX state and occurs at slightly different electric field due to a small difference in Coulomb energies between the states involved.

The transition $\left(\begin{smallmatrix} 2 & 0 \\ 2 & \underline{0} \end{smallmatrix}\right)$ represented by a dotted line in Fig. 5.8(a) is possible due to the partial tunneling of one of the hole from the top to the bottom QD. However, this transition will be extremely weak away from the hole energy levels resonances (see dotted line in Fig 5.8(b)) and visible only around these resonances.

Fig. 5.9(a) shows the 4 optical transitions from the XX degenerate triplet states. The triplet state $T = 0$ only decays to the bright exciton states while the triplet states $T = \pm 3$ only decay to the dark exciton states. Fig. 5.9(b) plots the resulting spectral lines (in red), which are added to the previously obtained x-pattern. The triplet states transitions pass straight through the
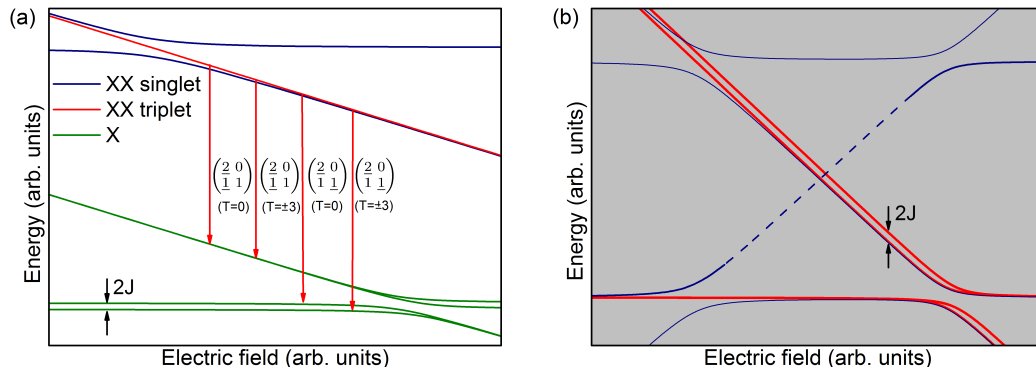
Figure 5.9: (a) Optical transitions from the XX triplet states and (b) resulting spectral line plotted in red.
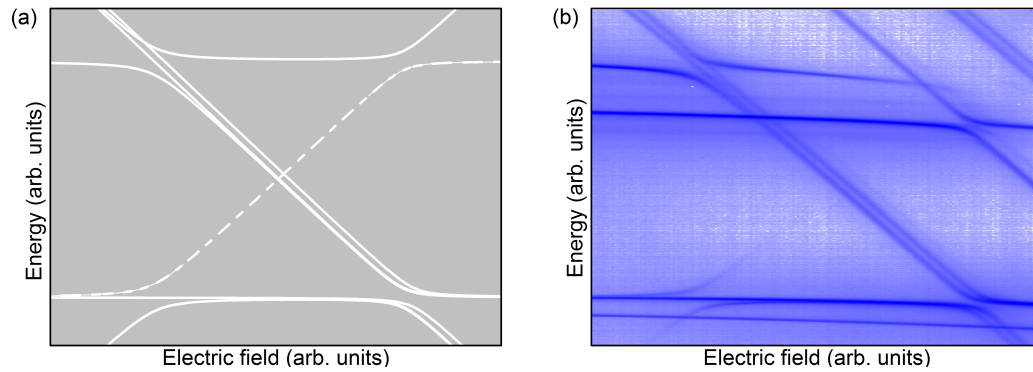
Figure 5.10: Comparison between the (a) calculated and (b) experimental optical spectrum of the XX state in a QDM (spectral lines from other transitions are also observable). The intensity scale in (b) is logarithmic and the background was subtracted.

anticrossings arising from the XX anticrossing, as no coupling is possible between the singlet and triplet indirect states.

Finally, the calculated x-pattern obtained previously (see Fig. 5.10(a)) is compared to a typical example of an experimental x-pattern corresponding to the XX state (see Fig. 5.10(b) where spectral lines from other states of the QDM are also present).

5.4.5 Positively charged exciton

Similarly to the XX case, the singlet and triplet spin configurations will form the basis for X$^+$. Moreover, the electron-hole exchange energy J must now be considered in the indirect states, where one hole and one electron are present in the top QD. Therefore, the triplet states $\{T = 0, \pm 3\}$ are not degenerate anymore and the basis is $\left\{ \begin{pmatrix} \uparrow & 0 \\ \Uparrow\Downarrow & 0 \end{pmatrix}, \begin{pmatrix} \uparrow & 0 \\ \Downarrow & \Uparrow \end{pmatrix}_S, \begin{pmatrix} \uparrow & 0 \\ \Uparrow & \Downarrow \end{pmatrix}_{T=0}, \begin{pmatrix} \uparrow & 0 \\ \Downarrow & \Downarrow \end{pmatrix}_{T=-3}, \begin{pmatrix} \uparrow & 0 \\ \Uparrow & \Uparrow \end{pmatrix}_{T=3} \right\}$, leading to the Hamiltonian [106]

$$\hat{\boldsymbol{H}}_{X^+} = E_{X^+}\boldsymbol{I} + \begin{pmatrix} 0 & \sqrt{2}t & 0 & 0 & 0 \\ \sqrt{2}t & E^h - edF & J & 0 & 0 \\ 0 & J & E^h - edF & 0 & 0 \\ 0 & 0 & 0 & E^h - edF + J & 0 \\ 0 & 0 & 0 & 0 & E^h - edF - J \end{pmatrix}, \quad (5.7)$$

where E_{X^+} is the X$^+$ confinement energy in the top QD, E_h is the Coulomb energy required to move one of the X$^+$ holes to the bottom QD. Similarly to the XX case, a factor $\sqrt{2}$ is needed in front of the tunnel coupling energy and no coupling terms between the triplet and singlet states are needed.

The different X$^+$ eigenstates will decay to the single hole state, for which the basis is $\left\{ \begin{pmatrix} 0 & 0 \\ \Uparrow & 0 \end{pmatrix}, \begin{pmatrix} 0 & 0 \\ 0 & \Uparrow \end{pmatrix} \right\}$, leading to the Hamiltonian

$$\hat{\boldsymbol{H}}^h = E_h\boldsymbol{I} + \begin{pmatrix} 0 & t \\ t & E^h - edF \end{pmatrix}, \quad (5.8)$$

where E_h is the confinement energy of a single hole and E^h is the energy to move the hole from the top to the bottom QD at zero field. As only the difference of the confinement energies $E_{X^+} - E_h$ is measurable through optical spectroscopy, we will consider in the following that the single hole confinement energy is 0 so that E_{X^+} is directly measurable on the spectrum.

The transitions from the singlet X$^+$ states to the single hole states are shown in Fig. 5.11(a). The resulting optical spectrum (see Fig. 5.11(b)) is qualitatively equivalent to the spectrum resulting from the radiative transi-
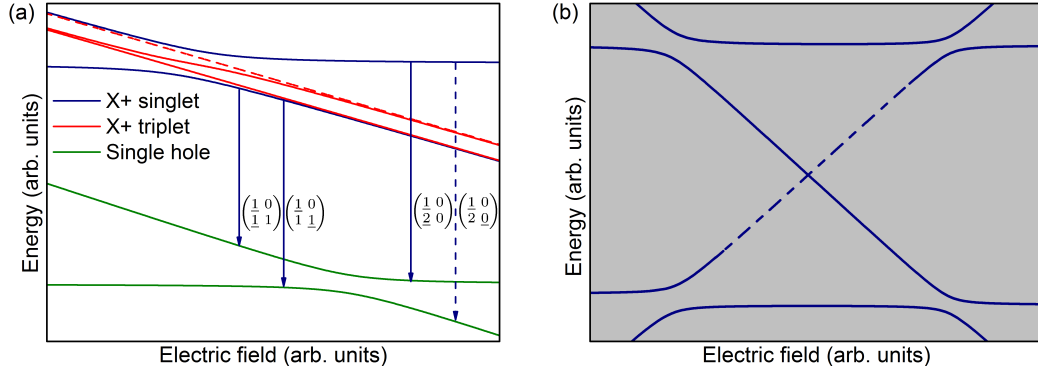
Figure 5.11: (a) Radiative transitions from the X^+ singlet states to the single hole states and (b) resulting optical spectrum.
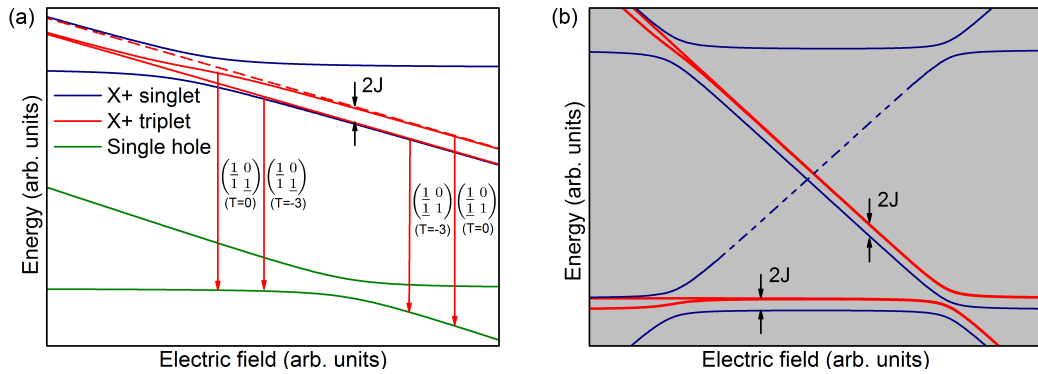
Figure 5.12: (a) Radiative transitions from the X^+ triplet states to the single hole states and (b) resulting optical spectrum.

tions from the XX singlet states.

The transitions from the non-degenerate triplet X^+ states to the single hole states are shown in Fig. 5.12(a). The resulting optical spectrum is shown in Fig. 5.12(b). The final spectrum qualitatively differ from the XX case by the presence of an electron-hole exchange interaction in the indirect X^+ states.

Finally, the calculated x-pattern obtained previously (see Fig. 5.13(a)) is compared to a typical example of an experimental x-pattern corresponding to the X^+ state (see Fig. 5.13(b), where spectral lines from other states of the QDM or other QDMs are also osbervable).

Figure 5.13: Comparison between the (a) calculated and (b) experimental optical spectrum of the X^+ state in a QDM. The intensity scale in (b) is logarithmic and the background was subtracted.

5.4.6 Negatively charged exciton

The two basis states for X^- are $\left\{ \begin{pmatrix} \uparrow\downarrow & 0 \\ \Uparrow & 0 \end{pmatrix}, \begin{pmatrix} \uparrow\downarrow & 0 \\ 0 & \Uparrow \end{pmatrix} \right\}$. Indeed, as the electrons are both located in the same QD, their only possible spin configuration is the singlet state according to the exclusion principle. Moreover, their total spin is 0 leading to no electron-hole exchange interaction. The Hamiltonian in this basis is

$$\hat{\boldsymbol{H}}_{X^-} = E_{X^-}\boldsymbol{I} + \begin{pmatrix} 0 & t \\ t & E^h - edF \end{pmatrix}. \tag{5.9}$$

The bright and dark optical transitions are energetically degenerated as shown in Fig. 5.14(a). The calculated optical spectrum of the X^- state is plotted in Fig. 5.14(b) and an experimental spectrum is shown in Fig. 5.15, where spectral lines corresponding to other states of the QDM or other QDMs are also observable.

5.4.7 Quantum confined Stark effect

In order to fully describe the QDM electric field dependent spectrum, the parabolic QCSE acting on charge carriers in the same QD and due the small dipole moment of direct states must also be considered. The QCSE was neglected in previous studies of QDMs due to its limited influence at low
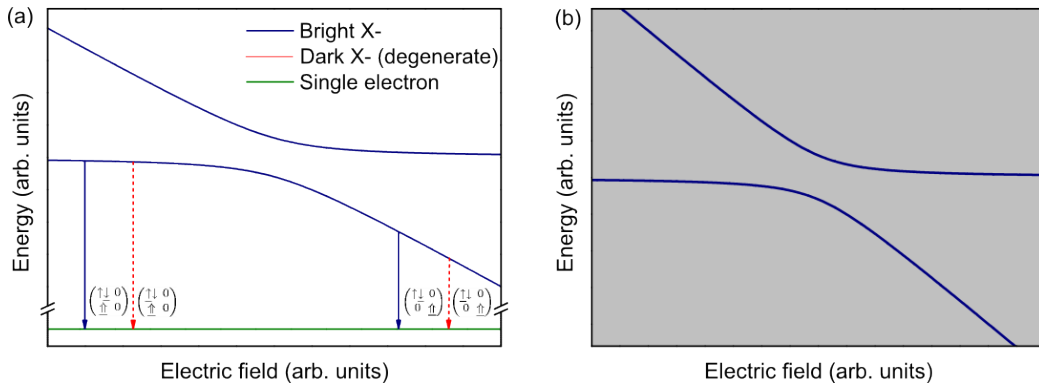
Figure 5.14: (a) All possible eigenenergies and transitions for the neutral exciton states. The bright and dark states are degenerate in the X$^-$ case due to the presence of two electrons in the top QD suppressing the e-h exchange interaction. (b) Calculated optical spectrum of X$^-$.
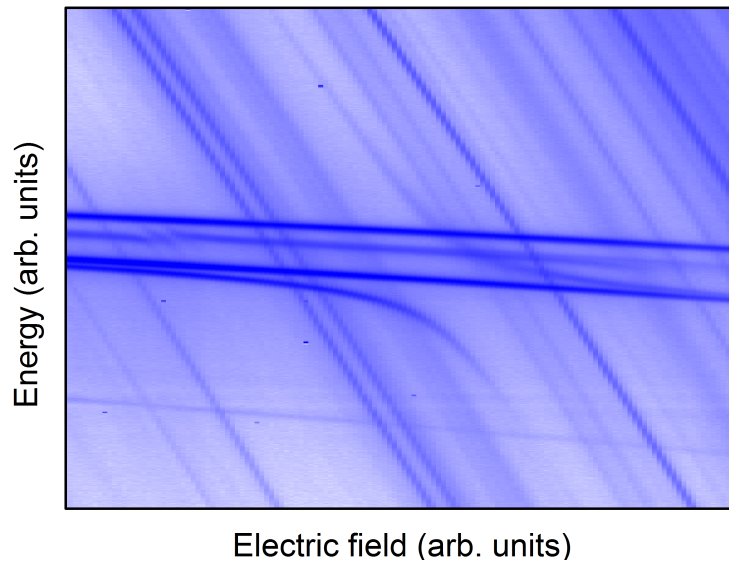
Figure 5.15: Experimental spectrum of X$^-$. The intensity scale is logarithmic and the background was subtracted.

electric fields compared to the linear Stark effect originating from the dipole moment of the indirect state. In our structures however, large electric fields can be applied without quenching the emission allowing therefore for clear observation of the QCSE in the top QD, providing physical insight into strain-induced QDs. The QCSE is modelled by diagonal matrices containing energy

terms of the form $pF + \beta F^2$, where p and β are respectively the permanent dipole moment and the polarisability of the exciton in the top QD. For the X state, the QCSE term is

$$\hat{\boldsymbol{H}}_X^{QCSE} = \begin{pmatrix} p_X F + \beta_X F^2 & 0 & 0 & 0 \\ 0 & 0 & 0 & 0 \\ 0 & 0 & p_X F + \beta_X F^2 & 0 \\ 0 & 0 & 0 & 0 \end{pmatrix}, \quad (5.10)$$

where by definition the indirect states leading only to indirect transitions exhibit no QCSE. For the XX state, we find

$$\hat{\boldsymbol{H}}_{XX}^{QCSE} = \begin{pmatrix} p_{XX} F + \beta_{XX} F^2 & 0 & 0 \\ 0 & p_{XX_i} F + \beta_{XX_i} F^2 & 0 \\ 0 & 0 & p_{XX_i} F + \beta_{XX_i} F^2 \end{pmatrix}, \quad (5.11)$$

where the indirect XX states (labelled XX_i) can lead to direct transitions similar to an X^- transition from the top QD with a spectator hole in the bottom QD. Similarly, we find for the X^+ state

$$\hat{\boldsymbol{H}}_{X^+}^{QCSE} = \begin{pmatrix} p_{X^+} F + \beta_{X^+} F^2 & 0 & 0 & 0 & 0 \\ 0 & p_{X_i^+} F + \beta_{X_i^+} F^2 & 0 & 0 & 0 \\ 0 & 0 & p_{X_i^+} F + \beta_{X_i^+} F^2 & 0 & 0 \\ 0 & 0 & 0 & p_{X_i^+} F + \beta_{X_i^+} F^2 & 0 \\ 0 & 0 & 0 & 0 & p_{X_i^+} F + \beta_{X_i^+} F^2 \end{pmatrix}, \quad (5.12)$$

where the indirect X^+ states (labelled X_i^+) can lead to direct transitions comparable to an X transition from the top QD with a spectator hole in the bottom QD. For the X^- state, we find

$$\hat{\boldsymbol{H}}_{X^-}^{QCSE} = \begin{pmatrix} p_{X^-} F + \beta_{X^-} F^2 & 0 \\ 0 & 0 \end{pmatrix}, \quad (5.13)$$

where the indirect X^- state only leads to indirect transitions without QCSE. Finally, the single hole direct and indirect states are assumed to exhibit no QCSE.
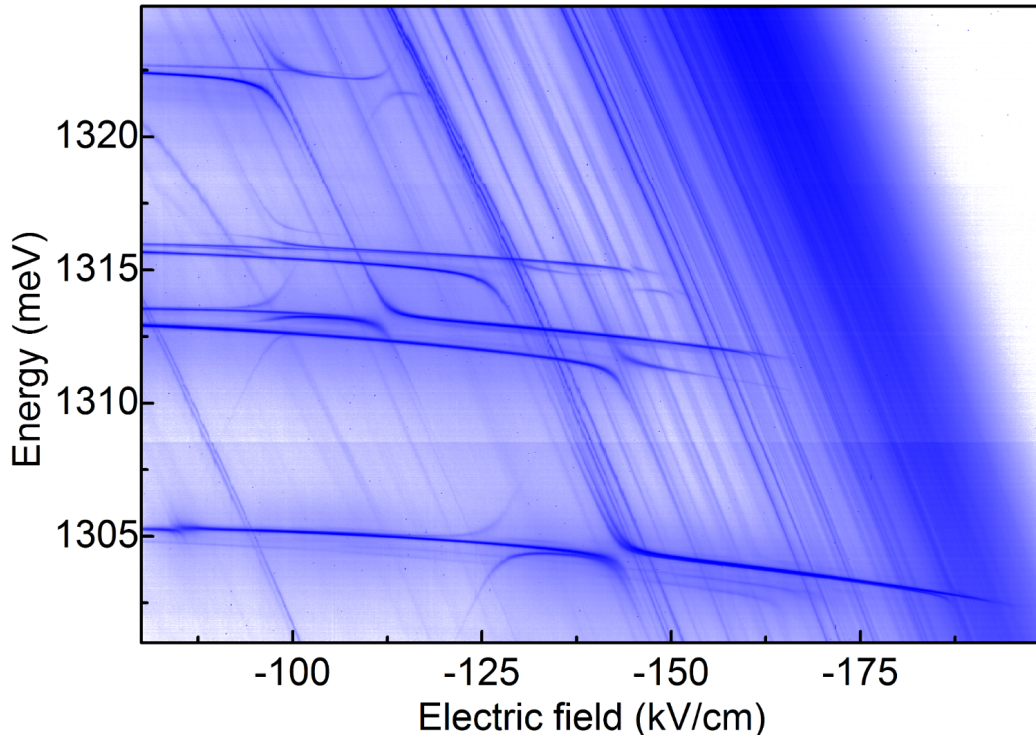
Figure 5.16: High-resolution spectroscopy of a QDM in a diode structure where all the optically-allowed transitions from the four main states were observed for hole tunneling. The intensity scale is logarithmic and the background was subtracted.

5.4.8 Full picture

An important advantage of our structures is to be able to access all the optically-allowed transitions from the main QDM states with a single device. Moreover, the $Al_{0.75}Ga_{0.25}As$ superlattice on each side of the intrinsic region allows for a much wider range of electric fields to be addressed and therefore allows for accurate measurements of the QCSE in the direct state. Electric-field dependent optical spectroscopy of a typical QDM and for hole tunneling is shown in Fig. 5.16.

Energies extracted from this figure are plotted in Fig. 5.17(a) and are fitted to the model previously developed (see Fig. 5.17(b)). For clarity, transitions originating from the same QDM state are plotted using the same colour. The fit is in excellent agreement with experimental data although
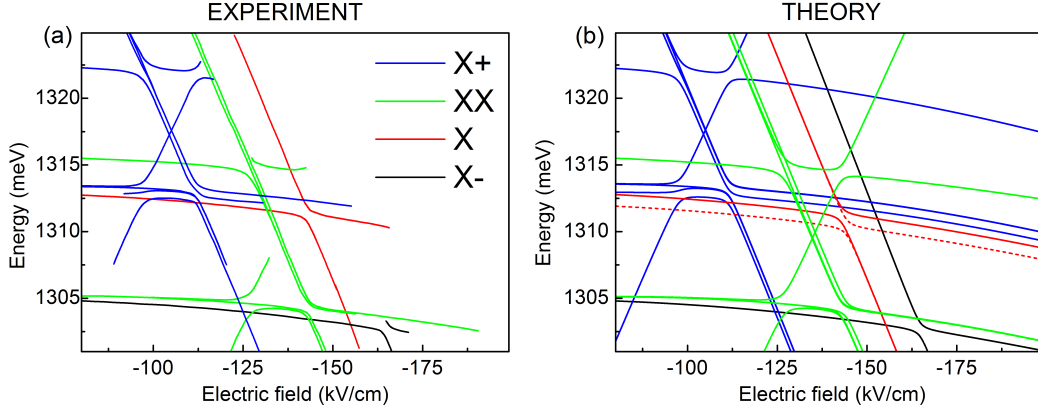
Figure 5.17: (a) Extracted energies of the different transitions from Fig. 5.16. (b) Theoretical calculations obtained using previously developed theoretical models and adding the QCSE.

some transitions are not visible in all field ranges due their reduced optical intensity.

The fitting parameters used are listed in Table 5.1. The permanent dipole moments p and the polarisabilities β found for the different direct transitions are higher than those measured for similar single QDs (see Table 5.2 and [93]). Higher values were also found for all the other QDMs studied. We attribute this to the fact that p and β are related to exciton states confined in the top QD which is strain nucleated and can differ in geometry from the self-assembled QDs from which the reference values are taken. Additionally, weak delocalization of the electron between both QDs could also lead to the higher values observed.

Values obtained for d are close to the nominal thickness $d=7\pm0.5$nm as already discussed in Fig. 5.5(b). Values for t agree well with Fig. 5.5(a) and with values found in [112] for QDMs with same d. The measured electron-hole exchange interaction J is similar to values found for single QD [76] and QDMs [106] in the range 0.1-0.5meV. Finally, the fact that t and d are similar for all exciton complexes indicates that they originate from the same QDM. Moreover, the direct transition from the indirect X^+ (resp. XX) state is close in energy to the direct X (resp. XX^-) transition. This is expected for a single QDM as the only difference between the two transitions is a spectator

	X	XX	XX$_i$	X$^+$	X$_i^+$	h	X$^-$
E (meV)	1312.39	2628.34	-	1312.39	-	0	1304.45
p (μeVkV^{-1}cm)	-14.85	-23.57	-39.14	-21.16	-34.22	0	-18.76
β (μeVkV^{-2}cm^2)	-0.175	-0.299	-0.241	-0.222	-0.232	0	-0.180
d (nm)	6.65	6.65	-	6.48	-	6.48	6.97
t (meV)	0.586	0.586	-	0.569	-	0.569	0.531
E^h (meV)	93.98	81.44	-	62.29	-	72.30	112.99
J (meV)	0.434	0.434	-	0.318	-	-	-

Table 5.1: Experimental values of the different parameters of the model for the four transitions X,XX,X$^+$, and X$^-$ used to obtain Fig. 5.17(b).

	X	XX	X$^+$	X$^-$
p (μeVkV^{-1}cm)	5.0$\pm$5.1	0.6$\pm$4.8	-14.1$\pm$12.5	3.6$\pm$2.7
β (μeVkV^{-2}cm^2)	-0.097$\pm$0.009	-0.084$\pm$0.010	-0.111$\pm$0.021	-0.091$\pm$0.010

Table 5.2: Reference values for permanent dipole moments and polarisabilities obtained for single QDs showing an increase in the case of QDMs. Values are extracted from [93].

hole in the adjacent QD in the X$^+$ (resp. XX) case, which has little effect on the transition energy. Finally, we measured the fine structure splitting to confirm the assignment of the different neutral and charged lines.

5.5 Electrical control of the exciton fine structure of a quantum dot molecule

We now discuss the field dependence of the fine structure between the bright neutral exciton states in a QDM. Indeed, though the electron-hole exchange coupling that defines the fine structure splitting and polarisation anisotropy of the bright states of a neutral exciton in a single QD is well understood [76, 58], the case of excitons confined in a QDM has never been investigated experimentally. A recent theoretical study [114] predicted that the fine structure splitting of an exciton in a QDM can be controlled by confining the electron and hole in neighbouring QDs and tuning the electron-hole wavefunction overlap electrically. In this section, we show that not only the magnitude of the fine structure splitting can be manipulated but also the

eigenstate orientation, indicating a coupling between dissimilar spin states which is not accounted for in [114]. As demonstrated in chapter 4 and in [115], such coupling makes it possible to perform quantum operations on spin qubits. Combined with the extended lifetime of an indirect exciton confined in a QDM (see chapter 6 and [102]), the coupling presented in this section is likely to enhance the number of operations that can be performed on a stored exciton qubit.

We here describe the QDM spectrum for the case of hole tunneling (electron tunneling can be treated analogously). The two bright exciton eigenstates of a single QD are polarised along the [110] and $[1\bar{1}0]$ crystal axes, annotated horizontal (H) and vertical (V), as a consequence of the electron-hole exchange interaction. For this reason we choose to express the eigenstates of a neutral exciton in the basis of two H/V polarised direct states and two H/V polarised indirect states $\left\{ \begin{pmatrix} 1 & 0 \\ 1 & 0 \end{pmatrix}_H, \begin{pmatrix} 1 & 0 \\ 1 & 0 \end{pmatrix}_V, \begin{pmatrix} 1 & 0 \\ 0 & 1 \end{pmatrix}_H, \begin{pmatrix} 1 & 0 \\ 0 & 1 \end{pmatrix}_V \right\}$. Using this basis, the eigenstates have the general form $|\Psi_{FSS}\rangle = A \begin{pmatrix} 1 & 0 \\ 1 & 0 \end{pmatrix}_H + B \begin{pmatrix} 1 & 0 \\ 1 & 0 \end{pmatrix}_V + C \begin{pmatrix} 1 & 0 \\ 0 & 1 \end{pmatrix}_H + D \begin{pmatrix} 1 & 0 \\ 0 & 1 \end{pmatrix}_V$.

The Hamiltonian describing the excitonic states consists of one spin independent and one spin dependent part, $\hat{\boldsymbol{H}} = \hat{\boldsymbol{H}}_1 + \hat{\boldsymbol{H}}_2$. In the absence of anisotropic exchange interaction the two spin states are degenerate and $\hat{\boldsymbol{H}}_1$, accounting for kinetic energies, Coulomb interaction and spin conserving tunneling, is sufficient to describe the electric field dependence of the spectrum. We find

$$\hat{\boldsymbol{H}}_1 = E_X \boldsymbol{I} + \begin{pmatrix} pF + \beta F^2 & 0 & t & 0 \\ 0 & pF + \beta F^2 & 0 & t \\ t & 0 & E^h - edF & 0 \\ 0 & t & 0 & E^h - edF \end{pmatrix}, \quad (5.14)$$

where the different terms have the same signification as previously described. This Hamiltonian was used to fit the experimental spectral lines of the neutral exciton states of the QDM under study, which has a hole tunneling resonance at positive electric field (see Fig. 5.18(a)). The values obtained

E (meV)	1337.01
p (μeVkV^{-1}cm)	-91.08
β (μeVkV^{-2}cm^2)	-0.40
d (nm)	5.39
t (meV)	0.31
E^h (meV)	67.36

Table 5.3: Experimental values of the different parameters of Eq. (5.14) used to obtain the fits in Fig. 5.18(a).

for the different parameters of Eq. (5.14) are shown in Table 5.3.

The fine structure of the exciton spectrum was studied in terms of $|S|$, the energy splitting between the two orthogonally polarised states, and θ, the angle that describes the orientation of the eigenstates relative to the crystal lattice. The experimental values of $|S|$ for our QDM are plotted in Fig. 5.18(b) as circles. In the direct state, the fine structure is similar to that of an exciton confined in a single QD. The electron-hole exchange interaction is strong since both charge carriers are confined in the same QD and $|S|$ is on the order of 10 to $100\mu eV$. At the anticrossing $|S|$ reduces as a consequence of the weakened exchange interaction when the electron and hole are separated in different QDs. However, not only the energy separation of the eigenstates is affected at the transition from the direct to indirect exciton configuration but also the eigenstate orientation θ, as shown in Fig. 5.18(c) where experimental values for our QDM are plotted as circles. We model the electric field dependence of the anisotropic electron-hole exchange interaction on the spectrum of an exciton confined in a QDM by introducing the $\hat{\boldsymbol{H}}_2$ Hamiltonian

$$\hat{\boldsymbol{H}}_2 = \begin{pmatrix} 0 & \delta_{DD} & 0 & \delta_{DI} \\ \delta_{DD} & S_D + \gamma F & \delta_{DI} & 0 \\ 0 & \delta_{DI} & 0 & 0 \\ \delta_{DI} & 0 & 0 & S_I \end{pmatrix}. \tag{5.15}$$

The 2×2 sub-block in the top left corner of $\hat{\boldsymbol{H}}_2$ describes the field dependence of the direct exciton H and V basis states and is equivalent to the

fine structure Hamiltonian of the exciton states in a single QD subjected to a vertical electric field [12]. At zero electric field the fine structure splitting of the direct exciton is S_D, and it increases linearly with increasing field due to a small difference in the permanent dipole moment along the z-direction for the direct basis states, γ. The direct exciton H and V basis states are coupled via the term δ_{DD} which causes them to mix when the fine structure splitting approaches zero and thus rotates the eigenstates away from the H/V basis. The 2×2 sub-block in the lower right corner of the Hamiltonian describes the field dependence of the indirect exciton H and V basis states. The fine structure splitting of the indirect states is expected to be substantially smaller than that of the direct states due to the small exchange interaction between the electron and hole when they are separated in different QDs. For this reason the indirect exciton splitting is described by a single term, S_I ($< S_D$), and any field dependence of the splitting or coupling between the indirect basis states is disregarded. Finally we consider the coupling terms between the direct and indirect states where δ_{DI} represents the coupling between dissimilar spin states (direct H to indirect V or direct V to indirect H).

$|S|$ and θ for both the high and low energy branch of the exciton spectrum obtained from Eq. (5.15) are plotted in Fig. 5.18(b) and (c) as plain lines. The orientation of the eigenstates to the crystal lattice is calculated as $\theta = sign\,(B/A) \times \arctan\,(B^2/A^2)$ for the lowest energy eigenstate of each branch. We have here assumed that it is only the direct components of the eigenstate that are visible in a photoluminescence measurement since the indirect components have substantially weaker oscillator strength. Excellent agreement is found between the experimental data and the values obtained with our model. The corresponding parameters used in Eq. (5.15) are shown in Table 5.4, where S_D and γ agree with the values observed for single QDs [58]. A further discussion on the effect of the other parameters as well as on the exciton fine structure for QDMs subjected to negative electric fields for both hole and electron tunneling resonances can be found in [116].
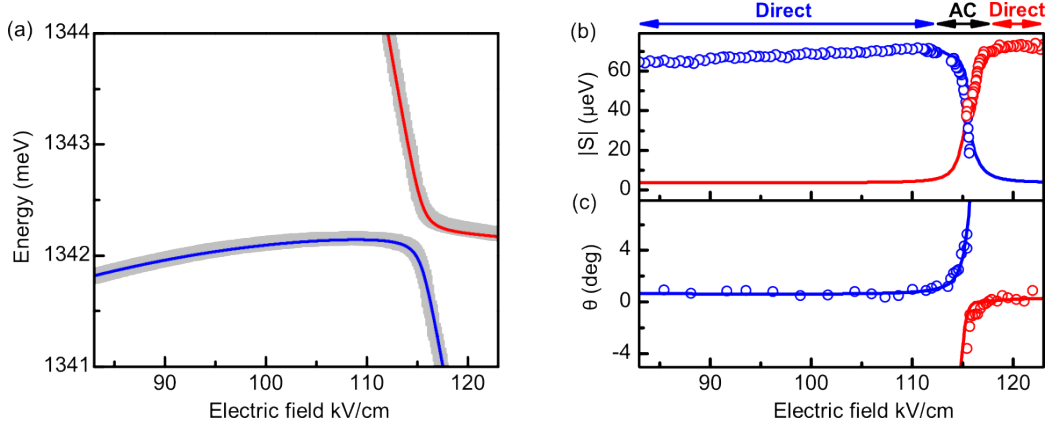
Figure 5.18: (a) Exciton spectrum of the QDM under study. Experimental energies are plotted in gray and calculated energies for the high- and low-energy branch of the spectrum are plotted in red and blue respectively. (b) Fine structure splitting and (c) θ as a function of electric field. Red and blue plain lines correspond respectively to the calculated fine structure of the high- and low-energy exciton branch. Experimental data obtained from the QDM in (a) are plotted as circles.

S_D (μeV)	40.7
γ (μeVkV^{-1}cm)	0.27
S_I (μeV)	-3.7
δ_{DD} (μeV)	-6.5
δ_{DI} (μeV)	8.3

Table 5.4: Experimental values of the different parameters of Eq. (5.15) used to obtain te plain lines in Fig. 5.18(b) and (c).

5.6 Conclusion

In conclusion, we have presented a comprehensive study of QDMs in diode structures. A new method of selectively controlling the tunneling carrier in QDMs using different doping profiles was presented. Precise control over the coupling energy between the QDs was achieved through modification of the barrier thickness. More importantly, the 20 optically-allowed from the four main states X, XX, X$^+$, and X$^-$, of a QDM were observed in the same device and fitted to extended theoretical models. The values obtained for the different parameters of the model were given and compared to referenced

values where applicable. Finally, we reported on the fine structure of neutral excitons confined in QDMs. Our measurements showed a rotation of the eigenstates at the molecular resonance, indicating coupling between dissimilar spin states. A model was developed to account for the observations and excellent agreement with the experiment was achieved. We expect that the $\hat{\boldsymbol{H}}_2$ parameters, which depends on the shape, composition and strain situation for the two QDs, can be engineered to give an electrically controlled dial for the anisotropic exchange interaction in QDMs. This will allow quantum operations to be performed on exciton qubits. In summary, our results demonstrate extensive electrical control of the quantum state of a QDM and provide further insight into the physics of QDMs, which we anticipate will lead to new applications in semiconductor-based quantum information nanotechnologies. In the next chapter, we will concentrate on using QDMs to store single photons as well as their circular polarisation in the spin state of an electron-hole pair, an important step towards a quantum memory for polarised light.

Chapter 6

Exciton-spin memory with a semiconductor quantum dot molecule

6.1 Introduction

Further development of the emerging fields of quantum computing and quantum communication require quantum interfaces between optical "flying" and solid-state "stationary" qubits that enable reversible transfer, storage and manipulation of quantum information [117]. Semiconductors quantum dots (QDs) constitute promising candidates as quantum interfaces between light and matter. Indeed, optical absorption of photons to create an electron-hole pair (or exciton) provides a natural mechanism to transfer quantum information from optical fields into the solid-state. Moreover, optical [118], electrical [115], and optoelectrical [31, 32] coherent control of an exciton qubit in a QD have been successfully demonstrated. However, those approaches do not permit storage of quantum information, which limits their usefulness to the short lifetime of the exciton.

QD-based devices offering spin storage have been developed [119, 120, 121] but rely on the storage of single carriers. Therefore, only pure spin states corresponding to the spin eigenstates can be stored. Indeed, for any

other exciton spin state, the electron and the hole spins are entangled and loss of one of the carriers makes it impossible to recreate the original photon state, which prevents any extension of those schemes to a quantum memory.

Exciton storage has been demonstrated in ensembles of quantum dot molecules (QDMs) [122], quantum posts [123], nanocrystals [124], natural QDs [125] and coupled quantum wells [126, 127, 128]. The main idea behind those works is to spatially separate the carriers for the storage operation. However, those works do not address the issue of transcribing and storing the polarisation of a photon into the spin state of the spatially-separated electron-hole pair, a necessary step towards a quantum memory for polarised light.

In this chapter, we present a novel approach which allows for initialisation and storage of the exciton spin state in a semiconductor QDM. We start with a brief description of the device used in our experiments. We then explain the operating principle behind exciton storage, which is achieved by controlling the recombination rate of the electron-hole pair through electric-field dependent spatial separation in the QDM. We demonstrate microsecond light storage at the single photon level and extend our scheme to exciton-spin storage. Using a vertical magnetic field to lift the degeneracy of the exciton spin states, we show high-fidelity transfer and storage of the circular polarisation of photons into the exciton spin state under resonant optical excitation, with no observable degradation of the fidelity of the operation with time. Finally, we discuss the feasibility of storing superposition states and the limitations on the coherence of the stored states.

6.2   Device structure

The device used consists of a *p-i-n* heterostructure grown by molecular beam epitaxy. Two layers of InAs QDs separated by a thin GaAs layer were grown at the center of the intrinsic region made of a GaAs quantum well clad with a short period superlattice equivalent to $Al_{0.75}Ga_{0.25}As$ on each side, which prevents tunneling of the carriers out of the QDM region when a large vertical electric field is applied. Vertical alignment of the QDs to form QDMs

naturally arises from the strain field generated by the growth of the first layer. Doping extends into the superlattice and allows application of an electric field along the growth direction. This *p-i-n* device is encased in a weak planar microcavity to enhance collection efficiency. We used standard photolithography and wet etching techniques to fabricate a diode with an area of 35×60 μm^2. An opaque metallic film with μm-sized apertures allowed single QDMs to be addressed optically. All our experiments were performed on samples cooled to <10K in a liquid helium cryostat. A diode laser triggered by a pulse pattern generator of tunable period was used for above-band excitation. Resonant and quasi-resonant excitation was achieved using a wavelength-tunable Ti:Sapphire pulsed laser of linewidth $< 30\mu eV$ and of pulse length in the range 2-100ps operating at a fixed period of 12.5ns.

6.3 Operating principle of the exciton memory

A schematic band diagram of the device is shown in Fig. 6.1(a). QDs from the top layer are strain-induced and therefore larger than QDs from the bottom layer [63, 64]. The electron (hole) energy states are consequently lower (higher) in the top QD than in the bottom QD. The exciton naturally relaxes into the top QD at zero electric field as it is the lowest energy configuration ("direct state"). The top QD is positioned on the p-doped side of the diode structure so that applying an electric field in reverse bias separates the hole energy levels of the top and bottom QDs further. On the other hand, the electron energy levels from both QDs are tuned into resonance at a field F_0, which depends on the physical properties of each QDM, and the electron wavefunction hybridises over both QDs. Further increase of the electric field leads to further polarisation of the electron into the bottom QD, the exciton being eventually delocalised over both QDs forming the molecule ("indirect state").

As discussed in chapter 5, the energy of the exciton state as a function of electric field is accurately modelled using the direct and indirect states
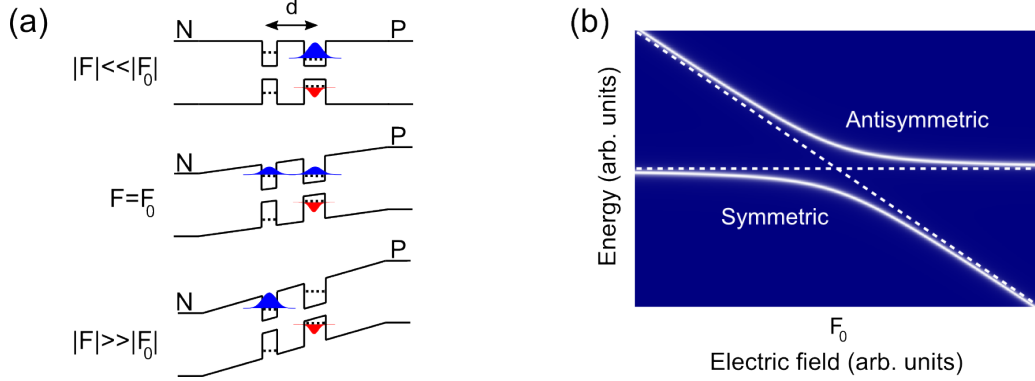
Figure 6.1: (a) Schematic of the band-structure of the QDM at various electric fields. The electron and hole wavefunctions for the low-energy eigenstate are illustrated respectively in blue and red. (b) Calculated (using Eq. (6.1)) photoluminescence spectra of the emission from the QDM eigenstates as a function of electric field. The dotted lines correspond to the energies of the direct and indirect states as a function of electric field.

as basis states (we consider only the bright states here), which leads to the Hamiltonian [105]

$$\boldsymbol{H} = E_0\boldsymbol{I} + \begin{pmatrix} 0 & t \\ t & ed(F - F_0) \end{pmatrix}, \qquad (6.1)$$

where E_0 is the energy of the exciton confined in the top QD at zero electric field, F is the electric field applied to the structure, t is the tunneling rate of the electron from the top to the bottom QD, e is the charge of the electron, d is the distance between the QDs, and F_0 is the field at which electron energy levels are tuned into resonance. The eigenstates of this Hamiltonian are the symmetric (low-energy) and antisymmetric (high-energy) combinations of the basis states [113]. Coherent tunneling of the electron results in an anticrossing between the eigenstates at F_0. Calculated (using Eq. (6.1)) photoluminescence (PL) spectra of the emission from both eigenstates as a function of electric field is shown in Fig. 6.1(b), where the dotted lines correspond to the energy of the direct and indirect states. The dipole moment ed of the exciton in its indirect state results in a linear Stark shift of the emission energy.
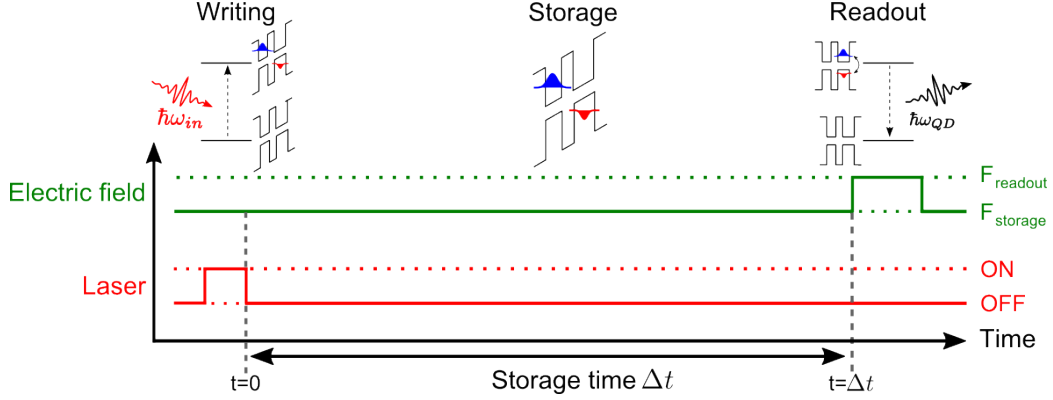
Figure 6.2: Operating principle behind photon and exciton-spin storage.

Photon and exciton-spin storage exploits the long exciton lifetime in the indirect state, originating from the spatial separation of the electron and the hole. A schematic of the memory operation is shown in Fig. 6.2(c). At t=0, a laser pulse creates an electron-hole pair which relaxes into the QDM. The electric field is such that the exciton is in an indirect state characterised by a long lifetime. This long lifetime will prevent recombination of the electron and the hole during a storage time Δt. At $t = \Delta t$, a sub-nanosecond modulation of the electric field is applied to bring the exciton from the indirect to the direct state so that readout of the emission occurs naturally through recombination.

6.4 Photon storage

6.4.1 Electric-field dependent photoluminescence spectroscopy

PL emission from the symmetric exciton state of the QDM used for photon storage is shown in Fig. 6.3(a) as a function of electric field. Fitting using Eq. (6.1) gives values of d=8.2±0.05nm (nominal design value is 8.5nm) and t=7.9±0.05meV (Fig. 6.3(b)). The high-energy antisymmetric states of the QDMs that we studied were either not visible (as in Fig. 2(a)) or of weak intensity and therefore not suitable for storage experiments. We attribute
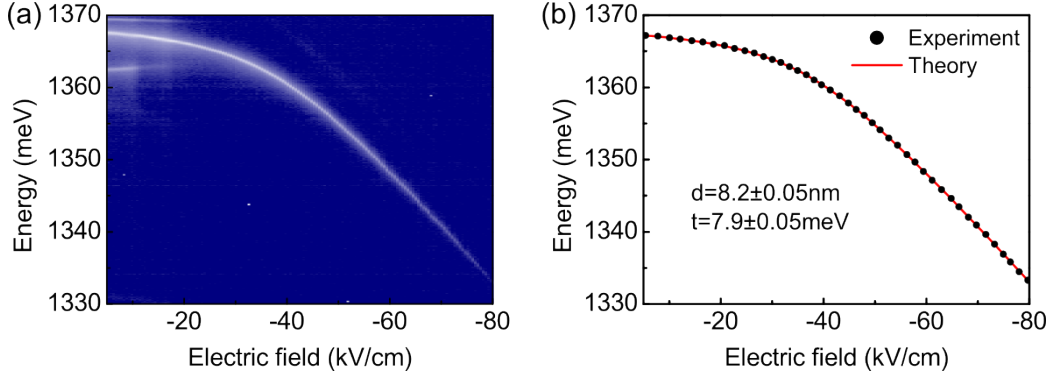
Figure 6.3: (a) Electric-field dependence of the PL emission from the symmetric exciton state used for photon storage. (b) Fitting of the energy using Eq. (6.1), where the black experimental points were extracted from (a).

this to effective thermalization of the exciton to the low-energy symmetric state. Missing spectral lines from QDMs due to thermalization effects have also been reported in other studies [111].

6.4.2 Exciton lifetime

The exciton lifetime in the QDM was measured as a function of electric field using standard time-resolved spectroscopy. Results are shown in Fig. 6.4(a) and (b). A rapid increase in lifetime is observed as the electron wavefunction progressively polarises from the top to the bottom QD.

This increase is mostly attributed to a reduction in the electron-hole wavefunction overlap. Indeed, according to Fermi's golden rule, the lifetime τ of a neutral exciton state $|\Psi_X\rangle$ that decays through radiative recombination to the ground state $|\Psi_0\rangle$ is such that

$$\tau^{-1} \propto |\langle\Psi_X| H' |\Psi_0\rangle|^2 \delta\left(E_X - E_0 - \hbar\omega\right), \tag{6.2}$$

where H' is the Hamiltonian of the electromagnetic interaction, E_X (E_0) is the exciton (ground) state energy and $\hbar\omega$ is the energy of the photon emitted after recombination. A recombination therefore occurs when the exciton and ground states are in resonance with the oscillating electromagnetic field. Using the envelope-function approximation $|\Psi_j\rangle = u_j(r)\phi_j(r)$, where u_j is
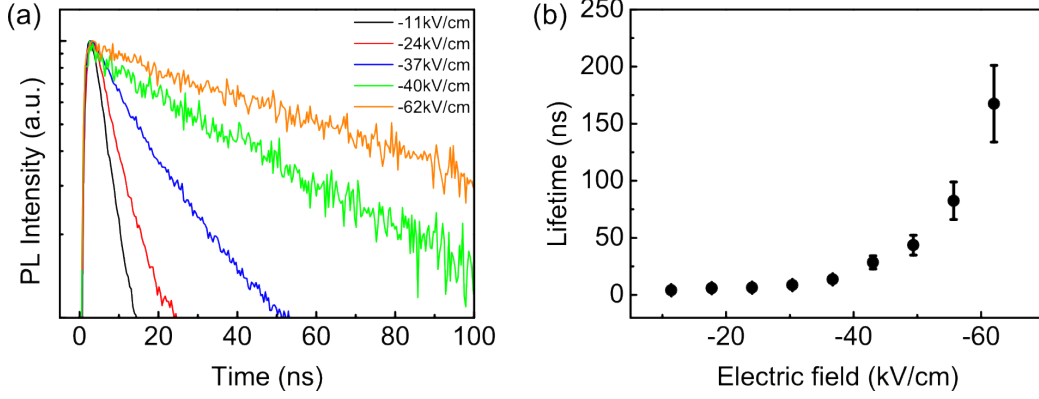
Figure 6.4: (a) Standard time-resolved measurements of the exciton emission at different electric fields. (b) Exciton lifetime as a function of electric field extracted from (a).

the atomic Bloch function of state j and ϕ_j is the envelope function, and considering only interband transitions, we find

$$\langle \Psi_X | \, H' \, | \Psi_0 \rangle \propto \langle u_X | \, \vec{\epsilon}.\vec{p}e^{i\vec{k}.\vec{r}} \, | u_0 \rangle \int \phi_X^*(\vec{r})\phi_0(\vec{r})d^3\vec{r}, \qquad (6.3)$$

where $\vec{\epsilon}$ and $\vec{k}$ represents respectively the polarisation and the wave vector of the emitted photon, and $\vec{p}$ is the dipole moment of the exciton. The atomic matrix element leads to the selection rules and depends on the coupling of the exciton dipole with the electromagnetic field. The envelope matrix element accounts for the spatial overlap of the electron and hole wavefunctions, which mostly accounts for the increase in lifetime with electric field as the electron and the hole are progressively localised in different QDs.

6.4.3   Storage operation

Using the method described in Fig. 6.2, we successfully stored the exciton for storage times up to $1\mu s$, corresponding to more than 1000 times the usual lifetime of an exciton in a single QD. The results are shown in Fig. 6.5, for storage times of respectively 0.2, 0.4, 0.6, 0.8, and $1\mu s$ and for a storage electric field of -77kV/cm, where the exciton lifetime is expected to be >250ns considering Fig. 6.4(b).
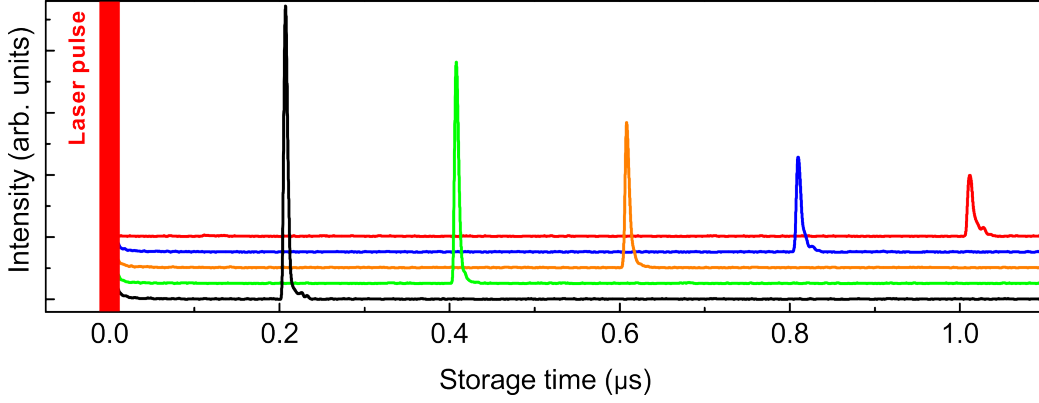
Figure 6.5: Successful storage of an exciton and readout signal after storage in an indirect state, at an electric field of -77kV/cm, for storage times up to 1μs.

A clear decay of the readout emission is observed in Fig. 6.5 caused by recombination of the indirect state, which has a finite lifetime. Considering a storage state with a lifetime τ_s, the decay in intensity with storage time Δt is given by

$$I(\Delta t) = I_0 e^{-\frac{\Delta t}{\tau_s}}, \qquad (6.4)$$

where I_0 is the intensity measured at t=0. Using Eq. (6.4), the lifetime τ_s of a specific storage state is measured indirectly by fitting the decay of the stored emission to an exponential (see Fig. 6.6(a) and 6.6(b)).

This was done for different storage states (i.e. different storage electric fields) and the corresponding measurements ("indirect measurement") are shown in Fig. 6.7 and compared to the measurements obtained by standard time-resolved spectroscopy ("direct measurement"). Agreement between both methods confirms the storage of the exciton in its indirect state. The lifetime at -77kV/cm was estimated at 677±91ns by fitting the decay in Fig. 6.5 but could not be measured directly and therefore does not appear in Fig. 6.7.

The maximum storage time achieved was limited only by the pulse pattern generator used to trigger the laser pulse, which had a maximum operating period of 1.1μs. Storage times of several seconds are expected using our
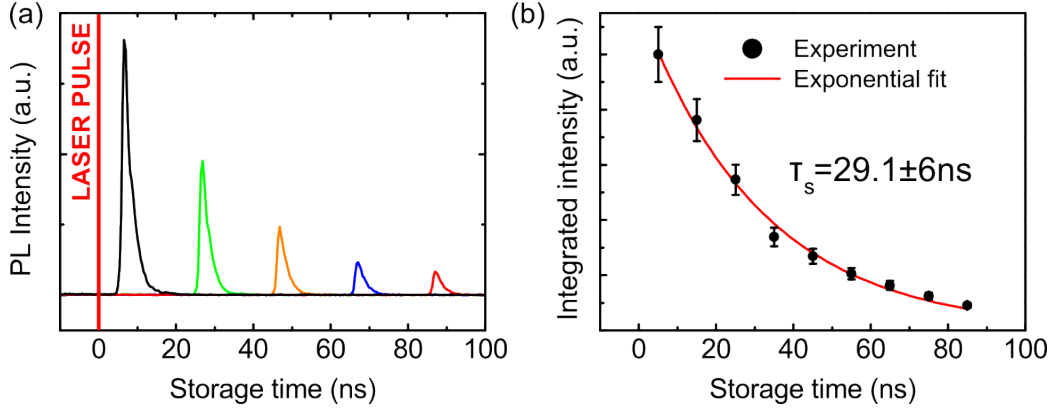
Figure 6.6: (a) Decay of the readout signal after storage in an indirect state at an electric field of -43.5kV/cm. (b) Exponential decay of the integrated intensity of the stored emission extracted from (a). The exponential fit provides an indirect measurement of the lifetime τ_s of the storage state.
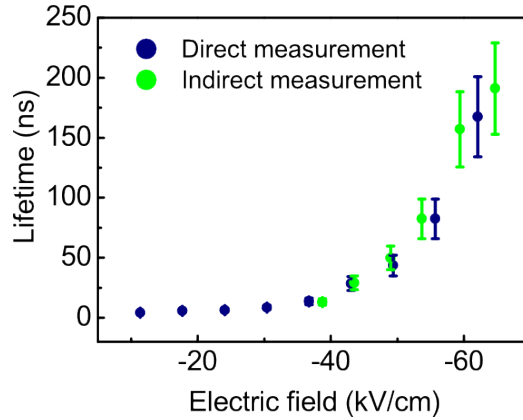
Figure 6.7: Exciton lifetime as a function of electric field measured directly using standard time-resolved measurements and indirectly by fitting an exponential decay to the decrease in intensity of the stored emission. Agreement between both methods confirms storage of an exciton into a single QDM.

scheme and engineering QDMs so that longer lifetimes can be achieved [122].

6.5 Exciton-spin memory

To store exciton-spins in a single QDM using the previously described operating scheme, both resonant optical excitation and a vertical magnetic field
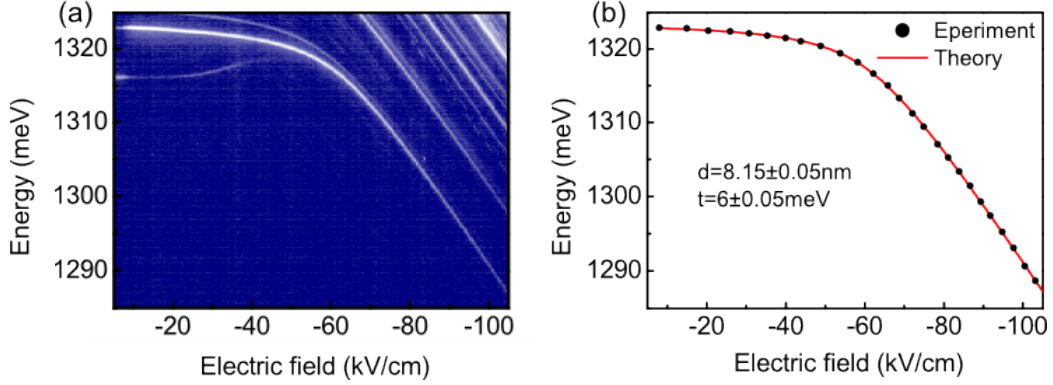
Figure 6.8: (a) Electric-field dependence of the PL emission from the symmetric exciton state used for exciton-spin storage. (b) Fitting of the energy using Eq. (6.1), where the black experimental points were extracted from (a).

are required. Resonant excitation will allow for high-fidelity transfer of the polarisation of a photon into the exciton spin state [115] while a vertical magnetic field will lift the degeneracy of the exciton spin states and define two Zeeman eigenstates with circular polarisations and long spin lifetimes [119, 120].

6.5.1 Exciton properties

In Fig. 6.8(a), PL emission from the QDM used for exciton-spin storage is shown as a function of electric field. Fittings using Eq. (6.1) provides values of d=8.15±0.05nm (nominal design value is 8.5nm) and t=6±0.5meV (Fig. 6.8(b)).

The lifetime as a function of electric field was measured using standard time-resolved spectroscopy and results are shown in Fig. 6.9. The lifetime appears to level out around 1μs for this particular QDM, which is thought to be related to the minimum overlap of the electron-hole wavefunctions reached in the indirect state (see Eq. (6.3)).
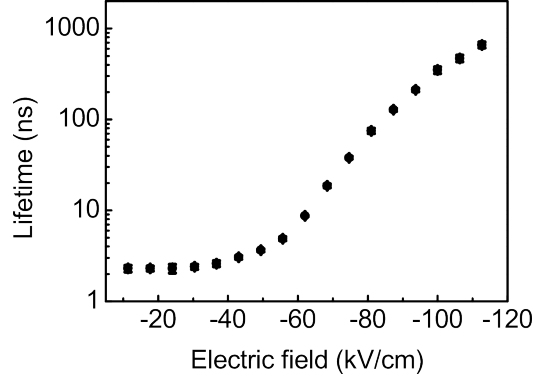
Figure 6.9: Exciton lifetime as a function of electric field. The lifetime is found to saturate around 1μs in the indirect state for this particular QDM.
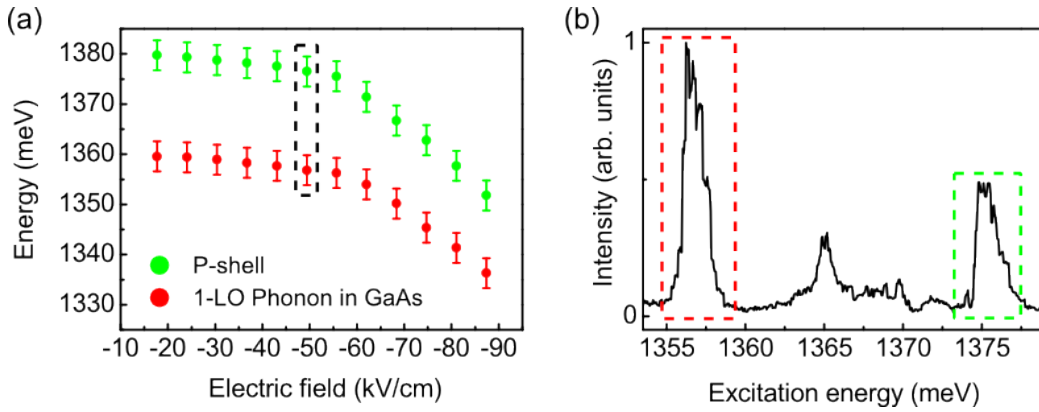
Figure 6.10: (a) Energies of the QDM resonances observed as a function of electric field. (b) Typical PLE spectrum measured at -50kV/cm from which the points in the dotted black box in (a) were extracted.

6.5.2 Resonant excitation

We performed PL excitation spectroscopy at various electric fields and two clear resonances were found. Their energies are plotted as a function of electric field in Fig. 6.10(a). A typical PLE spectrum measured at -50kV/cm is plotted in Fig. 6.10(b), where the resonance peaks of interest here are indicated by dotted boxes. The energies extracted from this particular spectrum correspond to the points in the dotted black box from Fig. 6.10(a).

The first resonance appears at 36.7±0.6meV from the exciton energy. A similar resonance at the same energy was found as well for other QDMs,

indicating resonant excitation through the creation of a 1-LO phonon in GaAs, the expected energy of which is $\approx$36.4meV [95]. The separation of the peak and the exciton emission remains constant as a function of electric field as expected for a phonon resonance. The second resonance appears at 55.2$\pm$2.1meV and is attributed to the *p*-shell of the exciton state. Consistent with this assignment, we found the position of this resonance varied from QDM to QDM. Moreover, electron tunneling appears to occur at a slightly different electric field for the *p*-shell and the *s*-hell, which we attribute to different separation between the energy levels for both QDs. Other weaker resonances can be observed in Fig. 6.10(b). No clear trends in the energy or intensity dependence with electric field were found for these resonances, which are therefore attributed either to other QDMs present on the same device or to some other excited state of the QDM under study.

6.5.3 Magneto-photoluminescence spectroscopy

The behaviour of our QDM under a vertical magnetic field was also studied. The energy of the exciton spin states as a function of magnetic field B is given by [129]

$$E(B) = E_0 + \gamma_1 B + \gamma_2 B^2 + \ldots, \tag{6.5}$$

where $|\gamma_1| = g\mu_B/2$ provides a direct measurement of the exciton g-factor g (μ_B is the Bohr magneton and the sign of γ_1 is given by the angular momentum ± 1 of the spin states), γ_2 is the diamagnetic coefficient, and where higher order terms can be neglected for the fields at which we are working ($B < 5T$).

The energy of the exciton states for our QDM as a function of magnetic field are shown in Fig. 6.11 along with a theoretical fit using Eq. (6.5). The small discrepancy observed at fields $B < 1.5T$ arises from the presence of the fine structure splitting s between the exciton linear eigenstates (s=76.5$\pm$0.1μeV for our QDM at zero electric and magnetic fields), which is not taken into account in Eq. (6.5) where the eigenstates are assumed to be circular. Indeed, exciton spin eigenstates become purely circular only for
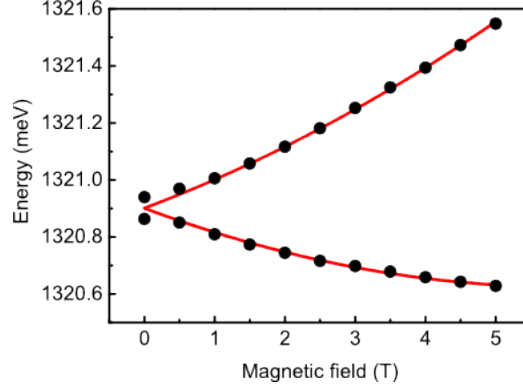
Figure 6.11: Magneto-PL of the exciton Zeeman states used for exciton-spin storage along with a theoretical fit using Eq. (6.5). The small discrepancy between theory and experiment at $B = 0T$ is due to the fine structure splitting between the exciton linear eigenstates.
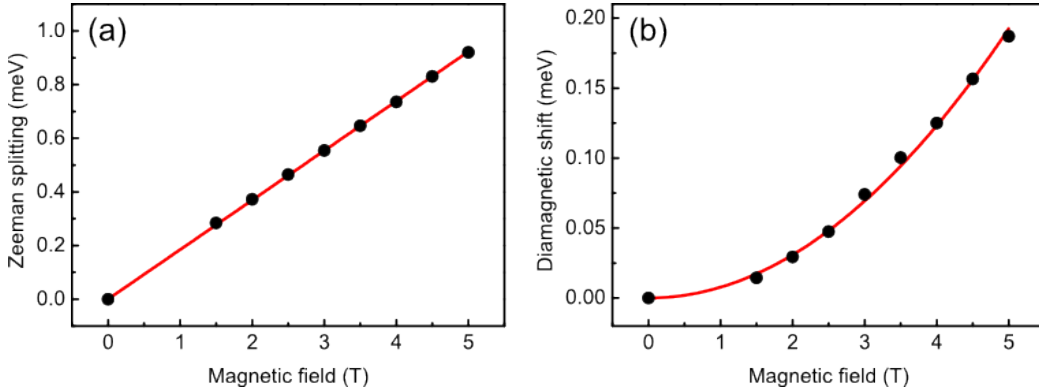
Figure 6.12: (a) Zeeman splitting and (b) diamagnetic shift of the exciton states as a function of magnetic field respectively with linear and quadratic fits. Results were obtained at an electric field of -17.7kV/cm.

vertical magnetic fields such that $g\mu_B B >> s$.

Measurements of the exciton Zeeman splitting and diamagnetic shift obtained at -17.7kV/cm are shown in Fig. 6.12(a) and 6.12(b) as a function of magnetic field. Points corresponding to $B < 1.5T$ were disregarded except for $B = 0T$ where the Zeeman splitting and the diamagnetic shift are expected to be 0. Linear and quadratic fits to the experimental points respectively provides a measurement of the g-factor and the diamagnetic coefficient.

The exciton g-factor and the diamagnetic coefficient γ_2 as a function of
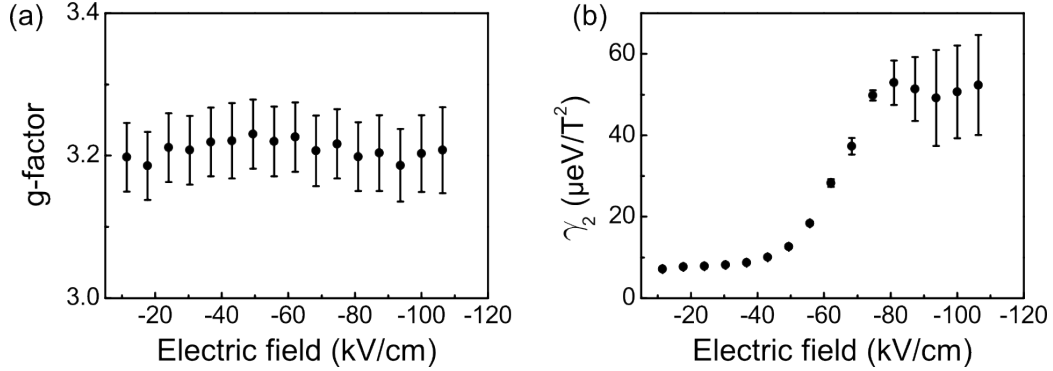
Figure 6.13: (a) g-factor and (b) diamagnetic shift a function of electric field. The g-factor is found to remain constant while the diamagnetic shift strongly depends on the electric field, providing a direct estimation of the lateral size of the exciton as the electron tunnels from one QD to another.

electric field are shown in Fig. 6.13(a) and 6.13(b). Each data point was obtained from measurements of the energy dependence of the Zeeman states with magnetic field as presented in Fig. 6.11 from which the linear and quadratic parts can be extracted as in Fig. 6.12. No electric field dependence of the g-factor is found for electron tunneling, as electron g-factors are similar in bulk GaAs (-0.44) and InAs QD (-0.6) [130]. However, a strong dependence of the diamagnetic coeffcient as a function of electric field is found. An order of magnitude difference is measured between the direct and indirect states. The diamagnetic shift is a measure of the in-plane electron-hole separation, which in turns depends on the lateral confinement and Coulomb interaction [129]. When the electron tunnels from the top to the bottom QD, the lateral confinement does not change significantly since both QDs have similar sizes. The increase in γ_2 in the indirect state therefore provides a measure of the reduced Coulomb interaction. γ_2 saturates at high electric field in the indirect state, where the electron-hole pair is fully spatially separated.

6.5.4 Exciton-spin storage

Exciting resonantly into the QDM while applying a vertical magnetic field allows for high-fidelity transfer of the photon circular polarisation into the exciton spin state. The fidelity of this transfer is usually defined [119, 120]

as the degree of circular polarisation of the exciton emission

$$P = \frac{I_{co} - I_{cross}}{I_{co} + I_{cross}},$$ (6.6)

where I_{co} (I_{cross}) is the intensity from the Zeeman exciton state co(cross)-polarised with the excitation circular polarisation. It is worth mentioning that the degree of polarisation usually used for a spin memory is a more severe figure of merit that the definition of the fidelity $f_{in} = |\langle\Psi_{out}|\Psi_{in}\rangle|^2$ (see Eq. 4.23) used in chapter 4. Indeed, it can be shown that

$$f_{in} = \frac{1 + P}{2}.$$ (6.7)

This should be kept in mind when comparing the results presented here with the results in Fig. 4.9. Fig. 6.14 illustrates the degree of polarisation of the stored emission obtained under phonon excitation after a storage time of 5ns and with a magnetic field of $B = 4T$. P is measured to be $80\% \pm 5\%$ (which corresponds to $f_{in} = 90\% \pm 2.5\%$). Comparable results were obtained when measuring the degree of polarisation of the "write" state (without storage operation). As a consequence, the storage operation is found to have no observable effect on the degree of polarisation and the limitation arises from the "write" operation, which may be improved by using wave plates calibrated at the QDM energy.

In Fig. 6.15, the degree of polarisation as a function of storage time is shown for both left- and right-hand circular pump polarisations and for three different excitation schemes: *p*-shell, phonon and *s*-shell. Discrimination between the laser signal and the exciton emission when exciting into the *s*-shell was achieved by taking advantage of the large Stark-shift between the energy of the indirect "write" state and the direct "read-out" state. The storage time was limited only by the 12.5ns period of the Ti:Sapphire laser used for the experiment. Moreover, ringing in the electrical signal prevented measurements at some storage times, as a change in electric field shifts the exciton energy out of the excitation or detection window through the Stark effect. This effect was particularly important in the case of *s*-shell excitation, where the resonance is the narrowest.
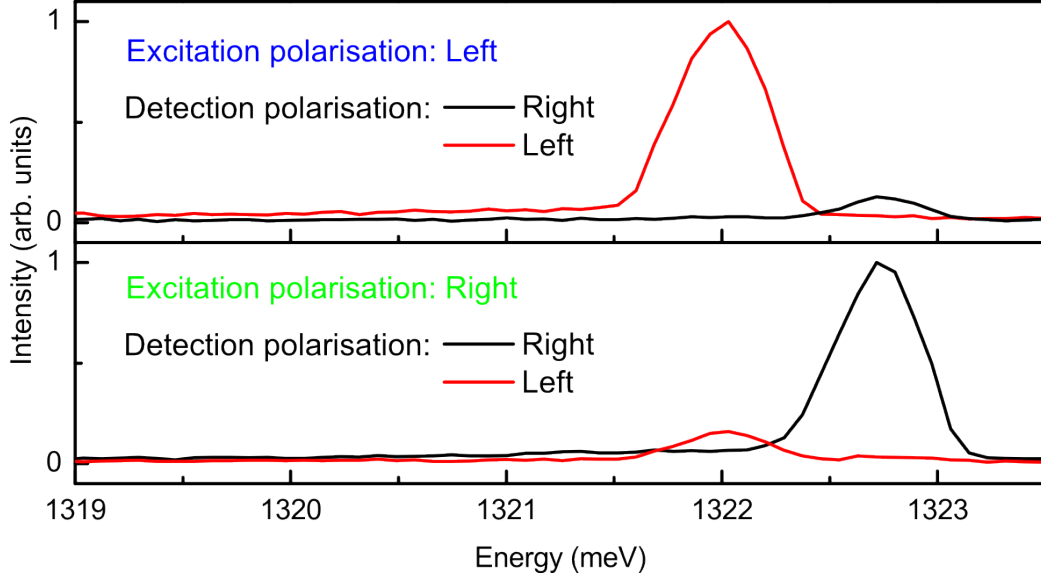
Figure 6.14: Typical spectra obtained after a storage time of 5ns when exciting in the phonon resonance and at a magnetic field $B = 4T$.
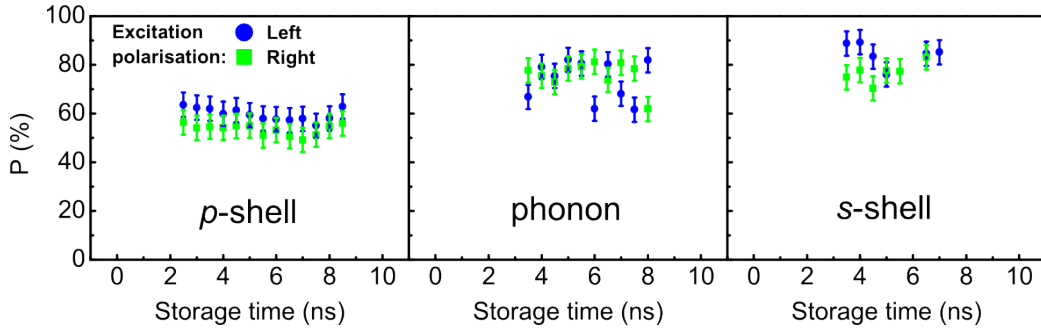
Figure 6.15: Degree of polarisation of the exciton-spin memory operation as a function of storage time when exciting in the p-shell, phonon, and s-shell resonances for both left- and righ-hand circularly polarised excitation. The data was taken at B=4T (similar results were obtained for $2T < B < 4T$.)

The degree of polarisation does not degrade over the 12.5ns repetition period of the experiment, suggesting that the spin relaxation time is substantially longer than the storage time. Average degrees of polarisation over time and over both pump polarisations are $57\pm5\%$ for p-shell excitation, $75\pm7\%$ for phonon excitation, and $81\pm6\%$ for s-shell excitation. No spin memory effect was observed when exciting in the continuum states, which

we attribute to spin relaxation as the charge carriers thermalize down to exciton ground state. The degree of polarisation is usually found to be slightly higher when exciting with left-hand circularly polarised light (particularly when using p-shell excitation), which is attributed to thermal relaxation from the right-polarised (high-energy, see Fig. 6.14) Zeeman eigenstate down to the left-polarised (low-energy) Zeeman eigenstate.

6.6 Towards an exciton quantum memory

It is possible to extend the presented exciton spin memory to an exciton quantum memory and store an arbitrary superposition of spin eigenstates if these can be made near degenerate. The energy separation of the eigenstates is ultimately limited by the exciton fine structure splitting and studies of single QDs have shown that it can be reduced to a level where the precession of a superposition state can be recorded with standard time-resolved spectroscopy [94, 97]. This would offer new possibilities to study and improve the coherence of an exciton spin state, which is expected to be limited by hyperfine interaction between the electron spin and the spins of the atomic nuclei [131].

The hyperfine interaction leads to an electron coherence time in the 10ns range for all III-V semiconductors as the naturally occurring isotopes of the constituent materials all have non-zero nuclear spin [132]. However, the nuclear field fluctuates on a much slower time scale, on the order of 100 μs. This means that a spin echo technique could be employed to extend the coherence time to this range [131]. Another alternative is to polarise the nuclear spins by optical pumping to keep the nuclear field fixed in time. Thereby any uncertainty in the phase evolution of the electron spin would be removed [133, 134]. It should also be mentioned that other material systems exist where most of the nuclei are zero spin isotopes. An example of such a material system is CdSe QDs embedded in ZnSe [135].

A further discussion on the properties of a solid-state quantum memory for polarised light based on quantum dot nanotechnology can found in [136], where the issues of efficiency, storage time, bandwidth, multiple-photon and

multiple-mode storage capacity, wavelength, and complexity are addressed.

6.7 Conclusion

In conclusion, we have successfully demonstrated photon storage in a single QDM up to 1μs. Moreover, exciton-spin storage has been demonstrated using resonant excitation and a vertical magnetic field with a fidelity above 90% (corresponding to a degree of polarisation above 80%). No decay in the fidelity was apparent within the period of the excitation laser of 12.5ns. Increasing the barrier thickness of the QDM, which would lead to longer lifetimes in the indirect state, and using a laser with a tunable period, we anticipate that spin storage in a single QDM is achievable for times in excess of 1ms [119, 122]. Moreover, a realistic extension of the presented exciton spin memory to a quantum memory was presented and should be achievable in the near future. Eventually, several QDM quantum memories could be combined on a single chip. Recent advances in the field of solid-state cavity quantum electrodynamics makes it likely that such a system would be scalable [137].

Chapter 7

Conclusion

This thesis described the work undertaken towards the development of semiconductor nanotechnologies for long-distance quantum communication. The three key requirements for long-distance quantum communication are light-matter interfaces, elementary quantum operations, and quantum memories. Electrical devices based on semiconductor quantum dots (QDs) have been shown to constitute a promising practical implementation potentially fulfilling all these requirements, as described in the summary of the main results below. This would therefore constitute another practical application for QDs in diode structures, which have been shown in the past to be fruitful resources for future quantum information technologies.

7.1 Summary of the main results

7.1.1 Single quantum dots

Single QDs were demonstrated to constitute high-fidelity interfaces between light and matter. Using quasi-resonant excitation where the laser energy is tuned about 36meV above the QD s-shell (corresponding to the energy of a 1-LO phonon in GaAs), we demonstrated transfer of the polarisation of single photons into the spin state of single electron-hole pairs in individual QDs. The fidelity was determined by measuring the square of the overlap between the excitation photon and the photon emitted by the electron-hole pair after

recombination. Photons with polarisations aligned with the natural linear polarisation of the QD eigenstates were transferred into, and restored from, the solid-state with fidelities above 95%. Diagonal and circular maximum superpositions of linear polarisations resulted in fidelities above 80%. The coherence of the exciton spin state time evolution was studied and spin-scattering times above 100ns were measured, while cross-dephasing appeared to occur on a timescale of ≈3ns.

Additionally, we used a recently discovered effect whereby the fine structure splitting between the exciton eigenstates as well as their orientation are tuned by applying a vertical electrical field. Subnanosecond modulation of the electric field were used to manipulate spins in the solid-state and elementary quantum operations were performed. Operating at electric fields such that only the splitting was modulated, phase-shift gates were successfully implemented and fidelities above 90% were measured. Combining modulation of both the splitting and the eigenstate orientation, arbitrary operations are expected to be possible and spin-flip gates were demonstrated with fidelities above 80%. The fidelities of the gate operations were limited by the finite response time of our electrical device, which could be reduced by orders of magnitude using state-of-the-art on-chip electronics.

Though promising results were obtained with single QDs as useful resources for long-distance quantum communication, the major limitation is their short radiative lifetime, which prevent their use as quantum memories. To overcome this problem, we studied quantum dot molecules (QDMs) in which electron-hole pairs could be spatially separated, suppressing their radiative recombination.

7.1.2 Quantum dot molecules

A comprehensive study of individual QDMs in diode structures was presented. Good control over the fabrication methods allowed for controlling the coupling energies of both electron and hole energy level resonances. Moreover, the doping profile of the diode structure was used to selectively control the tunneling carrier. Electric-field dependent optical spectroscopy of indi-

vidual QDMs was performed and revealed a rich line structure for the four main transitions. Theoretical models in great agreement with experimental observations were presented, providing a deeper understanding of the physics of QDMs. Finally, the fine structure of the exciton states in a QDM was studied and electrical tuning of the electron-hole exchange interaction was demonstrated. Moreover, a rotation of the eigenstates was observed, which could potentially lead to quantum operations on spins confined in QDMs.

Leaning upon the understanding that we acquired on QDMs, we stored photons up to 1μs in the solid-state, which was limited only by the pulse pattern generator used in our experiment. This storage was made possible through electrical control over the spatial separation between the electron and the hole in the QDM, leading to lifetimes measured up to 1000 times the radiative lifetime in single quantum dots. Using a vertical magnetic field to create pure spin eigenstates and resonant excitation, the circular polarisation of single photons was stored into the solid-state with fidelities above 90% (corresponding to a degree of polarisation above 80%), which did not appear to degrade for storage times up to the 12.5ns repetition period of the experiment.

7.2 Future work

Future work on single quantum dots consists in extending the schemes that we demonstrated to two-qubit quantum operations. This could be made possible by confining a second electron-hole pair in the quantum dot, forming therefore a neutral biexciton state. Quasi-resonant excitation of this second electron-hole pair would require a second laser synchronized with the first one and tuned to slightly different energy to account for the difference in Coulomb interaction due to the presence of the first electron-hole pair in the quantum dot. Electrical modulation of the splitting and orientation of the eigenstates could then be used to manipulate the spins of both electron-hole pairs.

Spin storage in QDMs up to the microsecond timescale could be achieved in the near future using an excitation laser of tunable period. The next

step would then consist in the storage of superpositions of spin states, which is possible if the spin states are made near degenerate. This requires their splitting to be reduced close to zero, which is feasible using the electric field dependence of the energy splitting between the spin states discussed in this thesis.

Eventually, combining storage of two electron-hole pairs in QDMs and quantum operations on spins using electric field subnanosecond modulation could lead to the development of controllable multi-qubit quantum memories for polarised light, a building block for future long-distance communication based on semiconductor nanotechnologies.

References

[1] C. Shannon. A mathematical theory of communications. *Bell system technical journal*, 27:239–423 and 623–656, 1948.

[2] R. Landauer. Information is physical. *Physics Today*, 44:23–29, 1991.

[3] R. Bouwmeester, A. Ekart, and A. Zeilinger. *The physics of quantum information*. Springer, 2000.

[4] M.A. Nielsen and I.L. Chang. *Quantum computation and quantum information*. Cambridge University Press, 2000.

[5] A. Peres. *Quantum theory: concepts and methods*. Kluwer, 1993.

[6] I.L. Chuang, N.A. Gershenfeld, and M. Kubinec. Experimental implementation of fast quantum searching. *Phys. Rev. Lett.*, 80:3408–3411, 1998.

[7] J.I. Cirac and P. Zoller. Quantum computations with cold trapped ions. *Phys. Rev. Lett.*, 74:4091–4094, 1995.

[8] D. Leibfried, R. Blatt, C. Monroe, and D. Wineland. Quantum dynamics of single trapped ions. *Rev. Mod. Phys.*, 75:281–324, 2003.

[9] T. Wilk, S.C. Webster, A. Kuhn, and G. Rempe. Single-atom single-photon quantum interface. *Science*, 317:488–490, 2007.

[10] C. Monroe. Quantum information processing with atoms and photons. *Nature*, 416:238–246, 2002.

[11] J.I. Cirac and P. Zoller. New frontiers in quantum information with atoms and ions. *Physics Today*, 57:38–44, 2004.

[12] F. Brennecke, T. Donner, S. Ritter, T. Bourdel, M. Köhl, and T. Esslinger. Cavity QED with a Bose–Einstein condensate. *Nature*, 40:268–271, 2007.

[13] A. Shnirman, G. Schön, and Z. Hermon. Quantum manipulations of small Josephson junctions. *Phys. Rev. Lett.*, 79:2371–2374, 1997.

[14] A. Wallraff, D.I. Schuster, A. Blais, L. Frunzio, R.-S. Huang, J. Majer, S. Kumar, S.M. Girvin, and R.J. Schoelkopfan. Strong coupling of a single photon to a superconducting qubit using circuit quantum electrodynamics. *Nature*, 431:162–167, 2004.

[15] R.M. Thompson, R.M. Stevenson, A.J. Shields, I. Farrer, C.J. Lobo, D.A. Ritchie, M.L. Leadbeater, and M. Pepper. Single-photon emission from exciton complexes in individual quantum dots. *Phys. Rev. B*, 64:201302, 2001.

[16] Z. Yuan, B.E. Kardynal, R.M. Stevenson, A.J. Shields, C.J. Lobo, K. Cooper, N.S. Beattie, D.A. Ritchie, and M. Pepper. Electrically driven single-photon source. *Science*, 295:102–105, 2002.

[17] P. Michler, A. Imamoglu, A. Kiraz, C. Becher, M.D. Mason, P.J. Carson, G.F. Strouse, S.K. Buratto, W.V. Schoenfeld, and P.M. Petroff. Nonclassical radiation from a single quantum dot. *Nature*, 406:968–970, 2000.

[18] C.H. Bennett and G. Brassard. Quantum cryptography: Public key distribution and coin tossing. In *Proceedings of the IEEE International Conference on Computers, Systems, and Signal Processing*, page 175, 1984.

[19] P. Kok, W.J. Munro, K. Nemoto, T.C. Ralph, and J.P. Dowling. Linear optical quantum computing with photonic qubits. *Rev. Mod. Phys.*, 79:135–174, 2007.

[20] E. Knill, R. Laflamme, and G. J. Milburn. A scheme for efficient quantum computation with linear optics. *Nature*, 409:46–52, 2001.

[21] R.M. Stevenson, R.J. Young, P. Atkinson, K. Cooper, D.A. Ritchie, and A.J. Shields. A semiconductor source of triggered entangled photon pairs. *Nature*, 439:179–182, 2006.

[22] L. He, M. Gong, C-F. Li, G-C. Guo, and A. Zunger. Highly reduced fine-structure splitting in InAs/InP quantum dots offering an efficient on-demand entangled 1.55-μ photon emitter. *Phys. Rev. Lett.*, 101:157405, 2008.

[23] A. Muller, W. Fang, J. Lawall, and G.S. Solomon. Creating polarization-entangled photon pairs from a semiconductor quantum dot using the optical stark effect. *Phys. Rev. Lett.*, 103:217402, 2009.

[24] C.H. Bennett, G. Brassard, C. Crépeau, R. Jozsa, A. Peres, and W.K. Wootters. Teleporting an unknown quantum state via dual classical and einstein-podolsky-rosen channels. *Phys. Rev. Lett.*, 70:1895–1899, 1993.

[25] P.M. Intallura, M.B. Ward, O.Z. Karimov, Z.L. Yuan, P. See, A.J. Shields, P. Atkinson, and D.A. Ritchie. Quantum key distribution using a triggered quantum dot source emitting near 1.3 μm. *Appl. Phys. Lett.*, 91:161103, 2007.

[26] C. Santori, D. Fattal, J. Vuckovic, G.S. Solomon, and Y. Yamamoto. Indistinguishable photons from a single-photon device. *Nature*, 419:594–597, 2002.

[27] A.J. Bennett, D. Unitt, A.J. Shields, P. Atkinson, and D.A. Ritchie. Influence of exciton dynamics on the interference of two photons from a microcavity single-photon source. *Opt. Express*, 13:7772–7778, 2005.

[28] S. Varoutsis, S. Laurent, P. Kramper, A. Lemaître, I. Sagnes, I. Robert-Philip, and I. Abram. Restoration of photon indistinguishability in the

emission of a semiconductor quantum dot. *Phys. Rev. B*, 72:041303, 2005.

[29] M. Atatüre, J. Dreiser, A. Badolato, A. Högele, K. Karrai, and A. Imamoglu. Quantum-dot spin-state preparation with near-unity fidelity. *Science*, 312:551–553, 2006.

[30] A. Greilich, S.E. Economou, S. Spatzek, D.R. Yakovlev, D. Reuter, A.D. Wieck, T.L. Reinecke, and M. Bayer. Ultrafast optical rotations of electron spins in quantum dots. *Nature Physics*, 5:262–266, 2009.

[31] A. Zrenner, E. Beham, S. Stufler, F. Findeis, M. Bichler, and G. Abstreiter. Coherent properties of a two-level system based on a quantum-dot photodiode. *Nature*, 418:612–614, 2002.

[32] S. Michaelis de Vasconcellos, S. Gordon, M. Bichler, T. Meier, and A. Zrenner. Coherent control of a single exciton qubit by optoelectronic manipulation. *Nature Photonics*, 4:545–548, 2010.

[33] N. Gisin, G. Ribordy, W. Tittel, and H. Zbinden. Quantum cryptography. *Rev. Mod. Phys.*, 74:145–195, 2002.

[34] R. Ursin, F. Tiefenbacher, T. Schmitt-Manderbach, H. Weier, T. Scheidl, M. Lindenthal, B. Blauensteiner, T. Jennewein, J. Perdigues, P. Trojek, B. Ömer, M. Fürst, M. Meyenburg, J.G. Rarity, Z. Sodnik, C. Barbieri, H. Weinfurter, and A. Zeilinger. Entanglement-based quantum communication over 144 km. *Nature Physics*, 3:481–486, 2007.

[35] T. Schmitt-Manderbach, H. Weier, M. Fürst, R. Ursin, F. Tiefenbacher, T. Scheidl, J. Perdigues, Z. Sodnik, C. Kurtsiefer, J.G. Rarity, A. Zeilinger, and H. Weinfurter. Experimental demonstration of free-space decoy-state quantum key distribution over 144 km. *Phys. Rev. Lett.*, 98:010504, 2007.

[36] T.D. Ladd, F. Jelezko, R. Laflamme, Y. Nakamura, C. Monroe, and J.L. OBrien. Quantum computers. *Nature*, 464:45–53, 2010.

[37] F.H.L. Koppens, C. Buizert, K.J. Tielrooij, I.T. Vink, K.C. Nowack, T. Meunier, L.P. Kouwenhoven, and L.M.K. Vandersypen. Driven coherent oscillations of a single electron spin in a quantum dot. *Nature*, 442:766–771, 2006.

[38] D. Press, T.D. Ladd, B. Zhang, and Y. Yamamoto. Complete quantum control of a single quantum dot spin using ultrafast optical pulses. *Nature*, 456:218–221, 2008.

[39] W.K. Wootters and W.H. Zurek. A single quantum cannot be cloned. *Nature*, 299:802–803, 1982.

[40] H.-J. Briegel, W. Dr, J.I. Cirac, and P. Zoller. Quantum repeaters: The role of imperfect local operations in quantum communication. *Phys. Rev. Lett.*, 81:5932–5935, 1998.

[41] M. Zukowski, A. Zeilinger, M.A. Horne, and A.K. Ekert. Event-ready-detectors bell experiment via entanglement swapping. *Phys. Rev. Lett.*, 71:4287–4290, 1993.

[42] N. Sangouard, C. Simon, H. de Riedmatten, and N. Gisin. Quantum repeaters based on atomic ensembles and linear optics. *Rev. Mod. Phys.*, 83:33–80, 2011.

[43] D.P. DiVincenzo. Two-bit gates are universal for quantum computation. *Phys. Rev. A*, 51:1015–1022, 1995.

[44] A. Barenco, D. Deutsch, A. Ekert, and R. Jozsa. Conditional quantum dynamics and logic gates. *Phys. Rev. Lett.*, 74:4083–4086, 1995.

[45] A. Barenco, C.H. Bennett, R. Cleve, D.P. DiVincenzo, N. Margolus, P. Shor, T. Sleator, J.A. Smolin, and H. Weinfurter. Elementary gates for quantum computation. *Phys. Rev. A*, 52:3457–3467, 1995.

[46] P. Michler, editor. *Single Semiconductor Quantum Dots*. Springer Berlin Heidelberg, 2009.

[47] D. Bimberg, M. Grundmann, and N.N. Ledentsov. *Quantum dot heterostructures.* John Wiley and Sons, 1999.

[48] M. Sugawara. *Self-assembled InGaAs/GaAs quantum dots*, volume 60 of *Semiconductors and Semimetals.* Academic Press, 1999.

[49] P. Yu and M. Cardona. *Fundamentals of Semiconductors: Physics and Materials Properties.* Springer, 2005.

[50] L. Jacak, P. Hawrylak, and A. Wójs. *Quantum Dots.* Springer-Verlag, 1998.

[51] J.R. Gell, M.B. Ward, R.J. Young, R.M. Stevenson, P. Atkinson, D. Anderson, G.A.C. Jones, D.A. Ritchie, and A.J. Shields. Modulation of single quantum dot energy levels by a surface-acoustic-wave. *Appl. Phys. Lett.*, 93:081115, 2008.

[52] R. Heitz, M. Grundmann, N.N. Ledentsov, L. Eckey, M. Veit, D. Bimberg, V.M. Ustinov, A.Yu. Egoro, A.E. Zhukov, P.S. Kop'ev, and Zh.I. Alferov. Multiphonon-relaxation processes in self-organized InAs/GaAs quantum dots. *Appl. Phys. Lett.*, 68:361–363, 1996.

[53] F. Adler, M. Geiger, A. Bauknecht, F. Scholz, H. Schweizer, M. H. Pilkuhn, B. Ohnesorge, and A. Forchel. Optical transitions and carrier relaxation in self-assembled InAs/GaAs quantum dots. *J. Appl. Phys.*, 80:4019–4026, 1996.

[54] A. Muller, E.B. Flagg, P. Bianucci, X.Y. Wang, D.G. Deppe, W. Ma, J. Zhang, G.J. Salamo, M. Xiao, and C.K. Shih. Resonance fluorescence from a coherently driven semiconductor quantum dot in a cavity. *Phys. Rev. Lett.*, 99:187402, 2007.

[55] H.W. van Kesteren, E.C. Cosman, W.A.J.A. van der Poel, and C.T. Foxon. Fine structure of excitons in type-II GaAs/AlAs quantum wells. *Phys. Rev. B*, 41:5283–5292, 1990.

[56] O. Stier, M. Grundmann, and D. Bimberg. Electronic and optical properties of strained quantum dots modeled by 8-band k.p theory. *Phys. Rev. B*, 59:5688–5701, 1999.

[57] R.J. Young. *Controlling the fine structure splitting in single InAs quantum dots.* PhD thesis, University of Cambridge, 2005.

[58] A.J. Bennett, M. Pooley, R.M. Stevenson, M.B. Ward, R.B. Patel, A. Boyer de la Giroday, N. Sköld, I. Farrer, C.A. Nicoll, D.A. Ritchie, and A.J. Shields. Electric field induced coherent coupling of the exciton states in a single quantum dot. *Nature Physics*, 6:947, 2010.

[59] G. Schedelbeck, W. Wegscheider, M. Bichler, and G. Abstreiter. Coupled quantum dots fabricated by cleaved edge overgrowth: From artificial atoms to molecules. *Science*, 278:1792–1795, 1997.

[60] T. Hatano, M. Stopa, and S. Tarucha. Single-electron delocalization in hybrid vertical-lateral double quantum dots. *Science*, 309:268–271, 2005.

[61] Q. Xie, A. Madhukar, P. Chen, N.P. Kobayashi, E. André, and O. Vatel. Vertically self-organized InAs quantum box islands on GaAs(100). *Phys. Rev. Lett.*, 75 (13):2542, 1995.

[62] H. Heidemeyer, U. Denker, C. Müller, and O.G. Schmidt. Morphology response to strain field interferences in stacks of highly ordered quantum dot arrays. *Phys. Rev. Lett.*, 91:196103, 2003.

[63] Z.R. Wasilewski, S. Fafard, and J.P. McCaffre. Size and shape engineering of vertically stacked self-assembled quantum dots. *J. Cryst. Growth*, 201:1131–1135, 1999.

[64] P. Howe, E.C. Le Ru, E. Clarke, B. Abbey, R. Murray, and T.S. Jones. Competition between strain-induced and temperature-controlled nucleation of InAs/GaAs quantum dots. *J. Appl. Phys.*, 95:2998, 2004.

[65] J. Stangl, V. Holý, and G. Bauer. Structural properties of self-organized semiconductor nanostructures. *Rev. Mod. Phys.*, 76:725–783, 2004.

[66] M.A. Herman and H. Sitter. *Molecular Beam Epitaxy: Fundamentals and Current Status.* Springer, 1989.

[67] D. Leonard, M. Krishnamurthy, C.M. Reaves, S.P. Denbaars, and P.M. Petroff. Direct formation of quantum-sized dots from uniform coherent islands of InGaAs surfaces. *Appl. Phys. Lett.*, 63 (23):3203, 1993.

[68] J.M. Moison, F. Houzay, F. Barthe, and L. Leprince. Self-organized growth of regular nanometer-scale InAs dot on GaAs. *Appl. Phys. Lett.*, 64 (2):196, 1994.

[69] P. Borri, W. Langbein, S. Schneider, U. Woggon, R.L. Sellin, D. Ouyang, and D. Bimberg. Ultralong dephasing time in InGaAs quantum dots. *Phys. Rev Lett.*, 87:157401, 2001.

[70] V. Zwiller, T. Aichele, and O. Benson. Quantum optics with single quantum dot devices. *New Journal of Physics*, 6:96, 2004.

[71] K.J. Vahala. Optical microcavities. *Nature*, 424:839–846, 2003.

[72] H. Benisty, H. De Neve, and C. Weisbuch. Impact of planar microcavity effects on light extraction - Part I: Basic concepts and analytical trends. *IEEE Journal of Quantum Electronics*, 34:1612–1631, 1998.

[73] A.J. Bennett, P. Atkinson, P. See, M.B. Ward, R.M. Stevenson, Z.L. Yuan, D.C. Unitt, D.J.P. Ellis, K. Cooper, D.A. Ritchie, and A.J. Shields. Single-photon-emitting diodes: a review. *Phys. Stat. Solidi B*, 243:3730–3740, 2006.

[74] R.B. Patel. *Indistinguishability of single photons from electrically controlled quantum dots.* PhD thesis, University of Cambridge, 2010.

[75] S. Adachi. GaAs, AlAs, and $Al_xGa_{1-x}As$: Material parameters for use in research and device applications. *J. Appl. Phys.*, 58:R1–R29, 1985.

[76] M. Bayer, G. Ortner, O. Stern, A. Kuther, A.A. Gorbunov, A. Forchel, P. Hawrylak, S. Fafard, K. Hinzer, T.L. Reinecke, S.N. Walck, J.P.

Reithmaier, F. Klopf, and F. Schäfer. Fine structure of neutral and charged excitons in self-assembled In(Ga)As/(Al)GaAs quantum dots. *Phys. Rev. B*, 65:195315, 2002.

[77] R.M. Stevenson, R.J. Young, P. See, D.G. Gevaux, K. Cooper, P. Atkinson, I. Farrer, D.A. Ritchie, and A.J. Shields. Magnetic-field-induced reduction of the exciton polarization splitting in InAs quantum dots. *Phys. Rev. B*, 73:033306, 2006.

[78] H. Kosaka, H. Shigyou, Y. Mitsumori, Y. Rikitake, H. Imamura, T. Kutsuwa, K. Arai, and K. Edamatsu. Coherent transfer of light polarization to electron spins in a semiconductor. *Phys. Rev. Lett.*, 100:096602, 2008.

[79] A. Imamoglu, D.D. Awschalom, G. Burkard, D.P. DiVincenzo, D. Loss, M. Sherwin, and A. Small. Quantum information processing using quantum dot spins and cavity QED. *Phys. Rev. Lett.*, 83:4204–4207, 1999.

[80] M. Bayer, A. Kuther, A. Forchel, A. Gorbunov, V.B. Timofeev, F. Schäfer, J.P. Reithmaier, T.L. Reinecke, and S. N. Walck. Electron and hole g factors and exchange interaction from studies of the exciton fine structure in $In_{0.60}Ga_{0.40}As$ quantum dots. *Phys. Rev. Lett.*, 82:1748–1751, 1999.

[81] D. Gammon, E.S. Snow, B.V. Shanabrook, D.S. Katzer, and D. Park. Homogeneous linewidths in the optical spectrum of a single gallium arsenide quantum dot. *Science*, 273:87–90, 1996.

[82] R. Hafenbrak, S.M. Ulrich, P. Michler, L. Wang, A. Rastelli, and O.G. Schmidt. Triggered polarization-entangled photon pairs from a single quantum dot up to 30 K. *New J. Phys.*, 9:315, 2007.

[83] S. Seidl, M. Kroner, A. Högele, K. Karrai, R.J. Warburton, A. Badolato, and P.M. Petroff. Effect of uniaxial stress on excitons in a self-assembled quantum dot. *Appl. Phys. Lett.*, 88:203113, 2006.

[84] G. Jundt, L. Robledo, A. Högele, S. Fält, and A. Imamoglu. Observation of dressed excitonic states in a single quantum dot. *Phys. Rev. Lett.*, 100:177401, 2008.

[85] K. Kowalik, O. Krebs, A. Lemaître, B. Eble, A. Kudelski, P. Voisin, S. Seidl, and J.A. Gaj. Monitoring electrically driven cancellation of exciton fine structure in a semiconductor quantum dot by optical orientation. *Appl. Phys. Lett.*, 91:183104, 2007.

[86] K. Kowalik, O. Krebs, P. Senellart, A. Lemaître, B. Eble, A. Kudelski, J. Gaj, and P. Voisin. Stark spectroscopy of coulomb interactions in individual InAs/GaAs self-assembled quantum dots. *Phys. Status Solidi (c)*, 3:3890–3894, 2006.

[87] J.D. Plumhof, V. Krápek, F. Ding, K.D. Jöns, R. Hafenbrak, P. Klenovský, A. Herklotz, K. Dörr, P. Michler, A. Rastelli, and O.G. Schmidt. Strain-induced anticrossing of bright exciton levels in single self-assembled GaAs/Al$_x$Ga$_{1-x}$As and In$_x$Ga$_{1-x}$As/GaAs quantum dots. *Phys. Rev. B*, 83:121302, 2011.

[88] M. Gong, W. Zhang, G.-C. Guo, and L. He. Exciton polarization, fine-structure splitting, and the asymmetry of quantum dots under uniaxial stress. *Phys. Rev. Lett.*, 106:227401, 2011.

[89] R. Singh and G. Bester. Lower bound for the excitonic fine structure splitting in self-assembled quantum dots. *Phys. Rev. Lett.*, 104:196803, 2010.

[90] M.M. Vogel, S.M. Ulrich, R. Hafenbrak, P. Michler, L. Wang, A. Rastelli, and O.G. Schmidt. Influence of lateral electric fields on multiexcitonic transitions and fine structure of single quantum dots. *Appl. Phys. Lett.*, 91:051904, 2007.

[91] J.A. Barker and E.P. OReilly. Theoretical analysis of electron-hole alignment in InAs-GaAs quantum dots. *Phys. Rev. B*, 61:1384013851, 2000.

[92] J.J. Finley, M. Sabathil, P. Vogl, G. Abstreiter, R. Oulton, A.I. Tartakovskii, D.J. Mowbray, M. S. Skolnick, S.L. Liew A.G. Cullis, and M. Hopkinson. Quantum-confined Stark shifts of charged exciton complexes in quantum dots. *Phys. Rev. B*, 70:201308, 2004.

[93] A.J. Bennett, R.B. Patel, J. Skiba-Szymanska, C.A. Nicoll, I. Farrer, D.A. Ritchie, and A.J. Shields. Giant stark effect in the emission of single semiconductor quantum dots. *Appl. Phys. Lett.*, 97:031104, 2010.

[94] T. Flissikowski, A. Hundt, M. Lowisch, M. Rabe, and F. Henneberger. Photon beats from a single semiconductor quantum dot. *Phys. Rev. Lett.*, 86:3172–3175, 2001.

[95] D. Strauch and B. Dorner. Phonon dispersion in GaAs. *J. Phys.: Condens. Matter*, 2:1457, 1990.

[96] A.J. Hudson, R.M. Stevenson, A.J. Bennett, R.J. Young, C.A. Nicoll, P. Atkinson, K. Cooper, D.A. Ritchie, and A. J. Shields. Coherence of an entangled exciton-photon state. *Phys. Rev. Lett.*, 99:266802, 2007.

[97] R.M. Stevenson, A.J. Hudson, A.J. Bennett, R.J. Young, C.A. Nicoll, D.A. Ritchie, and A.J. Shields. Evolution of entanglement between distinguishable light states. *Phys. Rev. Lett.*, 101:170501, 2008.

[98] J.F. Poyatos, J.I. Cirac, and P. Zoller. Complete characterization of a quantum process: the two-bit quantum gate. *Phys. Rev. Lett*, 78:390–393, 1997.

[99] X. Li, Y. Wu, D. Steel, D. Gammon, T.H. Stievater, D.S. Katzer, D. Park, C. Piermarocchi, and L.J. Sham. An all-optical quantum gate in a semiconductor quantum dot. *Science*, 301:809–811, 2003.

[100] R. Chau, B. Doyle, S. Datta, J. Kavalieros, and K. Zhang. Integrated nanoelectronics for the future. *Nature Materials*, 6:810–812, 2007.

[101] A. Mohan, M. Felici, P. Gallo, B. Dwir, A. Rudra, J. Faist, and E. Kapon. Polarization-entangled photons produced with high-

symmetry site-controlled quantum dots. *Nature Photonics*, 4:302–306, 2010.

[102] A. Boyer de la Giroday, N. Sköld, R.M. Stevenson, I. Farrer, D.A. Ritchie, and A.J. Shields. Exciton-spin memory with a semiconductor quantum dot molecule. *Phys. Rev. Lett.*, 106:216802, 2011.

[103] M. Bayer, P. Hawrylak, K. Hinzer, S. Fafard, M. Korkusinski, Z.R. Wasilewski, O. Stern, and A. Forchel. Coupling and entangling of quantum states in quantum dot molecules. *Science*, 291:451–453, 2001.

[104] H.J. Krenner, M. Sabathil, E.C. Clark, A. Kress, D. Schuh, M. Bichler, G. Abstreiter, and J.J. Finley. Direct observation of controlled coupling in an individual quantum dot molecule. *Phys. Rev. Lett.*, 94:057402, 2005.

[105] E.A. Stinaff, M. Scheibner, A.S. Bracker, I.V. Ponomarev, V.L. Korenev, M.E. Ware, M.F. Doty, T.L. Reinecke, and D. Gammon. Optical signatures of coupled quantum dots. *Science*, 311:636–639, 2006.

[106] M. Scheibner, M.F. Doty, I.V. Ponomarev, A.S. Bracker, E.A. Stinaff, V.L. Korenev, T.L. Reinecke, and D. Gammon. Spin fine structure of optically excited quantum dot molecules. *Phys. Rev. B*, 75:245318, 2007.

[107] J.R. Petta, A.C. Johnson, J.M. Taylor, E.A. Laird, A. Yacoby, M.D. Lukin, C.M. Marcus, M.P. Hanson, and A.C. Gossard. Coherent manipulation of coupled electron spins in semiconductor quantum dots. *Science*, 309:2180–2184, 2005.

[108] F.H.L. Koppens, J.A. Folk, J.M. Elzerman, R. Hanson, L.H. Willems van Beveren, I.T. Vink, H.P. Tranitz, W. Wegscheider, L.P. Kouwenhoven, and L.M.K. Vandersypen. Control and detection of singlet-triplet mixing in a random nuclear field. *Science*, 309:1346–1350, 2005.

[109] A.N. Vamivakas, C.-Y. Lu, C. Matthiesen, Y. Zhao, S. Fält, A. Badolato, and M. Atatüre. Observation of spin-dependent quantum

jumps via quantum dot resonance fluorescence. *Nature*, 467:297–300, 2010.

[110] D. Kim, S.G. Carter, A. Greilich, A.S. Bracker, and D. Gammon. Ultrafast optical control of entanglement between two quantum-dot spins. *Nature Physics*, 7:223–229, 2010.

[111] M. Scheibner, I.V. Ponomarev, E.A. Stinaff, M.F. Doty, A.S. Bracker, C.S. Hellberg, T.L. Reinecke, and D. Gammon. Photoluminescence spectroscopy of the molecular biexciton in vertically stacked InAs-GaAs quantum dot pairs. *Phys. Rev. Lett.*, 99:197402, 2007.

[112] A.S. Bracker, M. Scheibner, M.F. Doty, E.A. Stinaff, I.V. Ponomarev, J.C. Kim, L.J. Whitman, T.L. Reinecke, and D. Gammon. Engineering electron and hole tunneling with asymmetric InAs quantum dot molecules. *Appl. Phys. Lett.*, 89:233110, 2006.

[113] M.F. Doty, J.I. Climente, M. Korkusinski, M. Scheibner, A.S. Bracker, P. Hawrylak, and D. Gammon. Antibonding ground states in InAs quantum-dot molecules. *Phys. Rev. Lett.*, 102:047401, 2009.

[114] H.Y. Ramirez and S.J. Cheng. Tunneling effects on fine-structure splitting in quantum-dot molecules. *Phys. Rev. Lett.*, 104:206402, 2010.

[115] A. Boyer de la Giroday, A.J. Bennett, M.A. Pooley, R.M. Stevenson, N. Sköld, R.B. Patel, I. Farrer, D.A. Ritchie, and A.J. Shields. All-electrical coherent control of the exciton states in a single quantum dot. *Phys. Rev. B*, 82:241301, 2010.

[116] N. Sköld, A. Boyer de la Giroday, A.J. Bennett, I. Farrer, D.A. Ritchie, and A.J. Shields. Electrical control of the exciton fine structure of a quantum dot molecule. *In preparation.*

[117] S. Tanzilli, W. Tittel, M. Halder, O. Alibart, P. Baldi, N. Gisin, and H. Zbinden. A photonic quantum information interface. *Nature*, 437:116–120, 2005.

[118] A.J. Ramsay, S.J. Boyle, R.S. Kolodka, J.B.B. Oliveira, J. Skiba-Szymanska, H.Y. Liu, M. Hopkinson, A.M. Fox, and M.S. Skolnick. Fast optical preparation, control, and readout of a single quantum dot spin. *Phys. Rev. Lett.*, 100:197401, 2008.

[119] M. Kroutvar, Y. Ducommun, D. Heiss, M. Bichler, D. Schuh, G. Abstreiter, and J.J. Finley. Optically programmable electron spin memory using semiconductor quantum dots. *Nature*, 432:81–84, 2004.

[120] R.J. Young, S.J. Dewhurst, R.M. Stevenson, P. Atkinson, A.J. Bennett, M.B. Ward, K. Cooper, D.A. Ritchie, and A.J. Shields. Single electron-spin memory with a semiconductor quantum dot. *New Journal of Physics*, 9:365, 2007.

[121] D. Heiss, V. Jovanov, M. Bichler, G. Abstreiter, and J.J. Finley. Charge and spin readout scheme for single self-assembled quantum dots. *Phys. Rev. B*, 77:235442, 2008.

[122] T. Lundstrom, W. Schoenfeld, H. Lee, and P.M. Petroff. Exciton storage in semiconductor self-assembled quantum dots. *Science*, 286:2312–2314, 1999.

[123] H.J. Krenner, C.E. Pryor, J. He, and P.M. Petroff. A semiconductor exciton memory cell based on a single quantum nanostructure. *Nano Lett.*, 8:1750–1755, 2008.

[124] A.A. High, A.T. Hammack, L.V. Butov, L. Mouchliadis, A.L. Ivanov, M. Hanson, and A.C. Gossard. Indirect excitons in elevated traps. *Nano Lett.*, 9:2094–2098, 2009.

[125] R.M. Kraus, P.G. Lagoudakis, A.L. Rogach, D.V. Talapin, H. Weller, J.M. Lupton, and J. Feldmann. Room-temperature exciton storage in elongated semiconductor nanocrystals. *Phys. Rev. Lett.*, 98:017401, 2007.

[126] C. Rocke, S. Zimmermann, A. Wixforth, and J.P. Kotthaus. Acoustically driven storage of light in a quantum well. *Phys. Rev. Lett.*, 78:4099–4102, 1997.

[127] S. Zimmermann, A. Wixforth, J.P. Kotthaus, W. Wegscheider, and M. Bichler. A semiconductor-based photonic memory cell. *Science*, 283:1292–1295, 1999.

[128] A.G. Winbow, A.T. Hammack, and L.V. Butov. Photon storage with nanosecond switching in coupled quantum well nanostructures. *Nano Lett.*, 7:1349–1351, 2007.

[129] S.N. Walck and T.L. Reinecke. Exciton diamagnetic shift in semiconductor nanostructures. *Phys. Rev. B*, 57:9088–9096, 1998.

[130] M.F. Doty, M. Scheibner, I.V. Ponomarev, E.A. Stinaff, A.S. Bracker, V.L. Korenev, T.L. Reinecke, and D. Gammon. Electrically tunable *g* factors in quantum dot molecular spin states. *Phys. Rev. Lett.*, 97:197202, 2006.

[131] R. Hanson, L.P. Kouwenhoven, J.R. Petta, S. Tarucha, and L.M.K. Vandersypen. Spins in few-electron quantum dots. *Rev. Mod. Phys.*, 79:1217–1265, 2007.

[132] O. Krebs, B. Eble, A. Lemaître, P. Voisin, B. Urbaszek, T. Amand, and X. Marie. Hyperfine interaction in InAs/GaAs self-assembled quantum dots: dynamical nuclear polarization versus spin relaxation. *C.R. Phys.*, 9:874, 2008.

[133] A.V. Khaetskii, D. Loss, and L. Glazman. Electron spin decoherence in quantum dots due to interaction with nuclei. *Phys. Rev. Lett.*, 88:186802, 2002.

[134] W.A. Coish, V.N. Golovach, J.C. Egues, and D. Loss. Measurement, control, and decay of quantum-dot spins. *Phys. Stat. Sol. B*, 243:3658–3672, 2006.

[135] I.A. Akimov, D.H. Feng, and F. Henneberger. Electron spin dynamics in a self-assembled semiconductor quantum dot: The limit of low magnetic fields. *Phys. Rev. Lett.*, 97:056602, 2006.

[136] C. Simon, M. Afzelius, J. Appel, A. Boyer de la Giroday, S. J. Dewhurst, N. Gisin, C.Y. Hu, F. Jelezko, S. Kröll, J.H. Müller, J. Nunn, E.S. Polzik, J.G. Rarity, H. De Riedmatten, W. Rosenfeld, A.J. Shields, N. Sköld, R.M. Stevenson, R. Thew, I.A. Walmsley, M.C. Weber, H. Weinfurter, J. Wrachtrup, and R.J. Young. Quantum memories: A review based on the European integrated project Qubit Applications (QAP). *Eur. Phys. J. D*, 58:1–22, 2010.

[137] J.L. O'Brien, A. Furusawa, and J. Vuckovic. Photonic quantum technologies. *Nature Photonics*, 3:687–695, 2009.